RADIOMICS EVALUATION OF MULTIMODAL (X-RAY CT/SPECT/PET/MRI) IN VIVO IMAGING RESULTS IN ANIMAL MODELS

UNIVERSITY OF PÉCS

MEDICAL SCHOOL

DOCTORAL SCHOOL OF CLINICAL MEDICINE

The Leader of the Doctoral School: prof. Dr. KOVÁCS, L. Gábor

Program Leader: prof. Dr. KISS, István

Supervisor: Dr. GYÖNGYI, Zoltán

Doctoral Dissertation

Dr. BUDÁN, Ferenc Csaba
Pécs, 2019.

1. INTRODUCTION......5

1.1. In vivo imaging and nuclear medicine......6
1.1.1. X-ray computed tomography......7
1.1.2. Single Photon Emission Tomography......8
1.1.3. Positron Emission Tomography......8
1.1.3.1. Positron emission tomography with 18F- fluor-dezoxy-glucose tracer......9
1.1.4. Magnetic Resonance Imaging......9
1.1.5. Fusion imaging and radiomics evaluation......10

1.2. Radiomics improving data obtaining......13
1.2.1. Biological information in scope of radiomics study......13

1.3. Examined pathological conditions and environmental exposures......15
1.3.1. Bone diseases......16
1.3.1.1. Application of bone grafts......17
1.3.1.2 Rat tail model for monitoring bone healing......18
1.3.1.3 X-ray computed tomography and other methods for imaging bone diseases. 18
1.3.1.4. Single Photon Emission Tomography with ^{99m}Tc-Methyl diphosphonate tracer for bone scintigraphy......19
1.3.1.5. Bone formation imaging evaluated with radiomics approach......20
1.3.2. Environmental pollutions and public health......20
1.3.2.1. Air pollutants and lung diseases......21
1.3.2.1.1. X-ray computed tomography and other methods for imaging lung diseases 23
1.3.2.1.2. Hindrances and distorting factors of X-ray CT for imaging lung diseases 23
1.3.2.1.3. Radiomics evaluation of air pollution induced lung damage in mice model 24
1.3.2.2. Soil and water pollutants......25
1.3.2.2.1. Cadmium......26
1.3.2.2.2. Earthworm model for monitoring soil pollutants......30

2. OBJECTIVES......32

3. MATERIALS AND METHODS......33

3.1 Animal models......33
3.1.1. Rat model for bone grafts......33
3.1.1.1. Bone grafts......35
3.1.2 Mice lung model......35
3.1.3. Earthworm model......38
3.1.3.1. Pre-treatment of earthworms......38
3.1.3.2. Immobilization of earthworms......39
3.1.3.3. Cadmium exposure of earthworms followed up with in vivo imaging......40

3.2. Multimodal in vivo imaging......41
3.2.1. X-ray CT......41
3.2.1.1. Imaging of caudal vertebrae......41
3.2.1.2. Imaging of the chest......42

3.2.2. SPECT with 99mTc-Methyl diphosphonate tracer..42
3.2.3. In vivo MRI of earthworms..44

3.2.4. In vivo PET with 18F- fluor-dezoxy-glucose tracer of earthworms................45

3.3. Data analysis and radiomics evaluation...45
3.3.1.Analysis of bone graft model...45
3.3.1.1. Data analysis of bone graft model...45
3.3.1.2. Radiomics-based evaluation of bone graft model.......................................46
3.3.2. Analysis of mice lung model...46
3.3.2.1. Data analysis of mice lung model...46
3.3.2.2. Radiomics-based evaluation of mice lung model..47
3.3.3.1. Data analysis of soil pollution model..50
3.3.4. Statistical analysis..51
3.3.4.1. Statistical analysis for in vivo imaging of bone formation model................51
3.3.4.2. Statistical analysis for in vivo imaging of air pollution model.....................51
3.3.4.3. Statistical analysis of earthworm model..51
3.3.4.3.1. Statistical analysis of pre-treatment for in vivo imaging of earthworm model..51
3.3.4.3.2. Statistical analysis of earthworm model using PET with 18F- fluor-dezoxy-glucose tracer...52

4. RESULTS..52

4.1. Examined descriptive parameters of bone grafts..52
4.1.1. Bone opacity imaged with X-ray CT..52
4.1.2. 99mTc-Methyl diphosphonate activity imaged with SPECT..........................52
4.1.3. Time related changes of parameters..53
4.1.4. Multimodal data analysis utilizing radiomics evaluation................................54

4.2. Observations and examined descriptive parameters of lungs............................55
4.2.1. Observations based upon the X-ray CT of chest..55
4.2.2. Examined descriptive parameters of lungs...56
4.2.2.1. Frequency distributions of attenuation data (height, width and position parameters of Gaussian curve)...56
4.2.2.2. Cut-off ranges (COR) of attenuation associated with calculated fractal dimension (FD)...56
4.2.2.3. FD – COR mathematical function's descriptor parameters analyzed...........57

4.3. Examined parameters of earthworms...58
4.3.1. Parameters of pre-treatment for optimal earthworm immobilization...............58
4.3.2. Application of alcohols for immobilization...59
4.3.3. MRI observations of immobilized earthworms...60
4.3.4. FDG uptake of earthworms...61

5. DISCUSSION..63

5.1. Imaging of bonegrafts enhanced bone healing..63
5.1.1. Inflammatory mechanisms affecting bonegrafts and bone formation..............64
5.1.2. Potential distorting factors of bone formation model's in vivo imaging..........65
5.1.3. Normalization and filtration in order to improve data evaluation...................65
5.1.4. Examined bone grafts effect on bone formation...66

5.2. Imaging of air pollution induced alterations of the lungs..................................68
5.2.1. Attenuation of lung tissues based upon simple X-ray CT scans......................68
5.2.3. Fractal dimension cut-off range mathematical function histogram-based parameters of lung tissues..69

5.3. Imaging of earthworms...73
5.3.1. Pre-treatment for optimal earthworm immobilization.....................................73
5.3.1.1. Immobilization of earthworms..74
5.3.2. Imaging of earthworms utilizing MRI...76
5.3.3. Imaging of earthworms utilizing FDG PET..77
5.3.4. Limitations of earthworm model..80

6. CONCLUSION...81

6.1. The opportunities based upon the newly developed animal models, with radiomics-based evaluation...82
6.1.1. Possible applications of the bone formation model...82
6.1.2. Possible applications of the radiomics-based evaluation of the respiratory organ...83
6.1.3. Opportunities based upon the earthworm model...84
6.1.3.1. Opportunities of earthworm's MRI...84
6.1.3.2. Opportunities of earthworm's PET imaging...84

6.2. Risk groups and interventions..86
6.2.1. Risk groups...86
6.2.1.1. Risk groups of bone diseases...86
6.2.1.2. Risk groups of lung diseases..87
6.2.1.3. Risk groups of cadmium poisoning...87
6.2.2. Preventions and interventions regard to the studied diseases and environmental pollution..88
6.2.2.1. Prevention or treatment of bone diseases..89
6.2.2.2. Strategies for ameliorating lung diseases symptoms and slow down progression..89
6.2.2.3. Interventions to mitigate the hazards of environmental cadmium pollution. 90

7. SUMMARY..91

8. ACKNOWLEDGEMENT...94

9. PUBLICATION LIST...95

9.1.Publications related to the present thesis...95

9.2. Presentations related to the present thesis...96

9.3 Other own publications, mentioned in the thesis...97

10. LIST OF ABBREVIATIONS..99

11. REFERENCES...102

12. APPENDIX..123

1. INTRODUCTION

X-ray computed tomography (CT), positron emission tomography (PET), single photon emission tomography (SPECT) and magnetic resonance imaging (MRI) are used to reveal important quantitative anatomical and functional information. Multimodal in vivo (X-ray CT/PET/SPECT/MRI) fusion hybrid imaging provides, comparable, sensitive, longitudinal and robust data, thereby increasing accuracy as well as precision (Környei, 1997; Budán, 2018a). Radiomics analysis approach is based on extraction of large amounts of advanced quantitative medical data obtained with CT, PET, SPECT and MRI, elucidating valuable diagnostic, prognostic or predictive information through computing meta-data (Gillies 2016; Kumar, 2012). Utilizing radiomics evaluation the mentioned parameters of the results of a fusion hybrid imaging can be advanced further, or enables decreasing sample number, respectively (Gillies, 2016; Kumar, 2012; Kolossváry, 2018). These data can be not only morphologic or results of biochemical reactions, but also time-related information about positions of moving organs.

In developed countries diseases of locomotor- and the respiratory- system, as well as (WHO, 2018). These diseases cause worldwide an immense loss of life-years, life-quality, as well as financial burden. Environmental pollution exacerbates the mentioned diseases, thereby increases their morbidity as well as mortality (Muralikrishna, 2017). Proper monitoring may detect populations with increased risk as well as it could enhance decisions about necessary interventions to treat environmental pollution issues.

In this dissertation we focus on recently developed radiomics-based evaluation techniques utilizing novel in vivo animal models (Budán, 2018a) of bone formation (Budán, 2018b; Budán, 2018c) and also animal models capable to detect air (Budán, 2014a; Máthé 2015, Szigeti, 2016) and soil pollutions (Budán 2013a; Budán 2013b; Budán, 2014b) early.

1.1. In vivo imaging and nuclear medicine

The discovery of radiography paved the way towards in vivo imaging. In vivo molecular imaging method X-ray CT, and MRI are used to detect or follow up anatomical attributions, while PET and SPECT provides functional information (Studwell, 2011). Region of interests (ROI) or voxels of interests (VOI) is selected from where the spatial quantitative signal values are collected. Specific signal ranges with or without filtering are reconstructed. Also the acquisition time and the examined voxel's size are cardinal parameters, influencing the signal-to-noise ratio greatly.

The application of contrast materials (CM) enhance the signal - and quality of imaging - of X-ray CT and MRI greatly, but they are mostly delivered via injection or infusion. Therefore they are invasive techniques. Further disadvantages of CM is that they may increase blood's viscosity (Blumgart, 1926.). An exception is the non-invasive per os barium-sulfate ($BaSO_4$) CM for the imaging of gastrointestinal tract (Diós, 2016; Diós, 2015).

Gating is among radiomics filtering approaches. It is utilized frequently in cardiac and pulmonary imaging, with the purpose to exclude motion artefacts, based on special imaging considering the ventilation or the perfusion (Maki, 1999). Motion artefacts can be caused by voluntary or involuntary motion of patient, but also by physiological function of some organs, for example the heart or the lungs. Indeed, gating is a cardinal factor influencing several parameters of in vivo imaging when moving body parts are targeted. For example, it can be technically problematic in clinical practice to perform gating in patients with decreased lung capacity due to COPD (Szigeti, 2016). Gating also increases the time of examination and consequently X-ray exposure of patients.

On the other hand, nuclear medicine is the utilization of radioactive isotopes always inside the body of the target organism with medical purpose, both for detection and curative therapy. SPECT and PET modality require radiotracer (Lawrence, 1947).

Nowadays, multimodal (X-ray CT/SPECT/PET/MRI) fusion hybrid imaging can be applied (Környei, 1997; Budán, 2018a) that can be advanced further utilizing the aforementioned radiomics data handling and evaluation (Budán, 2018a).

1.1.1. X-ray computed tomography

Between 1869 and 1875, William Crookes and Johann Hittorf developed the so called Crook's pipe - the first X-ray similar device - based upon strong vacuum (0.005-0.1 Pa) and electricity (5 kV and 100 kV voltage) (Crookes, 1902). In 1895, Wilhelm C. Röntgen added a metal target anode to the device and has presented at the Parisian Scientific Academy the first X-ray photo, with the purpose of medical use (Röntgen, 1895).

More photos (from different angles about the same object) with exactly defined spatial locations enabled to locate exact 3D anatomical regions. Established upon this principle, Johann Radon as early as in 1917 has developed the theoretical background of CT. But, only in 1971 has enabled the technical level of computers developing the first X-ray based CT by Sir Godfrey Hounsfield. The X-ray attenuation of a specific voxel, correlates to the cubic of effective atomic numbers of the components. These effective atomic numbers contribute to the attenuation according to their molar quantity (Coles, 1995). For the sake of completeness we need to mention, that the specific technical properties of utilized CT (detectors, beam-energy profiles, collimators and filters), as well as other factors (sample shape, temperature drift, contrast enhancement, beam hardening) can influence the measurements (Coles, 1995).

Hounsfield unit (HU) is a linear transformation of the original linear attenuation coefficient measurement into one in which the radiodensity of distilled water at standard pressure and temperature (STP) is defined as 0 HU and air -1,000. The HU scale applies to medical-grade CT scans but not to conebeam CT (CBCT) scans. Different substances and tissues have different radiodensities at standard pressure and temperature: fat is defined at standard pressure and temperature (STP) -100 to -50 HU, muscle +10 to +40 and bone from +700 for cancellous bone to +3,000 for cortical bone (Feeman, 2010b).

1.1.2. Single Photon Emission Tomography

Kuhl and Edwards, in 1963, have developed SPECT, which is based upon a gamma camera acquiring 2D projection images rotated around the patient while spatial data are computed utilizing a tomographic reconstruction algorithm (Hutton, 2014). Fan-beam and parallel collimators are applied in clinical imaging and pinhole or multiple pinhole collimators for small-animal imaging (Van Audenhaege, 2015). SPECT is a cost-effective method with the further advantage that multiple radionuclides, for example 99-technetium (^{99m}Tc), 123-iodine (^{123}I), 32-phosphorus (^{32}P), and 67-gallium (^{67}Ga), can be utilized simultaneously. Moreover, widebrenching precursors are presented to form a complex molecule with radioisotopes with the purpose to form suitable molecules for in vivo imaging. Thus diagnostic as well as therapeutic applications of many radiopharmaceuticals utilized in SPECT are known.

1.1.3. Positron Emission Tomography

Michael E. Phelps in 1974 created the first positron emission tomography (PET), inspired by the principle of CT. The modality is based upon detecting pairs of gamma-rays (approximately 511 keV) derived indirectly from electron-positron annihilation reaction. A coincident circuits (with usually 10 ns time-window) are utilized as detector.

Positron emission is produced by neutron-deficient radioisotopes, for example 11-carbon (^{11}C), 15-oxygen (^{15}O), 13-nitrogen (^{13}N), 18-fluor (^{18}F), and 68-gallium (^{68}Ga). These radioisotopes are produced by charged-particle bombardment (usually) with low-energy cyclotrons (Dewi, 1995). Neutron-deficient radioisotopes (tracers) are suitable for PET imaging and are mostly attached to bioactive molecules. This radiopharmaceutical compounds are applied as injections. They indicate specific biological functions, for example enzymatic reactions, etc. (Lauber, 2017).

Derived from its concept, the disadvantage of PET is its limited spatial resolution. In clinical devices, the current resolution does not surpass 4 mm of full width at half maximum of the modulation transfer function of the imaging system.

However, this value makes possible the detection of circa 1-2 mm diameter lesions in a low background radiotracer image. Quantification occurs for circa 1 cm diameter objects (Lauber, 2017).

For use in animal experiments, several dedicated “micro-PET” systems are applied that allow an advanced resolution, namely below 0.7 mm. In those systems detection of small lesions is possible at circa 0.5 mm diameter but a volume of interest`s quantified radioactive tracer concentration can only be reliably measured if they are circa 1.5 mm in diameter (Lauber, 2017).

1.1.3.1. Positron emission tomography with 18F- fluor-dezoxy-glucose tracer

FDG indicates hexokinase reaction, which is increased in tumor due to the typically enormously grown metabolic rate.

Clinical PET utilizing 18F- fluor-dezoxy-glucose (FDG) radiotracer is used most frequently for oncological imaging, to underpin tumor staging or carry out metastasis detection. Nevertheless, besides oncological application also cardiologic, neuro-psychiatric, or inflammatory clinical utilization of FDG is common (Legoza, 2010; Trón, 2002).

On the other hand, micro-PET is used mostly to perform preclinical imaging in oncological research (by tracking metabolism, gene expression, cell proliferation, angiogenesis, hypoxia or apoptosis), or in cardiology (to examine heart function and find cardiac infarction) (Lauber, 2017). It is also used in neurology (measuring cerebral metabolism and perfusion), as well as for drug development (Lauber, 2017).

Recently, even in a radiogenomic approach (see below) Yipp et al. utilizing FDG PET evaluated the reconstruction with a radiomics feature, namely normalized inverse difference moment (IDMN), elucidated the difference of epidermal growth factor receptor (EGFR) mutations positivity from EGFR negativity, and also EGFR positivity from Kirsten rat sarcoma viral (KRAS) positivity (Yip, 2016).

1.1.4. Magnetic Resonance Imaging

Magnetic resonance imaging (MRI) (earlier known as nuclear magnetic resonance

(NMR)) is based upon that in great static magnetic field (mostly 1.5 T) certain intense radiofrequency pulses generate a characteristic spin echo signals for a specific nuclei (Perrin, 2012). The main principle of MRI was discovered by E.L. Hahn in year 1950, that the amplitudes of spin echo signals can be determined and thereby relaxation time can be calculated, which is informative in regard to specific quantity of that nuclei (Hahn, 1950). Practically mostly protium (H) density pattern inside a VOI is examined and thereby indicating anatomical information.

A large amount of development leaded to the modern in vivo MRI technique that can produce robust, sensitive and longitudinal results using a small sample size owing to the fact that each animal acts as a control for itself over time (Lauber, 2017) These imaging studies are quick, high throughput (for example multiple animals can be imaged at once) and yield easily repeatable data. Thus, results of MRI ideally could detect early morphological changes.

Interestingly, MRI is capable to provide functional information too, with advanced imaging techniques, such as MRI microscopy, magnetic resonance spectroscopy, functional MRI, diffusion tensor imaging even support classical histochemistry (Busato, 2016). According to Al-Kadi et al., the same goal can be achieved in lung tumors, when CM is used in order to enhance signal, which may provide per se better signal noise ratio, but also in addition radiomics-based evaluation is carried out to possess further information, see below (Al-Kadi, 2008).

1.1.5. Fusion imaging and radiomics evaluation

Fusion imaging (or hybrid imaging) has an informatics background and combines modalities with each other. The purpose is, that the possessed biological information by PET or SPECT requires to be correspond to spatial data, gained by utilizing mostly CT or MRI. Mostly Wavelet transforms are utilized to carry out fusion imaging, see below (Kolossváry, 2018).

Computer-aided diagnosis and detection (CAD) systems are based upon some algorithm, which were developed by analyzing a large amount of medical data derived from imaging modules (CT, PET, SPECT and MRI). CADs are standalone systems in order to detect or diagnose diseases (mostly cancer). The purpose of CAD systems are to fasten and increase reliability of evaluation of reconstructions. However, they are suited only to improve single and simple decisions, for example to decide in a specific sample if lesion or cancer is presented (Gillies, 2016). Besides CAD there are other methods to highlight relevant information of reconstructions, for example the application of two different lookup tables (LUT) can be utilized to visualize voxels: one for the VOIs of the examined targets and another for VOIs of the background (Diós, 2015). Radiomics can be seen as a further development of CAD.

Most of the properties and the attributions as well as the purpose of radiomics analysis were mentioned earlier (Gillies 2016; Kumar, 2012). Additionally, detecting previously unknown biological relevance of one parameter or elucidate novel connection between firstly unexpected quantitative parameters can be a goal of radiomics too.

Based on quantifying spatial and textural properties of voxels the main methods of radiomics are grouped into 4 major categories: (1) intensity-based metrics, (2) texture-based analysis, (3) shape-based measures, and (4) transform-based metrics (Kolossváry, 2018).

The intensity-based metrics quantify the different aspects of the voxel's signal intensity abstracted on a histogram and evaluating its distribution with the following parameters: (1) average and variation, (2) shape, and (3) diversity (Kolossváry, 2018).

Shape diversity texture-based metrics fit functions to characterize the histograms and mean, standard deviation (SD) kurtosis and skewness are the mostly used descriptive parameters. Diversity (or dissimilarity) of values provide information about the heterogeneity of a sample. It can be calculated by the concept, that energy quantifies the overall magnitude of the intensities of voxels and it is calculated by squaring the values and then summing them. The entropy of a system is equal to the sum of these values multiplied by -1. Entropy quantifies uncertainty by weighing the information content of an event with its probability. Some entropy parameters are also representing well the malignant transformations of tissues (see below) (Kolossváry, 2018).

The texture-based metrics use patterns corresponding to the systematic, spatial repetition of some physical characteristics such as intensity, shape, or color and attempts to quantify them using mathematical formulas based on the spatial relationship of the voxels (Kolossváry, 2018). Haralick et al. used gray-tone spatial dependencies matrix, commonly known as gray level co-occurrence matrix (GLCM), for the texture analysis of 2D images in order to quantify how frequently similar value voxels are located next to each other within a given direction and distance (Haralick, 1973). More than 14 different statistics can be established upon this method (Kolossváry, 2018). Higher-order statistics, using gray-level run-length matrix (GLRLM) assesses how many voxels (more than 2 voxels) are next to each other with the same value (Galloway, 1975).

The shape-based metrics are suitable to characterize complex 3D structures. Minkowski functionals calculate different properties of geometrical objects, such as the Euler characteristic or genus, which is a parameter describing the connectivity of the data points, estimated by calculating the number of voxel groups with information minus the enclosed regions where there is no signal (Minkowski, 1903; Larkin, 2014). Also FD parameters are in this category, since fractal geometry quantifies self-symmetry by examining repeating patterns at different scales. With the scale of statistically self-similar and non-overlapping subsets with respect to a scaling factor can FD be computed (Mandelbrot, 1989) providing information about a structure's complexity and homogeneity (Smith, 1996). Also lacunarity the inhomogeneity of the examined fractal area is needed to be mentioned to describe non-Euclidean structures (Al-Kadi, 2008). The lacunarity is defined as the ratio of the variance over the mean value of the function (Petrou, 2006). For example, objects with no fractal (thereby also without lacunarity) properties scale their characteristics exponentially depending on the dimension, while more branching objects have an increased value, for example the length of a coastline of a river increases if we magnify the details of pattern (Mandelbrot, 1967).

Also transform-based metrics are needed to be mentioned. The concept of Fourier transformation (2D or fast Fourier transform) is that spatial-domain data set is transformed into a fundamental sine wave, which displays the amplitude of the Fourier component, represented in grayscale (or color), as a function of frequency. Gabor transform utilize a filtration with a Gaussian kernel previous the Fourier transformation. This decreases noise but still provides access to image features such as edges, texture, blobs - and even inverse-transformations convert the transforms back to the spatial domain. Wavelet transforms or “windowed Fourier transform” assists in the denoising, compression, and fusion of images. The width of the window determines both the spatial resolution and the frequency resolution (Kolossváry, 2018).

Furthermore also image acquisition and reconstruction can be optimized with correlation to image segmentation and rendering, or feature extraction and feature qualification (Kumar, 2012). Traditional Feldkamp–Davis–Kress (FDK) reconstruction method, requires dense angular sampling in the data acquisition phase. Thus either the measurement times are longer, or the resolution of X-ray CT scans are lower. Purisha et al calibrated the degree of sparsity from a few dense-angle reconstructions in the 3-D shearlet transform domain and with this advanced method solved that issue (Purisha, 2019). Also handling of databases and data sharing for advanced informatics analyses utilizing novel approach belongs to radiomics evaluation (Kumar, 2012).

However, each of these processes may pose unique challenge. Optimum protocols for image acquisition and reconstruction have to be identified; segmentations have to be robust and is preferred to involve minimal operator input; or features have to be generated that robustly reflect the complexity of the individual volumes, but needs to be averted being overly complex and/or redundant. Further challenge could be the harmonization of informatics databases that allow incorporation of image features and image annotations optimized with statistical approaches to analyze them (Kumar, 2012).

By all ways we can state, that multiple testing with the same animal, combined with radiomic evaluation, have the possibility to provide more relevant biological information (Renaud, 2016; Szigeti, 2016; Szigeti, 2018; Lauber, 2017).

1.2. Radiomics improving data obtaining

Radiomics (and radiomics-based data handling, as well as evaluation methods) may improve gaining quantitative data about several fields of public health (Gillies, 2016). With radiomics evaluation, based on X-ray CT reconstructions, it is possible to detect early and in an advanced manner diagnose specific frequent diseases, such as coronary diseases as well as cardiac infarcts or lung cancers (Kolossváry 2018; Thawania, 2018). The same is true on inflammatory diseases of the gastrointestinal tract (GIT), or mental-neural diseases (for example schizophrenia and Parkinson's disease), based on functional MRI (fMRI) reconstructed data (Maneesh, 2018; Cui, 2018). Also predictive information about progression or outcome of diseases can be possessed utilizing radiomics. For example Parkinson's disease examined with 123I-ioflupane-dopamine transporter (DAT) SPECT with radiomics evaluation has improved the prediction of outcome significantly, see below (Rahmim, 2017).

1.2.1. Biological information in scope of radiomics study

Coronary CT angiography (CTA) detects histopathological coronary lesions and their characteristics are predictive indicators of subsequent major adverse cardiac events (MACE). To characterize atherosclerotic plaques, which are complex 3D structures the shape-based metrics are suitable (Kolossváry, 2018). Moreover, Napkin-ring sign (NRS) (synonym of thin-cap fibroatheroma) is a rupture-prone plaque in a coronary artery, comprising a necrotic core covered by a thin cap (<65 μm). Also NRS is considered as a predictive biomarker of MACE. Kolossváry et al. calculated 4440 radiomic features based on CTA and 20.6 % of them were significantly different between NRS and non-NRS plaques samples of patients with stable angina pectoris (Kolossváry, 2017).

The intensity, structure, texture/gradient, and wavelet features of a nodule on a chest CT show correlation with the malignant potential, and indicate prognosis and mutation status (Thawania, 2018; Aerts, 2014). Moreover, measures of heterogeneity, such as spiculation and entropy gradients are strong prognostic indicators of overall survival (OS) in patients with early stage lung cancer (Grove, 2015). Depeursinge et al. found a correlation between radiomic biomarker based on CT texture of nodule and disease free survival (DFS) (Depeursinge, 2015).

Indeed, texture features correlate to the heterogeneity of a nodule. For example lower values of Haralick entropy are in a granuloma while high entropy values are in an adenocarcinoma (Thawania, 2018). The fractal texture features of FD analysis were averaged over the tumor region and quantitative classification showed up to 83.3% accuracy in distinction between advanced (aggressive) and early-stage (nonaggressive) malignant tumors (Al-Kadi, 2008). The angiogenesis theoretically corresponds to the aggressive nature of a malignant tumor and in a large number are practical examples represented, corresponding to this theory (Kossmann, 2017). A spectacular example is for that the *A disintegrin and metalloproteinase 9* (*ADAM9*) gene, which is highly expressed in several cancer cell and is a potent metastasis-inducer, while promoting vascularization by inducing vascular endothelial growth factor (VEGF), inter alia (Kossmann, 2017).

Yoon et al. in a radiogenomics study identified adenocarcinomas with *ALK*, *ROS1* and/or RET fusion phenotypes utilizing X-ray CT and PET imaging with a sensitivity and specificity of 0.73 and 0.70, respectively (Yoon, 2015).

According to Cui et al, to detect schizophrenia is possible with MRI (fMRI) technique (Cui, 2018). The data were possessed by using both of high-resolution T1-weighted anatomical imaging and resting-state blood oxygen level-dependent-fMRI. Then functional connectivity was calculated for both groups, namely on group with first-episode schizophrenia patients and a healthy control group. The features were selected by Least Absolute Shrinkage and Selection Operator (LASSO) method, the clinical utility of its features and the generalizability of effects across samples were assessed using machine learning by training and validating multivariate classifiers in the independent samples (Cui, 2018). Parkinson’s disease examined with DAT SPECT and using 92 heterogeneity and texture radiomic features with Random forest (RF) analysis with 5000 trees was used to combine both non-imaging and imaging variables to predict motor outcome and evaluated using leave-one-out cross-validation has improved significantly the prediction of outcome (Rahmim, 2017).

Magnetic resonance enterography (MRE) is a leading radiological modality to monitor Crohn’s disease (CD) and based on that in the recent decade several indices, such as Magnetic Resonance Index of Activity (MaRIA), the Clermont score, the Crohn’s Disease Magnetic Resonance Imaging Index (CDMI), the Magnetic Resonance Enterography Global Score (MEGS) and the Lemann index was developed. However, each mentioned index has its advantages as well as disadvantages (Rozendorn, 2018). Thus new approaches are still warranted. Recently, based on radiomics features (possessed by utilizing MRI) Maneesh et al developed a novel biomarker, namely the Small Intestinal MRI Pathology Inflammation Score (SIMPle) in an animal model. The parameters correlate to histopathological findings and enabled the discerning of an inflamed group (similar to the human Crohn Disease), an inflamed group treated with dexamethasone, and a control group (Maneesh, 2018). Presumably those approach may indicate other inflammatory disease of the GIT.

Generally speaking, radiomics may provide predictive information about diseases, improve monitoring of therapy or even rehabilitation in the future, when further develops will be carried out.

1.3. Examined pathological conditions and environmental exposures

According to the World Health Organisation (WHO) between 20%–33% of people across the globe are affected by the disease of the locomotor organ (GBD, 2016). In 2011, the direct and indirect cost of musculoskeletal disorders was $213 billion (Bone and Joint Initiative USA, 2016).

According to the estimations, approximately one quarter of global mortality is caused by unhealthy environment including indoor, outdoor and occupational exposures, such as chemicals, air pollution and ultraviolet radiation (Prüss-Üstün, 2016). Hazard identification and risk assessments are carried out by health organizations with various methods. The US Office of Health Assessment and Translation (OHAT) as well as the WHO describe most of the methods (Chartresa, 2019).

1.3.1. Bone diseases

Bone diseases, including osteoporosis, Paget’s disease of the bone, osteogenesis imperfecta, rickets, osteomalacia, renal osteodystrophy, and hyperparathyroidism remain a major public health problem in developed countries.

In 2004, the total number of patients with bone diseases was estimated as more than 10 million only in the US, with rising trend line. The result is approximately 1.5 million fractures yearly and a significant financial burden to both individuals and society. Many of these costs are avoidable, since opportunities are known to effectively prevent, diagnose early, and treat properly bone disease throughout the lifespan (DHHS, 2004).

Despite the large numbers of individuals affected, the mortality is low as a direct result of bone disease. Although bone disease could be under-appreciated as an indirect cause of death. Hip fractures, are one of the most severe consequences of bone disease, but they seldom directly result in death. In 1999, hip fractures were listed as the cause of 12,661 deaths in the US (NCHS, 1999). This represents less than 4 percent of the number of patients who were hospitalized for hip fractures in that year (Popovic, 2001).

Still remarkable individual life quality loss and immense social burden (hospitalization, costs of nursing, lost work hours, etc.) are estimated. Early diagnosis and proper monitoring of therapies, as well as rehabilitation, lead to achieve improvement (DHHS, 2004).

1.3.1.1. Application of bone grafts

Bone grafting is the replacement of missing bone by a surgical procedure. Ideal bone grafts possess certain essential properties, such as efficacious and safe use, biocompatibility, appropriate mechanical/chemical attributions, cost-effectiveness, convenient usage, as well as production and availability in a large quantity (Chen, 2016).

Bone grafting procedures are carried out in the US yearly more than in 500.000 cases, according to an estimation in 2002 (Bucholz, 2002). Approximately nearly the half (48.6%) of all bone graft substitutes were implanted during spinal surgery. Also arthroplasty, trauma, and foot/hand cases all used considerable amounts of bone grafting products (20.1%, 19.0%, 12.1%, respectively) (Bostrom, 2005).

Although not all bone diseases can be improved utilizing bone grafts (neither the most frequent osteoporosis, as generally the bone diseases with metabolic background) but the monitoring of bone formation procedure in the surroundings of bone grafts corresponds to several generally relevant bone healing factors. For example transforming growth factor β1 (TGF-β1), bone morphogenic proteins (BMPs) and insulin-like growth factor 1 (IGF-I) and chondrogenesis- factors (for example transforming growth factor b (TGFb) super family fibroblast growth factor 2 (FGF-2) and also the aforementioned (IGF-1) (Khan, 2000; Puetzer, 2010). Moreover the effects of those factors are partly overlapping with each other (Massari, 2019). Therefore to investigate the in vivo results of the relevant factors is warranted, in order to provide early predictive information about bone and cartilage healing (Budán, 2018b; Budán, 2018c).

1.3.1.2 Rat tail model for monitoring bone healing

The rat tail model's major advantages are the accessibility of the bones (Ellender, 1988) and relative cost-efficiency compared to other animal models (Fitzgerald, 1983). In 1983, rat tail models were utilized to study bone growth, development and were also considered to represent bone remodeling process (Anat, 1983). Indeed, predictable and symmetric bone growth was observed (Hammond, 1970). Moreover, in an experiment, the applied force resulted in altered and asymmetrically grown bones (Storey, 1972). These data seemed to underpin the bone remodeling properties of rat species models. However, in 1998, Nunamaker highlighted that rats possess a primitive bone structure, lacking haversian systems (Nunamaker, 1998). Thus, the classical bone remodeling process of rodents with larger size (for example rabbits) or more advanced species (for example mammals), where Haversian systems are involved cannot been exactly modeled with small rodents. Still rat models could be utilized in bone healing tests since bone formation properties depend mainly on the aforementioned inflammatory and blood circulation factors.

1.3.1.3 X-ray computed tomography and other methods for imaging bone diseases

Bone-forming cells are characterized by their synthesis of a type I collagen matrix that is mineralized (Ducy, 2000). Several methods were developed to assess the mineralization with the growth of osteoblast and osteoblast-like cells or purified mineralized-bone material ex vivo. Bone biopsy histology employing Von Kassa staining (Bonewald, 2003), scanning electron microscopy (SEM) (Boyde, 1976) transmission electron microscopy (TEM) (Basdra, 1999), morphometric parameters of human subchondral bone samples were determined using less acquisition time and higher resolution, utilizing a novel sparsely collected data reconstruction method (see below) (Purisha 2019). For the seeking of completeness it is needed to mention the energy-dispersed X-ray microanalysis (EDX), dual X-ray absorptiometry (DXA), X-ray diffraction, micro X-ray CT, and 45-calcium (^{45}Ca) radioisotope uptake (Budán, 2018).

Noninvasive and/or nondestructive techniques are capable to provide more information about the macro- or micro-structure of the bone. X-ray CT is especially well-suited for measurements of bone density, owing to the high signal contrast between bone and soft tissue, explained by the nature of attenuation (see above) (Coles, 1995; Feeman, 2010a). So it is not surprising that the first applications of this technique have been in bone studies where the bone architecture and density during subclinical phase of osteoporosis and osteoarthritis was investigated. Several research groups have applied CT techniques to non-destructive evaluation of trabecular bone structure (Borah, 2001). Micro CT has been used to detect changes in bone 3 dimensional (3D) structure, measure bone volume and investigate microarchitecture as well (Buchman, 1998). Also micro-CT has also been used to assess the 3D architecture of trabecular bone in an experimental rat model for tumor-induced osteolytic defects (Kurth, 2001).

1.3.1.4. Single Photon Emission Tomography with ^{99m}Tc-Methyl diphosphonate tracer for bone scintigraphy

In clinical practice, bone scintigraphy is a widespread screening method, that is based on osteoblast labeling by ^{99m}Tc-Methyl diphosphonate (Tc-99m-MDP) (Chopra, 2007). Tc-99m-MDP accumulates in the bone by chemical adsorption and incorporates into the hydroxyapatite structure (Kanishi, 1993). Areas with high osteogenic activity are Tc-99m-MDP absorbers and can be identified with gamma camera (Kanishi, 1993). SPECT imaging with Tc-99m-MDP tracer has been used frequently in nuclear medicine for the in vivo diagnosis of abnormalities in bone formation and remodeling, including osteogenic tumors or metabolic bone diseases (Chopra, 2007; Kanishi, 1993; Fogelman, 1978).

1.3.1.5. Bone formation imaging evaluated with radiomics approach

Bone health can be monitored well, using X-ray CT and SPECT with Tc-99m-MDP tracer, as mentioned above (Coles, 1995; Chopra, 2007). Multimodal in vivo imaging is capable to provide anatomical and functional information simultaneously (Szigeti, 2018). This could be applied to obtain more quantified and comparable data. In a previous study, bone formation was investigated with multimodal NanoSPECT/CT in rat tail implant model (Aberg, 2011). The results have revealed that the bone formation is supposed to be detectable three weeks after bone graft insertion with both modalities (Aberg, 2011). Additionally, eight weeks following bone graft insertion, the healing process might still be ongoing as indicated by the increase in bone opacity along with the decrease of the standardized uptake volume (SUV) of Tc-99m-MDP (Renaud, 2016; Aberg, 2011). SUV is generally used in routine clinical practice. It indicates semiquantitatively the radiotracer uptake. (Most commonly, SUV is normalized by the patient's body weight, using the following equation: SUV = measured activity concentration [MBq/ml]/(injected activity [MBq]/body weight [g]). The healing process lasts 12-14 weeks following surgery (Renaud, 2016; Aberg, 2011). Thus, presumably those multimodal data acquisition methods utilizing radiomics-based data handling and evaluation methods may provide improved results in comparison with one-modular techniques, namely, the ratio of those descriptive parameters may be more informative on bone formation as stand-alone data. Further data may be possessed if trend lines are abstracted and compared utilizing regression analysis.

1.3.2. Environmental pollutions and public health

The environmental pollutants are present mainly in the air, soil and water.

Predominantly the air-pollutants expose living organisms through their lungs and airways. The soil pollutants are solved mostly by the water content of soil. Thus, ultimately soil pollutants exert through drinking water or consumed food their harmful effects. The disease burden of environmental pollutions in the recent time is immense and also its trend line is increasing (Faroon, 2012).

1.3.2.1. Air pollutants and lung diseases

In 2012, around 7 million people died - one in eight of total global deaths – as a result of air pollution (WHO, 2012). Those data include indoor and urban outdoor air pollution, which is responsible for 3.1 million premature deaths yearly (WHO, 2009) including mostly newborns and infants (see below) (WHO, 2005). In 2016, the air pollution is estimated to reduce the average global life expectancy by 1 year (Apte, 2018).

Air pollution induces a significant part of the mortality of COPD which is 2.55 million death yearly (Lopez, 2006). The same is true about the lung cancer, which causes 1.59 million deaths annually (Ferlay, 2012). Asthma is also strongly related to air pollution and has currently 300 million cases, who are mostly children (Bousquet, 2007).

Asthma has an immense costs, yearly 300-1000$ / patient (Braman, 2006). It is important to highlight, that the prevalence of the mentioned diseases is increasing constantly (Mannino, 2007; Braman, 2006).

The clinical classification of chronic obstructive pulmonary disease (COPD) severity into four stages has been proposed by guidelines based primarily on forced expiratory volume (FEV) (Jeffery, 1998). A composite measure index essentially based on clinical parameters - body-mass index, obstruction, dyspnea (Pauwels, 2001) has been shown to be more clinically relevant and better predicting mortality than FEV changes alone (Celli, 2004). Other clinical diagnostic processes in COPD are based on complete blood count, arterial blood gases, pulse oximetry and plasma Alpha-1-Antitrypsin concentration (Wright, 1988). The screening of COPD and asthma diseases, their early diagnosis and therapy with proper monitoring is extremely important (Bach, 2012; Celli, 2004), because significantly improved therapeutic efficacy is associated with early diagnosis, better quality of life and even with a reduced mortality (Jobse, 2011). Furthermore, COPD and asthma are good targets of screening, because their progression is slow. However, COPD, asthma and bronchitis have partly overlapping symptoms as well as similar pathologic features for example the tissues are inflamed and mucus production may be increased (Szigeti, 2016). In each of the distinct individual with specific aforementioned lung disease early pathological changes of airways and alveoli and altered volume of air is presented. This could be caused by the increasing quantity of narrowed airways and alveoli, which is caused by inflammation-related thickening of airway walls. Mucus or fluid, derived from necrotic cells inside the alveoli could also contribute to the disease process. Moreover, mucus is capable to form plugs, responsible for trapping air inside the alveoli and further formation of micro sized bubbles (Bossé, 2010; Moldoveanu, 2009). Early changes in obstructive pulmonary diseases and infectious or allergic inflammatory illnesses of the lower respiratory tract are mostly a mosaic-like pattern of mucous “bottleneck” formation in the terminal bronchioli and the destruction of the alveolar unit (Bossé, 2010).

On the other hand, lung cancer is progressive and has the leading mortality among cancers (Bach, 2012). The overall ratio of mortality to incidence is 0.87 (Ferlay, 2012). For that high lethality of lung cancer is responsible that the symptoms appear in the late stage and is often associated with metastasis (Khakwani, 2013; Duffy, 2013). Efficient early screening may lead to better survival of lung cancer. Thus, it is not surprising, that the geographical pattern of mortality is associated to the local air pollution profile (Ferlay, 2012).

These facts highlight the relevance of prevention (see below) (Budán, 2014a; Máthé 2015, Szigeti, 2016).

Air pollution, including smoking (Deja, 2014) or smog, containing sulfurous- and/or nitrous – gases combined with ozone (Tager, 1999) directly increases the incidence and severity of the aforementioned diseases (Wright, 2001). Cigarette smoke contains multifarious toxins, such as aromatic hydrocarbons (McNeill, 2006) heavy metals, for example Cd, mercury (Hg) (Agbandji, 2012). According to United States Environmental Protection Agency (EPA) sulfur dioxide (SO_2) is also among the leaders of air-pollutants like ground-level ozone precursors, such as nitrogen oxides and volatile organic compounds (VOC) related mainly to fuel combustion (EPA, 2014a; EPA, 1996). It is also important that even a short-term exposure with SO_2 can lead to bronchoconstriction and worsen asthma symptoms (EPA 2014b).

1.3.2.1.1. X-ray computed tomography and other methods for imaging lung diseases

The changes in morphology and structure of lung tissue can be well detected with X-ray CT based on size and distribution of low attenuation areas (Yamashiro, 2011). Thus quantitative X-ray CT may have significant value as a non-invasive means to identify existence and distinct subtypes of COPD (Jobse, 2011) or other lung diseases for example lung cancer (Al-Kadi, 2008; EPA, 1996).

Pulmonary diseases (bronchitis, asthma, etc.) share important common features such as the inflammation of tissues and overproduction of mucus (Williams, 2006) or emphysema, and small airway remodeling, etc. (Churg, 2008; Jeyabalan, 2012). Presence of mucus in the airways leads to increased tissue densities while the destroyed walls of airways and alveoli increase patchy air trap formation and decrease density parts of the bronchi-alveolar units examined with X-ray CT (Jeyabalan, 2012). Pienn et al. distinguished patients with and without pulmonary hypertension (PH) with dynamic contrast-enhanced computed tomography (DCE-CT) (Pienn, 2014). Al-Kadi and Watson (2008) distinguished tumor and blood vessels based on CT attenuation (using CM) to perform fractal dimension (FD) analysis, see below (Al-Kadi, 2008).

1.3.2.1.2. Hindrances and distorting factors of X-ray CT for imaging lung diseases

If there are many inflamed or otherwise damaged lung tissue parts spread all over in the lungs in particular if they are small, the gained CT data can be obliterated by the overall high attenuation resulting from these small high-density spots that veil useful information. To highlight the fine aspects of COPD, such as emphysema, state of small airways, pulmonary hypertension, genetic factor (for example Alpha 1-

antitrypsin deficiency) and chronic bronchitis could not been fully remodeled using animal experiments (Lucas, 2013).

Gating by holding the breath in patients with COPD or asthma (or in patients with otherwise decreased lung capacity) is unpleasant or even impossible. Furthermore in such patients the possibility of unwilling motion artifacts is per se increased.

Morphogenic pattern of the human lungs are mostly symmetrical and branches dichotomously (Koblinger, 1985) contrary to the lungs of rodents, which is predominantly monopodial (Yeh, 1979). This difference could distort the direct translation of the results of experimental animal models evaluation methods into human clinical use (Szigeti, 2016).

1.3.2.1.3. Radiomics evaluation of air pollution induced lung damage in mice model

Because morphology and structure of lung tissue can be well detected with X-ray CT based on size and distribution of low attenuation areas, also specific features of lung diseases may provide a partly different, and partly overlapping pattern (Yamashiro, 2011). Thus, quantitative X-ray CT may have significant value as a non-invasive means to identify existence and distinct subtypes of COPD (Jobse, 2011) or other lung diseases for example lung cancer (Al-Kadi, 2008). According to comprehensive details, CT examinations, detecting the alterations of X-ray absorption quantities of diseased lung tissue, are supposed to result in increased number of voxels both with higher density (mucous tissues) and with lower density (cavities) in the reconstructed three-dimensional tissue density volumes. Spatial density patterns in small pulmonary regions could be very informative for diagnostic purpose.

Specific distributions of number of voxels in function of X-ray attenuation values, abstracted as histograms may be informative. Thus, FD distributions of voxels with similar X-ray attenuation values and also the aforementioned lacunarity can be calculated (Annadhason, 2012; Al-Kadi, 2008). FD has certain limits during analysis of “less or more branching nature” of structures (Mandelbrot, 1989; Petrou,

2006) including the respiratory organ (Nagao, 2002). However, the aforementioned lacunarity and other parameters are outside of the scope of this dissertation, since FD distribution pattern of voxels with same attenuation values, may alone represent lung diseases or effects of air pollutions, respectively (Petrou, 2006).

Radiomics approach carries both the possibility to improve early diagnosis of lung diseases such as COPD, asthma, lung cancer and to offer yet missing, robust and valuable “imaging biomarker data” for the testing of new therapeutic agents: in consequence, to improve therapy efficiency (Szigeti, 2016; Budán, 2014a; Máthé 2015).

FD calculation enables to overcome about the difficulties of different branching pattern of human and rodent airways (Fazzalari, 1996; Shlesinger, 1991; Nagao, 2002; Nagao, 2001; Helmberger, 2014).

1.3.2.2. Soil and water pollutants

Soils offer valuable goods and services such as carbon storage and water filtering. In order to ensure a sustainable environment and society, these goods and services need to be maintained (Lavelle, 2006; Morvan, 2008). Assessment of soil quality, defined as the ability of soils to deliver ecosystem services in a sustainable way (Doran, 1994), has become a major research topic in the last two decades (Ruiz, 2011). Nevertheless, validated tools to obtain information on degradation and/or remediation of soil properties and functions to inform state agencies, as well as monitoring networks (European Commission, 2006) are needed. To date, soil characterization has generally been based on physical and chemical parameters (Morvan, 2008; Kibblewhite, 2008).

Generally speaking, different contaminants have different - but characteristic, and even sometimes overlapping - effects on human health and the environment - depending on their properties, such as potential for dispersion, solubility in water or fat, bioavailability, carcinogenicity and so forth (Panagos, 2013). However, if pollutants cannot be completely excreted, due to lack of metabolizing biochemical reactions and in the same time those pollutants are lipophilic, then the so called biomagnification process may occur. Vegetal foods may accumulate pollutants and stock-raising as well as fishing worsens this with the aforementioned biomagnification process, leading to even ca. 10.000 times increased contaminant content in meat products in comparison to the concentration of polluted waters (Gobas, 1993; Bruns, 2001; Elinder, 1992). For example, redworm (*Eisenia fetida* S.) exposed to 80 ppm cadmium (Cd) for 60 days has accumulated as much as 200 µg/g dry tissue weight Cd quantity (Scaps, 1997).

Heavy metals and mineral oil are the main contaminants contributing around 60% to soil pollution, derived mostly from municipal and industrial wastes or from the commercial sector (Panagos, 2013). Heavy metals have been used by humans for thousands of years. Several adverse health effects of heavy metals have been known for a long time. Still exposure to heavy metals continues and is even increasing in less developed countries, though emissions have declined in most developed countries over the last 100 years (Järup, 2003). The main anthropogenic sources of heavy metals exist in various industrial point sources, for example, present and former mining activities, foundries, smelters, and diffuse sources such as piping, constituents of products, combustion of by products, and traffic related to industrial and human activities (Guvenç, 2003).

Any metal (or metalloid) species may be considered as a "contaminant" if it occurs where it is unwanted, or in a form or concentration that causes a detrimental human or environmental effect, such as lead (Pb), Cd, Hg, arsenic (As), chromium (Cr), copper (Cu), selenium (Se), nickel (Ni), silver (Ag), and zinc (Zn) (U.S. EPA, 1997). For example, some heavy metals, such as hexavalent chromium (CrVI), manganese (Mn), and Pb, as well as Cd and arsenic (As) inhibited the 8-oxo-Gua excision repair system in rats (Hirano, 2010). Other less common metallic contaminants including aluminium (Al), cesium (Cs), cobalt (Co), Mn, molybdenum (Mo), strontium (Sr), and uranium (U) may cause local, but important contamination (McIntyre, 2003). Thus, soil pollution requires reliable monitoring, which provides results as quick as possible.

1.3.2.2.1. Cadmium

Spectacular disaster was the infamous and deleterious „itai-itai disease" caused by severe chronic Cd poisoning. It has occurred in great numbers due to an environmental pollution with Cd in the Jinzu River basin in Toyama district in Japan. The osteomalacia symptom was the most severe in postmenopausal women, because decreased renal function (see below) inhibited the reabsorption of calcium (Ca^{2+}) and phosphate (PO_4^{3-}) ions. Despite the extensive interventions (see below) ordered to ameliorate harm even nowadays people are afflicted, who live in that area (Aoshima, 2012). Nevertheless, Cd content of soils in Europe since 1960 have increased until 1980, when its primary reason was recognized, namely the use of some types of fertilizers (with high Cd content), just like sewage sludge (Jensen, 1992). For example in superphosphate fertilizer the Cd content was as much as 7.25 ppm (Schroeder, 1963). Even actually Cd pollution represents one of the foremost important aspects of agricultural soil quality (Liu, 2016; Wang, 2015). Generally speaking, the major source of diffuse Cd pollution are fertilizers, produced mostly from ores, abundant in PO_4^{3-}. The Cd content of those fertilizers may reach drinking water with several ways. Therefore, the agricultural use of wastewater and sludge is forbidden. Indeed, Cd can accumulate as we have mentioned earlier describing biomagnification process, and even exert thereby ecological effect (Larison, 2000).

Despite that, the first symptom of rare acute Cd poisoning is pulmonary edema, the kidney is considered to be the critical target organ for the chronic cases, such as the general population as well as for the occupationally exposed workers (see below). Within the kidney, the cortex is the site where the first deleterious effect occurs. Long-term exposure to Cd causes renal tubular dysfunction with proteinuria, glucosuria, and aminoaciduria, as well as histopathological changes, in both experimental animals and humans (Rea, 2018). Risk factors of Cd poisoning is detailed below.

Cd toxicity also can induce carcinoma, teratogenesis, growth retardation, hypertension, peripheral neuropathy, and impaired reproduction (Takács, 2018). Obviously, the carcinogen effect is the most well-known as well as severe effect of Cd toxicity. The underlying multifarious causes partly corresponds with direct enzyme and cell damages, inter alia - and the enzyme function loss correlates to our study (see below.)

The hypertension is caused by Cd, which is capable to disturb renine-angiotensine system (RAS) (Takács, 2018; WHO, 1987). Varoni MV et al. elucidated in rats that the Cd decreases kallikrein level and thereby activate brain RAS, contributing to the central control of pressor response to induce intracerebroventricular (ICV) hypertension (Varoni, 2010). Moreover, Cd inhibits the release of acetylcholine, inhibits monoamine oxidase (MAO) and adenylate cyclase enzymes, also inhibits the uptake of choline, catecholamines, γ-aminobutyric acid (GABA) and glutamic acid, but activates cholinesterase enzyme – leading to peripheral neuropathy (Rea, 2018). Cd contributes to infertility, which is a recently growing problem in the developed countries. An increase in Cd (and Pb) levels was observed in infertile men. Cd and Pb concentration in the semen of oligoasthenospermic men correlated negatively in a significant manner with sperm concentration as well as with motility of sperm (Pant, 2003).

The Cd increases the risk of kidney and prostate cancer in a dose-dependent, stochastic manner, in multifarious pathways (Hirt, 2003; Martelli, 2006). Here we can mention, that Cd disturbs hormone functions, for example decrease dihydroxy-vitamin D production and activates redox sensitive glucocorticoid (Hirt, 2003; Martelli, 2006). But more important is that in both plants and animals Cd follows a Trojan horse strategy, because it mimics and also displace divalent metallic ions, such as Ca, Cu and iron (Fe). Thereby Cd also increase the presence of reactive oxygen species (ROS) (Hirt, 2003; Martelli, 2006).

ROS reacts through electrophilic intermediates quickly and thereby exerts damage to cells (Hirt, 2003; Martelli, 2006). Another underlying cause is that Cd increase lipid peroxidation, which induces oxidative damage caused directly also by ROS (Novais, 2011). Indirect damage contribute to this, namely that the most important glutathione-S-transferase (GST) is down-regulated by Cd (Novais, 2011). Furthermore, ROS inactivate other enzymes (SOD, CAT, GR, GPX) and inhibit mismatch DNA repair (Hirt, 2003; Martelli, 2006) and even damage DNA directly (Novais, 2011). Cd reacts with thiol-groups and thereby has a potential to deplete glutathione (GSH) the substrate of the ROS quenching GSTs (Novais, 2011; Pinkus, 1977) leading to incomplete phase II biotransformation. This harmful effect is demonstrated with chalcones (Lee, 2006) or chalcone analogue E-2-(4’-methoxybenzylidene)-1-benzosuberone (MBB), which are mostly in vitro chemopreventive (Perjési, 2000) but with the Michael reaction they can deplete GSH (Budán, 2009a; Budán, 2009b). Both of the environmental carcinogen N-methyl-N-nitrosourea (MNU) or 7,12-Dimethylbenz[a]anthracene (DMBA) liberate ROS (Budán, 2008a; Budán, 2008b; Fuller-Espie, 2011). In an experimental mice model the gene expression pattern of examined *HA-RAS* and *C-MYC* oncogenes and of *P53* tumor suppressor gene indicated the deleterious effects of MNU and DMBA (Budán, 2009b; Budán, 2008a; Budán, 2008b). However, if lacking GSH, the carbonium cation reacts with cellular macromolecules, such as lipids, proteins, or even alkylates DNA, and it prefers in a site-specific manner the mentioned relevant proto-oncogene *HA-RAS* and activates it (Budán, 2008c). Thus, according to the mentioned literatures, cell damage caused by Cd is obvious (Novais, 2011).

Cd can be taken up foremost through the lungs and the second most relevant way is through the gastrointestinal tract. For the general population not living in industrially polluted areas, Cd intakes from air are unlikely to exceed 0.8 μg/day (JECFA, 1989). Cigarette smoking increases indoor Cd concentrations. The average daily exposure from cigarette smoking (20 cigarettes a day) is 2–4 μg of Cd (Ros, 1987; WHO 2011). Cd concentrations in unpolluted natural waters are usually below 1 μg/l (Friberg, 1986). However, specific condition may increase Cd concentration in drinking water, see below. Cd levels in foods, namely fruits, meats and vegetables are usually below 10 μg/kg, in liver 10–100 μg/kg and in kidney 100–1000 μg/kg. In cereals Cd levels are about 25 μg/kg wet weight. In 1980–1988 the average Cd levels in fish were 20 μg/kg wet weight. Much higher Cd levels were found in shellfish (200–1000 μg/kg) (Galal-Gorchev, 1991).

The dietary daily intake of Cd has also been estimated to be in the range 10–35 μg (Galal-Gorchev, 1991). An average American accumulates 30 mg Cd in his body, but a smoker the twice of that quantity (Perry, 1976). However, in contaminated areas in Japan, daily intakes in 1980 were in the range 150–250 μg, based on measurements of Cd in feces (Friberg, 1986).

Cd in blood plasma is initially bound to albumin and is preferentially taken up by the liver. Cd induces the synthesis of methalothioneines (MTs) in the liver and a few days after exposure the MT-bound Cd is excreted in the blood plasma. However, Cd-MT complex is known about low molecular weight (6-7000 kDa) and therefore it is efficiently filtered through the glomeruli, then taken up in renal tubules by pinocytosis and subsequently degraded in lysosomes, thereby releasing Cd which stimulates de novo synthesis of MTs but also binds to reabsorbed MT. Ultimately, catabolizing and rebinding are continuous and prevent excretion of Cd (Nordberg, 1984). Thus, Cd accumulates in the human kidney over the entire lifetime, depending on other factors, such as other nephrotoxic agents (for example As) or gene expression of MT or autoantibodies against MT (Nordberg, 2012; Perry, 1976). Indeed, 5-7 times less Cd content was observed in the liver, then in the kidneys and even less in the pancreas and the lungs (Koch, 1956).

In summary, Cd exposure is needed to be minimized. Exposure minimization requires the use of effective monitoring methods and systems (Aoshima, 2012). For the purpose of monitoring the Cd exposure, still cost-effective and/or fast techniques are warranted. Cd exposure can be monitored with several in vivo tests using a large amount of biomarkers.

1.3.2.2.2. Earthworm model for monitoring soil pollutants

However, soil organisms are known to respond to multiple impacts and to react quickly to natural and anthropogenic stresses, and could, therefore, be used as early warning indicators (Cortet, 1999; Sousa, 2006). Among terrestrial invertebrates, earthworms (*Oligochaeta* and *Annelida* species) are “keystone” participants of soil ecosystems. Earthworms are distributed world-wide, have with a short life cycle and have a wide temperature and moisture tolerance range (Dominguez, 2004). Their direct contact with natural soil pore constituents and soil water makes them ideal for environmental monitoring (Gerencsér, 2010). The animal tests endpoints are mostly the alteration in body mass and in reproductive capacity (Gerencsér, 2010; Brousseau, 1997; Sauvé, 2002). Redworm (*Eisenia fetida* S.) has been recommended by the Organisation for Economic Co-Operation and Development (OECD) for testing chemicals since 1984 (OECD, 1984). Since 2009 juveniles (10–12 days old) *Folsomia candida* are required by the OECD standard test guideline No. 232 (OECD, 2009). However Guimarães B. et al. developed the test further utilizing eggs of *F. candida* (Guimarães, 2019).

Earthworms are sensitive to metallic pollution for example to Cd, which can be detected in 0.6 mg/kg in soil (while LC_{50} is 1000 mg/kg) (Xiaohui, 2012) which delays their sexual maturation (Spurgeon, 1996), slows down their growth (Spurgeon, 1999), modifies enzymatic activities (Łaszczyca, 2004), and gene expressions (Ricketts, 2004; Brulle, 2006; Brulle, 2007). Furthermore, earthworms are tolerant to toxic heavy metals due to distinct metabolic pathway that allows the bio-accumulation of Cd to yield body burdens in excess of 1/1000th of total dry body weight (Stürzenbaum, 2001). Thus, a wide range of heavy metal concentration can be traced in earthworm models, which are widely used as model organisms for detection of soil pollution.

Non-invasive immobilization techniques are needed as well to carry out *in vivo* imaging techniques. The morphological parameters in the *E. hortensis* and *L. terrestris* can be detected by using MRI, if there is a noninvasive anaesthetic method. However, the loss of coeloma is required to be minimized, as well as influencing hexokinase reaction needs to be avoided to enable FDG PET imaging (Budán, 2014). This includes the quantity of hexokinase reaction's substrates, regulating co-factors, or even the same factors of correlating reactions, for example ratio of oxidized and reduced forms of nicotinamide adenine dinucleotide (NAD^+/NADH ratio) would be presumably changed by ethanol intake, since ethanol is a nutrient with caloric value about 7 kcal/gram (Cederbaum, 2012).

Furthermore the intestines of earthworms are needed to be emptied to enable proper MRI signals.

Utilizing radiomics approach, the effects of environmental factors on living organisms may be observed in a more informative manner, than with the aforementioned one-modal imaging methods utilizing simple reconstruction with visual data evaluation. If organs of earthworms can be visualized in order to possess anatomical data utilizing SPECT or PET modalities, with proper tracers, and compare them to control, that approach could be capable to provide information about physiological functions, which are the results of numerous biochemical reactions, altered by exposure.

2. OBJECTIVES

In order to fully harness all opportunities of radiomics for more sensitive detection of harms to public health, the author has conducted several studies reported in this work. The general intention of these studies is to present a spectrum of radiomics methods. One end of this spectrum is testing imaging for possible individual screening approaches that are amenable to public health measures. The other end of this spectrum in radiomics is investigation of environmental systemic readouts that would be used for monitoring.

The particular purposes of the presented studies were to establish novel experimental set-ups, using animal models with proper new radiomics evaluation methods, in order to elucidate more relevant biological information, than already existing approaches. This may enable statistically significant discerning of otherwise not separable experimental data, based upon forming metadata from examined biological parameters. That method could virtually increase robustness, but practically enables decreasing the necessary sample number of animals, in coherence with the European Union (EU) directive 2010/63/EU on the protection of animals (Hartung, 2010).

The purpose of this study was to find a new radiomics evaluation method, based upon morphological bone X-ray attenuation and physiological time-related bone healing feature parameters that supplies researchers with accurate data regarding the bone healing properties. In the presented works, quantitative bone healing parameters of poly (methyl methacrylate)-based bone cement graft (PMMA) and albumin coated, sterilized, antigen-extracted freeze-dried human bone grafts (HLBC) were examined and compared, utilizing a bone healing model in caudal vertebrae (C5) of rats (Blazsek, 2009).

An additional goal was to develop rodent models to detect early the effect of air pollutants on the lungs utilizing X-ray CT with radiomics data evaluation to follow-up utilizing an automatic numeric characterization of air pollution affecting the respiratory organ. If the X-ray CT based spatial attenuation data of respiratory organ evaluated with the novel tested radiomics approach can enable the early distinction of harm sources, then also early diagnosis of lung diseases may be based on this method. Thus a potential clinically translatable mathematical algorithmic method using simple CT scans evaluated with calculation of FD number could be established (Fazzalari, 1996; Shlesinger, 1991; Nagao, 2002; Nagao, 2001; Helmberger, 2014).

In this dissertation, among soil pollutants, the Cd was studied with the purpose to develop in vivo animal test systems to detect soil contamination early, and in a reliable and economical manner (Budán 2013a; Budán 2013b; Budán, 2014b). Firstly earthworms are needed to be immobilized without influencing hexokinase reaction to investigate with in vivo FDG PET/MRI modalities the biological properties of earthworms, afflicted by Cd pollution. However test animal's size is required to enable proper resolution to monitor specific relevant organs (for example kidneys, hearts) in morphological tests. Similar relevance of relatively large sized *E. hortensis* and *L. terrestris* as that of *E. foetida* is proven in environmental toxicity models (Leveque, 2013). Then calculated trend lines and/or ratios of quantitative and time-related parameters, could represent the effects of noxious factors.

3. MATERIALS AND METHODS

3.1 Animal models

All procedures were conducted in accordance with the ARRIVE guidelines and the guidelines set by the European Communities Council Directive (86/609 EEC). The animal experiments were also reviewed and approved by the local authorities (Committee on the Ethics of Animal Experiments of the Semmelweis University, permit number: PMK ÉBÁI-XIV-I-001/29-7/2012) according to Hungarian animal protection laws in accordance with EU guidelines.

3.1.1. Rat model for bone grafts

Two groups (n=5) of female Wistar rats (Crl(Wi)Br, Charles River; 650–950 g from the breeding colony of Semmelweis University (Hungary) were kept in light controlled, air-conditioned rooms and fed *ad libitum*.

The surgical model of Blazsek et al. was applied, described briefly below (Blazsek, 2009). In spongious model of Blazsek et al., rats were anesthetized with sodium pentobarbital (Nembutal (Sigma-Aldrich) 40 mg/kg body weight (b.w.), by intraperitoneal (i.p.) injection). The tail above the C4 vertebra was ligatured to control bleeding during surgery. The tail was disinfected, then was partly removed after the C5 vertebra. A 5–6 mm incision was made at the level of caudal vertebrae (C4–C5). The skin was retracted and the vertebrae were exposed under sterile conditions. In the exposed central surface of C5, a 1 mm diameter and 5 mm deep hole was formed using an electric drill, corresponding to the size of a titanium screw. Subsequently, a hole was made (2.0 mm diameter and 3.5 mm depth) creating an "empty" cylinder, which allowed 360° rotation. Screwtype titanium implants (1.2 mm in diameter) were fabricated and their surface roughened using sandblasting (Full-Tech Company, Hungary). Sterilized screws were introduced into the 5 mm deep thin hole. Following insertion of the implant the skin was repositioned over the implant and tightly sutured. The surgical wound was protected aseptically by a plastic methyl-methacrylate butyl-acrylate butyl-methacrylate copolymer, diisooctyl phthalate film layer (Plastubol®, Pannonpharma Ltd. Hungary). Rats were kept in individual cages to insure appropriate hygiene and wound healing during the first two weeks following surgery. In each animal, 3 weeks after surgical intervention, the titanium implant was removed and the remained hole was filled with the experimental materials (**Fig. 1**), see below (Blazsek, 2009).

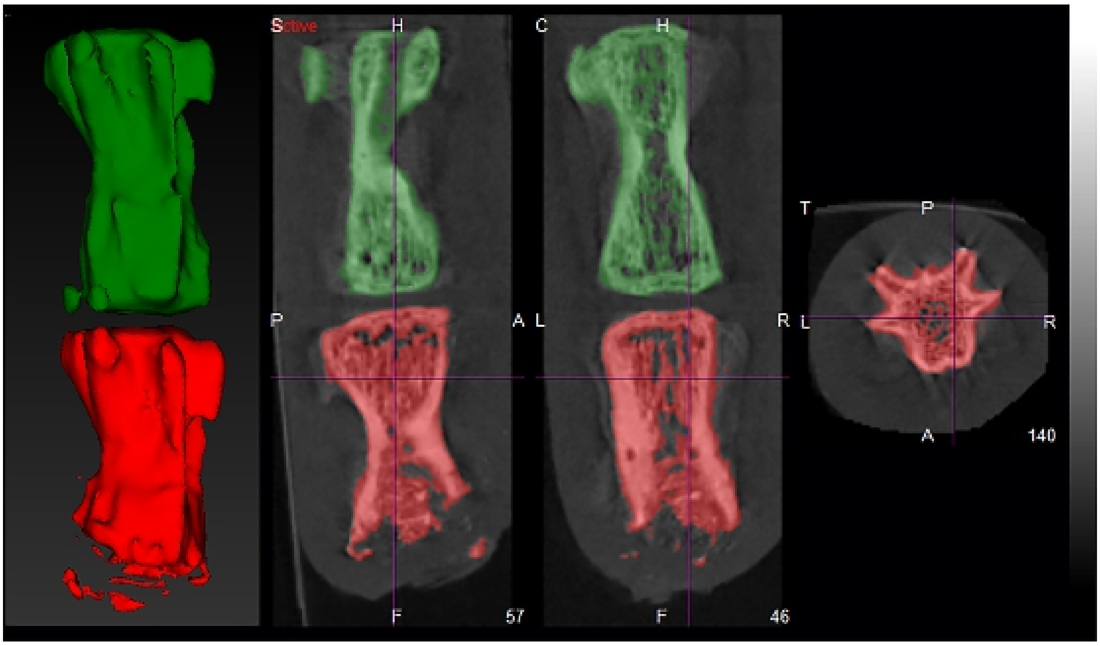

Fig. 1. Structure of caudal vertebrae of treated rats at starting point. The C5 vertebra (red color) was treated and filled with a bone graft which was selected as VOI for evaluation of CT. The green colored C4 vertebra show the VOI of control.

After the experiment, animals were killed by cervical dislocation. Autopsy was carried out in order to detect potential abnormalities for example inflammation.

3.1.1.1. Bone grafts

In this study, one female Wistar rat group (n=5) were treated with chemically sterilized, antigen-extracted HLBC (West Hungarian Regional Tissue Bank) and one group (n=5) with PMMA-based cement (Vertebroplastic, DePuy, USA) experimental materials. The HLBC were pretreated; a human serum albumin coating method (200g/1000ml, BIOTEST) was applied (Weszl, 2012).

3.1.2 Mice lung model

In our study, three groups of Balb/CBYJ female mice were used. In each group, we used 6-8 weeks old, 18-22 gram weight animals. Their exposure was performed in a plexi-glas inhalator chamber (30 cm × 30 cm × 50 cm). One group (n=5) was treated with inhalation of sulfur dioxide gas (SO_2) 2% v/v (referred as SDO group) and a further group (n=5) was treated with air-diluted fresh mainstream cigarette smoke from '3R4F' Reference Cigarettes (Kentucky Tobacco Research & Development Center, USA) mixed with ozone-air gas mixture (50 mg/h, 3.7 liters per minute dilution with air) referred as SAO group. Cigarettes with a shortened filter only (approx. 2 mm) were smoked according to our protocol (1 puff/9 sec of 3 sec duration and 40 mL volume). SAO group received one 20 minutes long exposure on first, two 20 minutes long exposure on second and three 20 minutes long exposure on the other remaining days. A control (CON) group (n=6) was also used, treated with the inhalation of filtered and humidified (30-40 %) air at laboratory temperature (24-26 C°) under the same conditions. The treatment durations were 14 days long then imaging was carried out. An untreated mouse was imaged too, for the sake of representation of attenuation profile of the chest (**Fig. 2 A, B, C, D, E, F, G**).

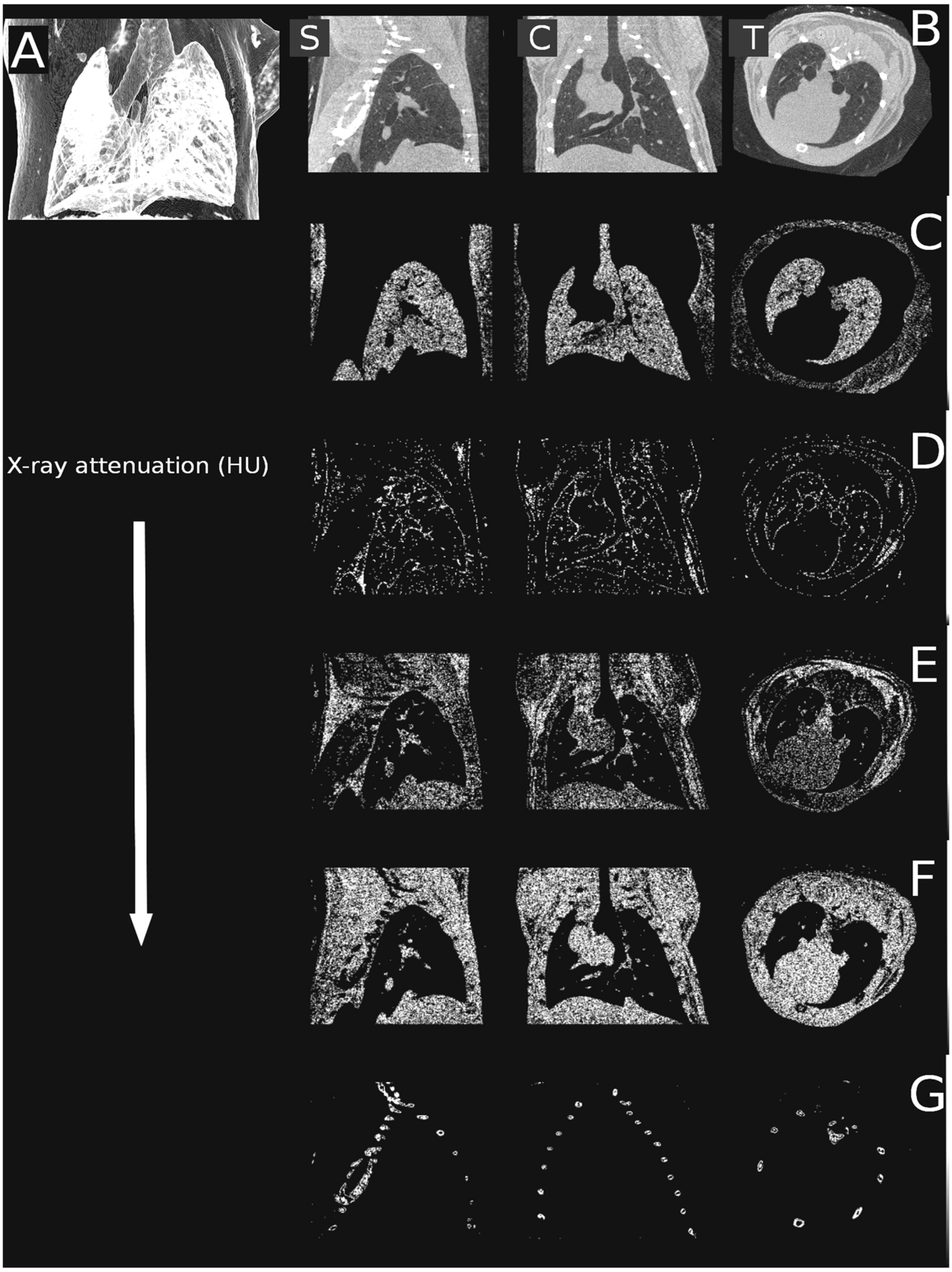

Fig. 2. The reconstruction of the lungs of an untreated mouse shown with the sole intent of representing the attenuation profile of the chest. Minimum intensity projection was applied in (**A**), sagittal (**left B**), coronal (**center B**), transaxial (**right B**) planes. Certain attenuation ranges were abstracted from these slices in sagittal, coronal and transaxial planes. The following HU ranges and organs are represented as: (**C**) −700 – -400 relative HU (lung parenchyma), (**D**) −100 – +200 relative HU (pleura, endothoracic fascia, epipleural fat and interlobar fissures), (**E**) +200 – +500 relative HU (respiratory- and heart muscles, diaphragm), (**F**) +500 – +800 relative HU (blood inside the vessels, aorta and heart, lymphatic fluid and interlobar fissures), and (**G**) +1400 – +3800 relative HU (bones).

During the CT scans animals were constantly anesthetized using a mixture of 2.5% isoflurane and medical air, and their body temperature was maintained at 38°C. One image acquisition was taken 4.5 minutes.

To preserve clinical translatability, for example to include realistic high-level noise that is often present in clinical patient CT acquisition settings where often also no breath gating is applied, we decided to analyze non-respiration gated data sets of mice.

3.1.3. Earthworm model

Earthworms (*E. hortensis* and *L. terrestris*) were kept at 20 ± 2 °C in plastic boxes (diameter 8.8 cm), with small ventilation holes and ten animals per box. Soil in the boxes was kept moist and contained 30% of farmyard horse manure.

We examined the possibility of keeping earthworms alive without earth to empty their intestines. The essence of pre-treatment is that earthworms were kept on Ringer solution instead of earth. Drewes and Pax developed a pre-treatment Ringer salt solution for earthworms (Drewes, 1974). This Ringer solution was modified and applied in our experiment (for details please see **Table 1**). The Ringer solution was changed daily. The buffer level in the boxes was sufficiently low to allow the earthworms to keep contact with air. The sucrose in the Ringer nourished earthworms and the water content kept their body moist. Earthworms were kept in separate boxes and their body mass and the mass of their excrements were monitored daily (Budán 2013a; Budán 2013b; Budán, 2014b).

3.1.3.1. Pre-treatment of earthworms

To provide data about the potential effect of a four day pre-treatment on the *E. hortensis* earthworms, two groups (n=10) were examined. In both groups, the earthworms were kept in Ringer solution (immersed in 1 mL x 4 mass (g) of the earthworm) in a box (diameter 8.8 cm). We also provided a solid polystyrene plate as we wished to test its effect as cover and ground that prevented their bodies to be fully immersed if they moved onto the plate in the box. Group A (n=10) earthworms were examined in the following way: a polystyrene plate was put into the box (**Fig. 3.A**). Earthworms in the control group B (n=10) were similarly treated as group A, but group B differed that polystyrene plates were missing (**Fig. 3.B**) (Budán, 2014b).

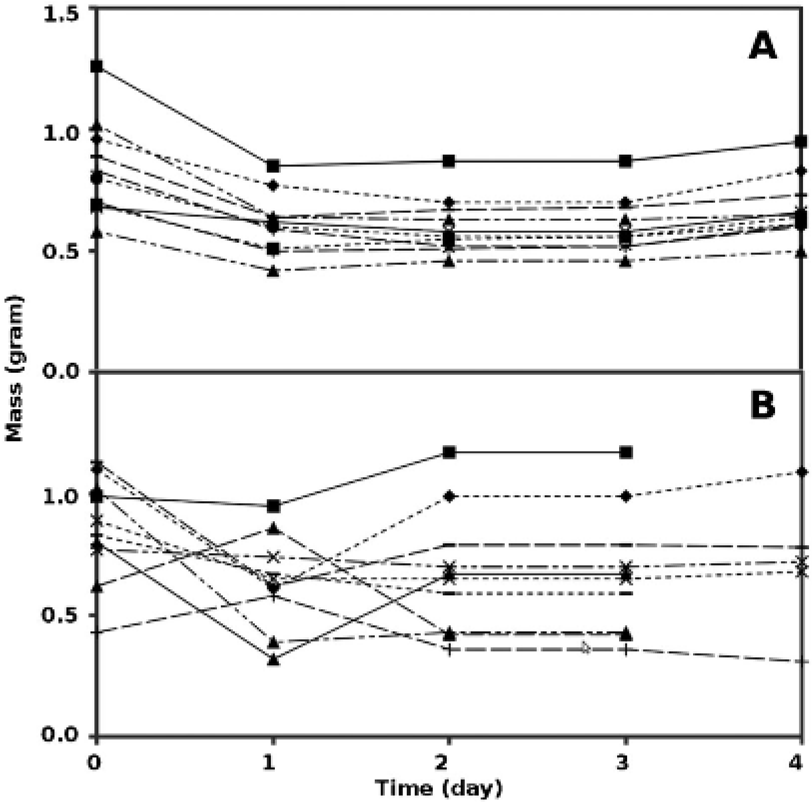

Fig. 3. Individual earthworm's body mass (g) alteration caused by keeping them in Ringer solution. (**A**) Polystyrene plates present (n = 10). (**B**) Polystyrene plates absent (n = 10).

3.1.3.2. Immobilization of earthworms

The *E. hortensis* earthworms were considered to be immobilized when they were completely paralyzed and they also not reacted on touching them. The time of immobilization was considered to be the time range from the beginning of the immobilization until the time point when immobilization ceased (for example they reacted with moving if their body was touched). We checked their state in each half minute by smoothly touching them.

Ethanol (96.7 %) was added into the bath of Ringer solution gradually. (The same modified Drewes and Pax Ringes solution was used (Drewes, 1974) as by the pre-treatment for MR imaging with the purpose to avoid soil in the intestines of earthworms). Animals were kept away from direct contact with 96.7 % ethanol. According to Petrics and Larsson, 8 % ethanol could be used to anesthetize earthworms (Petrics, 1986). Similarly to ethanol application we experimented with propan-2-ol added into the Ringer solution in 7-8 equal boli in each five minutes until 3.5-4.0 V/V% was reached. With careful administration, minimal distress was caused to the animals and thereby the excretion of coelomic fluid was avoided.

The airtight box tested for the general anesthetics was used to extend the immobilizing effect of alcohols by injecting 10 ml of 30 % propan-2-ol into the bottom of the box. An earthworm holder bed placed in a 50 ml Falcon tube was constructed with dual purpose: the first purpose of this holder bed was to keep the experimental animals from sliding inside the Falcon tube. The other goal was to separate animals from alcohol, but in such a manner that the vapor of alcohol was in the same airspace as the animals. Furthermore the box enabled us to move the animals from one desired imaging modality to the other one without the animal position changing related to the imaging bed (Budán, 2014b).

3.1.3.3. Cadmium exposure of earthworms followed up with in vivo imaging

Environmental harms such as poisoning with Cd could be detected in earthworms *via* elucidating the difference between an unpolluted control and a Cd polluted sample group's metabolic changes (for example in correlation with enzyme activity changes and/or depletion of their substrates). By utilizing FDG PET, the hexokinase reaction could be followed up. However to achieve comprehensible detection method, firstly the pharmacokinetic attributions of the radio tracers FDG in intact earthworms, in a control group, were examined to decide if those tracers reached the relevant organs, for example the kidneys (Budán 2013a; Budán 2013b).

To visualize organs with higher resolution, larger sized earthworm *L. terrestris* species was used. Also *L. terrestris* is more suitable to investigate Cd exposure, because according to the ecological category *L. terrestris* is a typical anecic earthworm (Domínguez, 2018) and - unlike the *E. hortensis* - the *L. terrestris* possess eleocyte in a less number (Plytycz, 2011) and therefore it is more sensitive to heavy metal pollutants (Plytycz, 2011). The other underlying cause of it is that in *L. terrestris* not only a few quantity of eleocytes are represented, but they even contain less heavy metal-protecting riboflavins than the eleocytes of *E. hortensis* (Mazur, 2011).

The intestines of earthworms were emptied while keeping them in Ringer solution as described above, with a specific modification, namely the applied Ringer solution was lacking TRIS buffer, which forms complex compounds with Cd. The purpose of earthworm Ringer was to avoid chemical reactions of Cd with humic and fulvic acids, which could be abundant in soil samples. Also the potential adsorption of Cd on the surface of particles in the soil was needed to be avoided. The previously developed pre-treatment for *E. hortensis* was optimal for *L. terrestris* too, according to the observations (Budán, 2013a; Budán, 2013b).

L. terrestris earthworms were kept in separate boxes and the volume of their Ringer solution was 3 ml/gram of earthworms. Animals were treated with 0.5 mmol Cadmium chloride (Sigma Aldrich) added into their Ringer solution and were kept alone for 48 hours (Budán, 2013a; Budán, 2013b).

3.2. Multimodal in vivo imaging

3.2.1. X-ray CT

3.2.1.1. Imaging of caudal vertebrae

The female Wistar rats (n=5) were scanned 3 and 8 weeks after surgery using a quantitative multiplexed multipinhole NanoSPECT/CT+ (Mediso, Hungary). The acquisition time was 30 min for X-ray CT. The reconstructed cubic voxel side size was 150 µm in a 198 × 198 × 546 pixel matrix. Fusion (Mediso Ltd., Hungary) and VivoQuant (inviCRO LLC, US) image analysis softwares were used to further analyze the reconstructed, reoriented and co-registered images by drawing appropriate VOIs over the specific caudal vertebrae (C4, C5) (**Fig. 1**).

The summarized absorbance of VOI was calculated. Voxels in VOI with attenuation below 1400 HU were cut off in order to filter the soft tissue from total X-ray attenuation of interest vertebra. Thus, only the mineralized bone tissue of C5 and C4 vertebrae were evaluated. This attenuation values were normalized in the following manner. The ratio of summarized bone mineral density (attenuation) of treated and control vertebra was calculated representing normalized bone mineral density (in this context is referred to as opacity).

From each group, 1 experimental animal with signs of inflammation was removed.

3.2.1.2. Imaging of the chest

About the chests of Balb/CBYJ female mice X-ray CT information was collected using a NanoX-CT (Mediso Ltd, Hungary) cone-beam in vivo micro-X-ray imaging system (8 W power of tube, 55 kV source voltage, 3.6 build in zoom) without using CT contrast agent. Reconstruction algorithm (Mediso Ltd.) used Feldkamp-filtered back projection was running on a 64 bit GPU. The reconstructed voxel sizes were 54 micrometers in 370 × 370 × 370 voxel matrix as ROI after our image acquisition.

As a first step our algorithm segmented the obtained 3D CT volume reconstructions to contain only the whole lung volumes and to discriminate automatically between lung tissue and bones of the chest and other tissues. Calibration of each CT image for HU scaling was performed using empty airspace within the field of view and a water-filled tube included in each scan. Linear attenuation data were reconstructed into pseudo Hounsfield units (HU) as cone beam CT cannot perform conversion of real attenuation data into Hounsfield units caused by Cone-beam specific technical reasons outside the scope of our paper. For sake of completeness we need to mention that cone-beam CT specific technical reasons, outside the scope of our paper, may distort the direct comparison of attenuation values of the same targets measured with other CT techniques but that simplicity in our subsequent text HU is used for pseudo Hounsfield units (Szigeti, 2016).

3.2.2. SPECT with 99mTc-Methyl diphosphonate tracer

The female Wistar rats (n=5) were scanned 3 and 8 weeks after surgery using a quantitative multiplexed multipinhole NanoSPECT/CT+ (Mediso, Hungary). The reconstructed cubic voxel side size was 150 µm in a 198 × 198 × 546 pixel matrix. Fusion (Mediso Ltd., Hungary) and VivoQuant (inviCRO LLC, US) image analysis softwares were used to further analyze the reconstructed, reoriented and co-registered images by drawing appropriate VOIs over the specific caudal (C4, C5) vertebrae (**Fig. 4**).

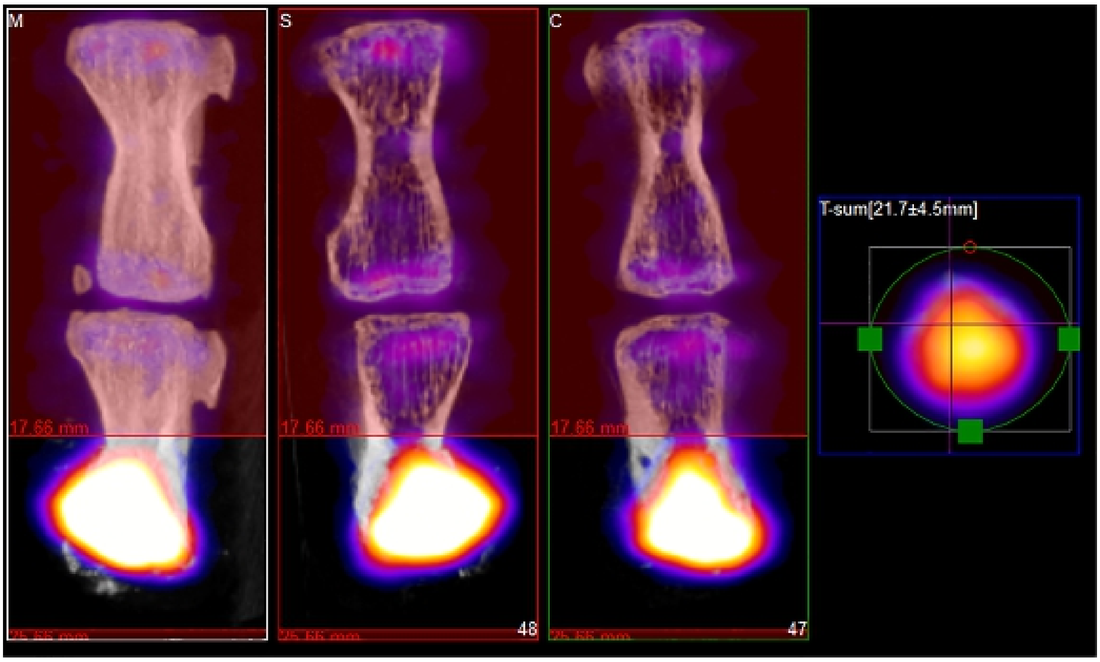

Fig. 4. Tc-99m-MDP activity in caudal vertebrae of treated rats after eight weeks. The C5 vertebrae (down) were treated and filled with a bone graft which was selected as VOI in SPECT at eight weeks after surgery. The color intensity shows the activity of Tc-99m-MDP in the last region of vertebra. The upper bones are C4 control vertebrae.

From the whole SPECT image, the C5 and C4 vertebrae of tail was selected then VOIs were marked (**Fig. 4**). The isotope activity in VOI was summed. Radioactive dose concentration of 99mTc-MDP was determined by dividing measured radioactivity in an animal (in MBq) by the whole body weight (in grams) of the animal to calculate the SUV, see above (Aberg, 2011).

From each group, 1 experimental animal with signs of inflammation was removed, as mentioned above.

The same, aforementioned quantitative multiplexed multipinhole NanoSPECT/CT+ (Mediso, Hungary) was utilized for selected rats (n=4) to carry out

SPECT examination 3 and 8 weeks after surgery. The rats were scanned 3 h after the injection of 80 MBq 99mTc-MDP. After acquisition, the data were reconstructed with the HiSPECT software.

This results were normalized in the same way as mentioned before. Thus, SUV ratios were used to measure the treatment response less depended on noise and image resolution. Normalized SUV values in this context is referred to as 99mTc-MDP activity. These process was performed on each animal. The mean and SD values of 99mTc-MDP activity in specific PMMA and HLBC groups were calculated in both of the examined time periods.

3.2.3. In vivo MRI of earthworms

For MRI a commercial small-animal sequential PET/MRI imaging system (nanoScan® PET/MRI, Mediso Ltd., Hungary) was used applying 1 T permanent magnet, 60 mm diameter transmit/receive volume coil and 450 mT/m gradients. A T1 weighted spoiled gradient echo sequence was applied with 3 dimensional acquisition scheme (7 x 7 cm^2 field of view in the coronal plane, 0.35 mm isovoxel size, 94 slices, repetition time of 20 ms, echo time of 2.3 ms, dwell time of 20 μs, flip angle of 25° and 4 averages). To achieve the needed short TE asymmetric echoes were acquired by sampling only the last 75% of the full k-space line. This sequence was selected in order to satisfy two main criteria: Firstly to minimize MRI acquisition time and secondly to achieve a good signal-to noise ratio. Due to the elongated shape of the earthworms one can make the scan even shorter with a rectangular-shaped FOV, when the number of phase encoding steps is reduced without increasing the voxel size. Our scanner is not capable of this and we decided to image more earthworms simultaneously to reach high throughput, increased MR signal and make the most out of a single FOV. Our above mentioned imaging box - made from a Falcon tube -is suitable for the scanning of 3 to 6 earthworms at the same time. Two separated levels of beds could be fitted into the Falcon tube and on each level 3 - 3 earthworms can be placed. Three of them are right next to each other and the three others are just above them on the appropriate level of the bed. With this positioning coronal slices (frequency encoding is parallel to the axes of the earthworms) are the most appropriate choice and slice number is set to cover all of the earthworms (Budán, 2014b).

3.2.4. In vivo PET with 18F- fluor-dezoxy-glucose tracer of earthworms

To detect glucose metabolism intracoelomic (ic.) injection of cca. 3 MBq of FDG in approximately 50 microliter Ringer was administered into the lower part (below the *clitellum*) of 4 animals (n=4) in each group. The whole body of earthworms were recorded utilizing nanoScan PET/MRI (Mediso, Hungary). The scanning was started immediately after FDG injection.

Data were acquired in list mode PET with acquisition time of 60 minutes and coincidence time window of 10 ns with energy window: 400-600 keV.

For reconstruction 3D OSEM was used with a voxel size of 0.3 mm and iteration of 6. Maximum intensity projection (MIP) and last output reference (LOR) filter was used. The whole imaging lasted for 160 minutes and 16 slices were reconstructed, each representing 10-10 minutes after the administration of tracer.

3.3. Data analysis and radiomics evaluation

3.3.1.Analysis of bone graft model

3.3.1.1. Data analysis of bone graft model

These calculations were performed for all female Wistar rats both 3 and 8 weeks after bone graft insertion as well and the statistical mean and SD were calculated.

The ratios of mean parameters at three and at eight weeks after bone graft insertion were determined. The means of opacity change were expressed in percent of opacity increasing from third to the eight week. The mean of Tc-99m-MDP activity change were calculated for both groups utilizing the mentioned ratios between the parameters of three and of eight weeks after bone graft insertion and expressed in percent of activity decreasing from third week to the eight week.

3.3.1.2. Radiomics-based evaluation of bone graft model

Linear regression analysis was carried out to examine the correlation between opacity change and Tc-99m-MDP activity change.

3.3.2. Analysis of mice lung model

3.3.2.1. Data analysis of mice lung model

The voxel densities were represented in a histogram using Freedman-Diaconis rule (Freedman, 1981; Jobse, 2012; Jing, 2003; Smith, 1996). Certain attenuation data of such segmented voxels of individual mice were imaged (-700 – -400 HU) **(Fig. 2.E)**, **(**-100 – +200 HU) **(Fig. 2.F)**, **(**+200 – +500 HU) **(Fig. 2.G)**, (+500 – +800 HU) **(Fig. 2.H)**, and (+1400 – +3800 HU) **(Fig. 2.I)** to underpin or disprove our hypothesis. In a further step of evaluation Gaussian curves was fitted by least square algorithm (Gnuplot 4.4) on these frequency distributions functions. The main parameters of Gaussian curve such as height, width and position were calculated. We also calculated the means and standard deviations (SD) of positions and widths of the Gaussian curves as well on the data of all examined groups **(Fig. 5.)**. The height is not presented on **Fig. 5.** as this parameter depends on width and area under histogram by definition.

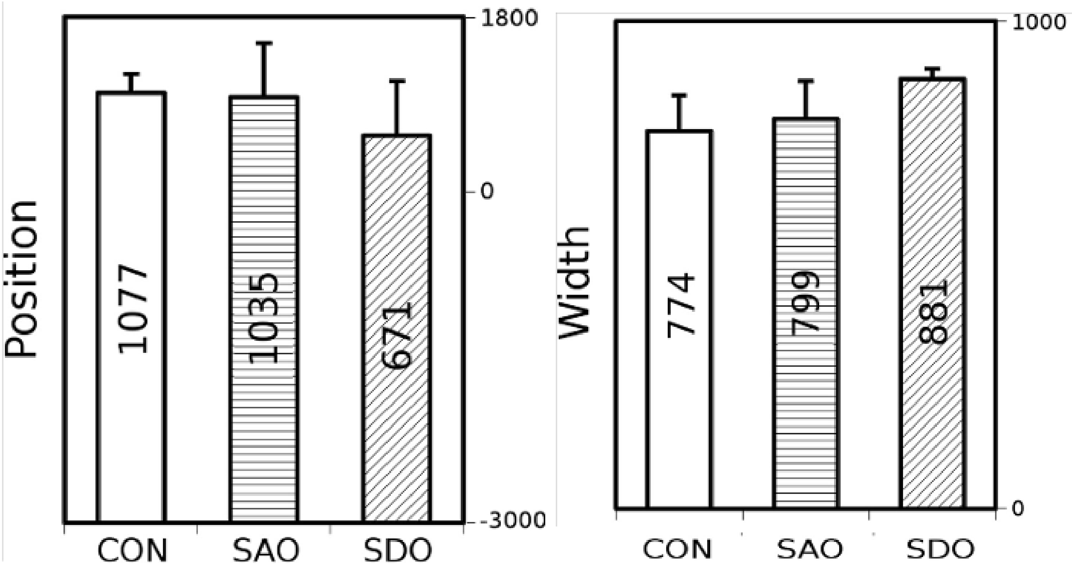

Fig. 5. Width and position parameters (mean, SD) of attenuation histograms of CON, SAO, SDO groups.

3.3.2.2. Radiomics-based evaluation of mice lung model

The method of final data analysis was performed using five main steps (**Fig. 6.**). Here we represent the exact details of the mentioned "five main steps method" of data analysis with the purpose to demonstrate how the cut-off range (COR) associated FD data were gained and FD – COR mathematical functions (FCF) were calculated (**Fig. 6.**).

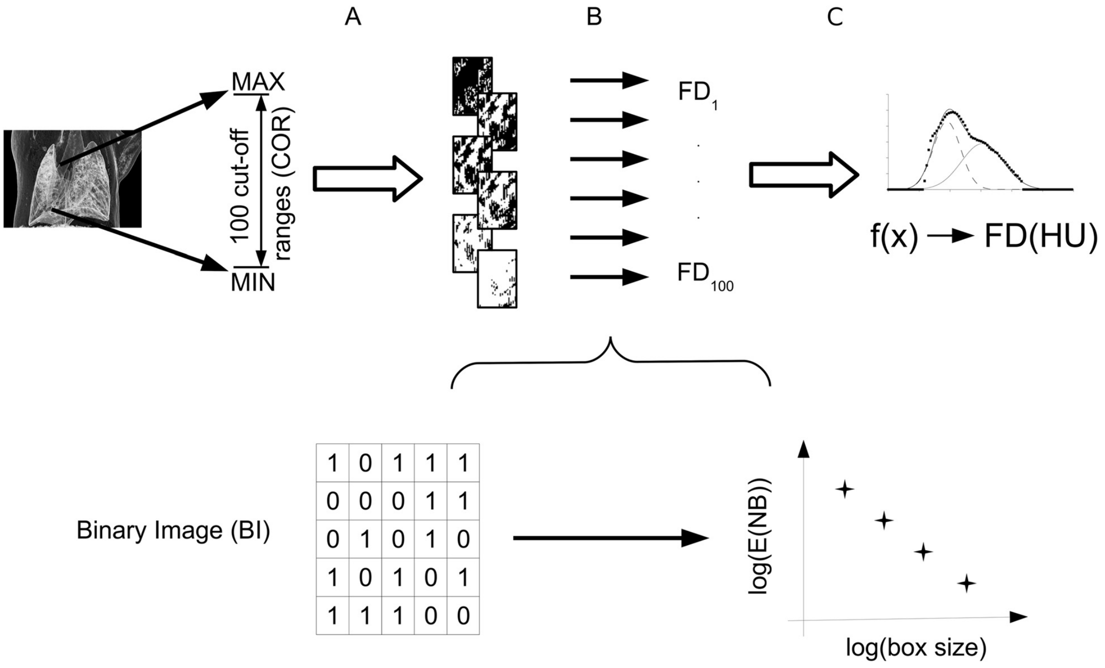

1	0	1	1	1
0	0	0	1	1
0	1	0	1	0
1	0	1	0	1
1	1	1	0	0

Fig. 6. Representation of the five steps of data analysis. **A**: The entire attenuation range of the reconstructed chest area of animals was divided into 100 distinct cut-off ranges **(Step 1)**. **B**: Binary images are generated **(Step 2 and 3)** and each such derived binary pattern was next associated with a calculated fractal dimension via box-counting algorithms **(Step 4)**. **C**: The FCF plot (**Step 5**).

Step 1. The whole attenuation range in the experiments was between -3,000 and +10,000 HU. The 100 distinct ranges of attenuations values were chosen by Freedman-Diaconis rule (Freedman, 1981). A chosen range is defined mathematically as the so called COR. So a certain attenuation value that was between the chosen higher and lower value were ranked into one COR. The 100

CORs involve the whole scale of the attenuations, and one COR contained 130 HU.

Step 2. The images of the tissues that were examined were partitioned into voxels (size: 54 micrometers in 370 × 370 × 370 voxel matrix) When the attenuation value of a given voxel was inside a certain COR then that voxel was associated to “1” otherwise to “0”. The voxel values out of the chosen range were assigned as “0” and these voxel were stated as background.

Step 3. This association step was repeated which results a pattern of voxels with “1” and “0” for every COR. These patterns of any CORs, as binary images (BI) were used in next steps. The 100 BIs were derived from 100 previously defined CORs (**Fig. 6. A**).

Step 4. The box-counting algorithm (Freedman, 1981; Smith, 1996) was used to calculate the FD number associated to each BI. See further details above in the **a)-d) substeps**.

Substep a) In this so called box-fitting least squares (BLS algorithm) the length of cubic boxes varied from 1 to 100 voxels. A given box size was chosen and that sized box was shifted without overlapping from one voxel to another voxel in every possible position in a certain BI. In each shifted positions – of the same sized box and assigned by the same COR - the number of boxes that contained at least one voxel with value “1”. was summarized. Thereby a number was gained the so called number of boxes of a given side length (NB).

substep b) The previous substep (a.)) was repeated with the difference that the boxes overlapped each other in each distinct spatial variations. Thus several slightly different NB results were produced, each of them derived from the new shifted overlapped positions. Therefore a certain box size and certain BI produced several NBs, depending from the exact shifted positions. From this slightly distinct results of NB’s average (E(NB)) were calculated, and that value was used for further evaluation.

substep c.) For each sized boxes the 4.a.)-b.) substeps were repeated. The E(NB) are represented in the function of the box size (**Fig. 6.B**) in a certain BI.

substep d.) To determine FD this function (**Fig. 6.B**) was fitted by a power function. The slope of fitted lines is the FD. To each certain BI (calculated by this method) an FD number was ordered (**Fig. 6.B1 and B2**).

Step 5. In this step the CORs were associated with one calculated FD (**Fig. 6.C**). At both very high and very low COR values the FD number is zero, while near to the middle values of the COR the associated FD number becomes nearly maximal.

Thus, the change of lung morphology was quantified by the FD – COR mathematical function (FCF) of each given 3D attenuation map.

The resulting function of FCF curves were thereafter separated into two Gaussian curves (presented as Gaussian curve A” and “B”). The Gaussian curves were fitted by using the BLS algorithm. As a final output of our algorithm the height, width and position parameters of these fitted “A” and “B” Gaussian curves were calculated for all animals. The lungs of all three groups – SDO, SAO and CON – were characterized by these parameters representing an association between the airway branching heterogeneity pattern and lung tissue attenuation heterogeneity **(Fig. 7.)** using least square algorithm (Gnuplot 4.4).

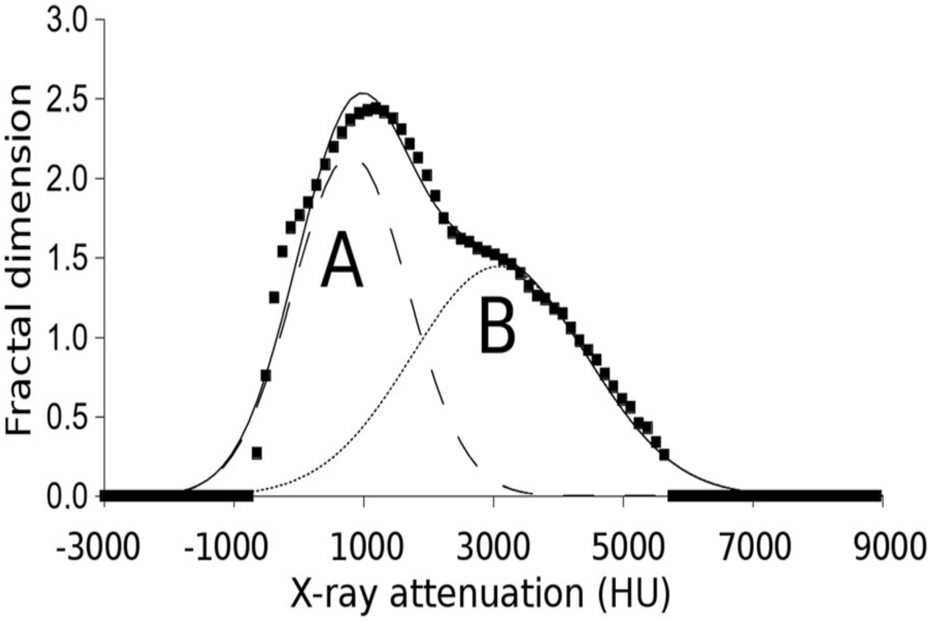

Fig. 7. The FCF fitted by Gaussian curves "A" and "B"

As a final output of our algorithm the height, width and position parameters of these fitted "A" and "B" Gaussian curves were calculated for all animals. To further attempt significant discrimination of the groups, ratios of all three mean parameters derived from both "A" and "B" Gaussian curves were calculated. The C insets are the ratios of "A" divided by "B" value (for example „C value" is calculated by height of "A" divided by height of "B", etc.) in a given group.

These steps were repeated to evaluate the images of each animal.

3.3.3.1. Data analysis of soil pollution model

To evaluate the pre-treatment the results of group A and B were compared to each other. Other relevant observations were recorded at occurrence. For example, the potential earth content in their intestines were checked visually (earthworms were put before a light source and thus their intestines become transparent).

The FDG uptake value ratio was calculated in both groups and expressed in percent from fourteenth time interval's FDG uptake value to the FDG uptake values of the first time interval.

3.3.4. Statistical analysis

3.3.4.1. Statistical analysis for in vivo imaging of bone formation model

2-tailed Student's t-test were performed for statistical evaluation of mean and SD values of bone opacity as well as Tc-99m-MDP activity in both of the examined time periods.

3.3.4.2. Statistical analysis for in vivo imaging of air pollution model

Statistical analysis (STATISTICA 7.0, Statsoft Inc., USA) was performed using the nonparametric Kruskal-Wallis (KW) test for fitted parameters of groups due to the small number of animals. Differences between all groups were evaluated by the Mann-Whitney post hoc (MWph) test (**Fig. 5.**).

Chi-square test was used to test the reliability ($p<0.05$) of fit histogram and FCF of both one fitted single and the resulting fitted two independent Gaussian curves, respectively. Statistical analysis (STATISTICA 7.0, Statsoft Inc., USA) was performed using the nonparametric Kruskal-Wallis (KW) test for fitted parameters of groups due to the small number of animals. Differences between all groups were evaluated by the Mann-Whitney post hoc (MWph) test **(Fig. 7.)**.

3.3.4.3. Statistical analysis of earthworm model

3.3.4.3.1. Statistical analysis of pre-treatment for in vivo imaging of earthworm model

Mann-Whitney U test was used to compare the data between earthworm group A and group B. All tests were performed using the Statistical Package for Social Sciences (IBM SPSS Statistics 20.0 software; IBM Corporation; Armonk; NY; USA).

3.3.4.3.2. Statistical analysis of earthworm model using PET with 18F- fluor-dezoxy-glucose tracer

2-tailed Student's t-test was performed for statistical evaluation of mean and SD values of FDG uptake ratios.

4. RESULTS

4.1. Examined descriptive parameters of bone grafts

With exception to one rat from each group, autopsy did not reveal any pathological condition including inflammation. In both groups the excluded rats autopsy disclosed inflammation.

4.1.1. Bone opacity imaged with X-ray CT

The mean opacity increased, while the mean 99mTc-MDP activity decreased, in both of the groups and at both time points that are at 3 and 8 weeks following treatment.

The difference between the PMMA and HLBC opacity values at the third and the eighth weeks were not significant (n=4, p=0.378) and (n=4, p=0.591), respectively (**Fig. 8.A** and **B**).

4.1.2. 99mTc-Methyl diphosphonate activity imaged with SPECT

The difference between PMMA and HLBC 99mTc-MDP activity values at the third week were also not significant (n=4, p=0.651) (**Fig. 8.C**). Likewise, these differences at the eighth week (n=4, p=0.807) were also not significant (**Fig. 8.D**).

Only in the HLBC group, the activity of the mean of 99mTc-MDP decreased significantly (n=4, p=0.002) starting from the third week until the eighth week (**Fig. 8.C** and **D**).

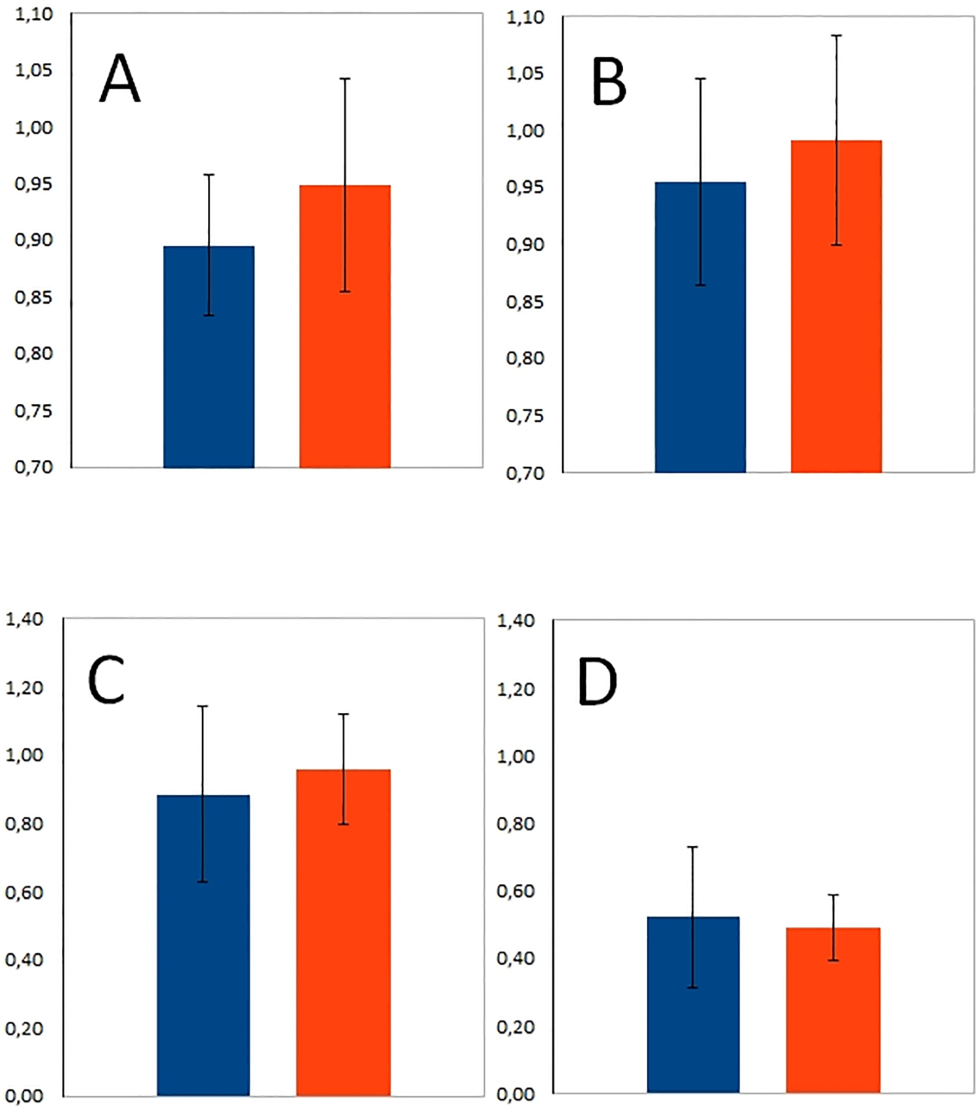

Fig. 8. Mean opacity and mean Tc-99m-MDP activity. The figure represents the mean opacity (above) and the mean Tc-99m-MDP activity (below) of PMMA (blue) and HLBC (orange) at third weeks (A, C) and at eight weeks after surgery (B, D).

4.1.3. Time related changes of parameters

The mean opacity change in PMMA group compared to the same parameter of HLBC group was not significantly different (n=4, p=0.395) (**Fig. 9.**). Similarly, the mean activity change of 99mTc-MDP in PMMA and HLBC groups was not significant (n=4, p=0.468) (**Fig. 9.**).

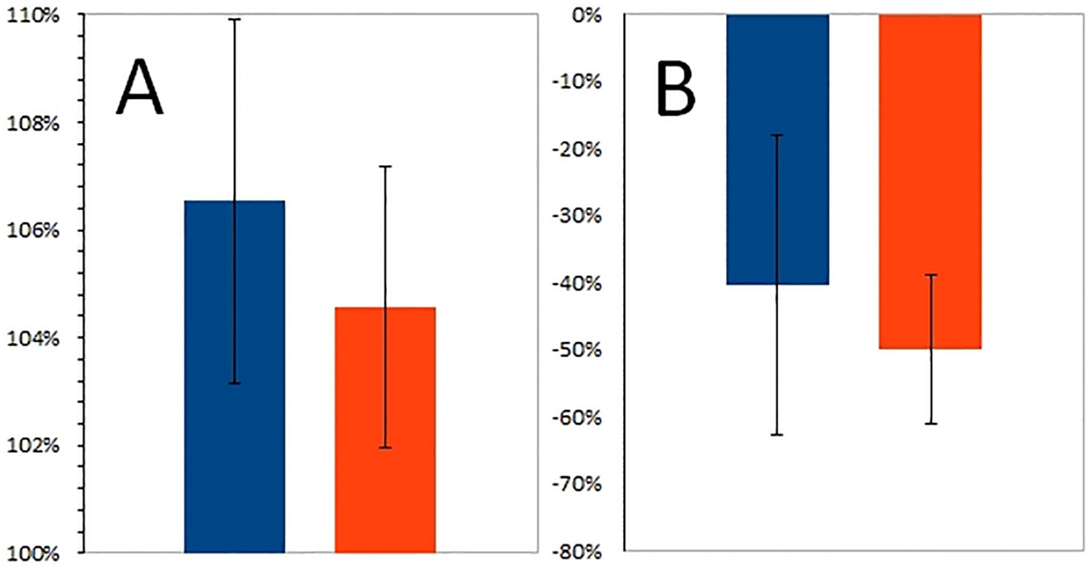

Fig. 9. Change ratio % from third week to eighth week after surgery of mean opacity increase (A) and mean Tc-99m-MDP activity decrease % (B) for PMMA (blue) and HLBC (orange) groups.

4.1.4. Multimodal data analysis utilizing radiomics evaluation

Performing linear regression analysis, strong significant positive correlation was found in HLBC group comparing the increase of bone opacity and decrease of 99mTc-MDP activity variables (r=0.772, p=0.012) (**Fig. 10.**).

Whereas, in case of PMMA treated group, medium negative correlation was found between these two variables (r=0.395, p=0.605) (**Fig. 10.**).

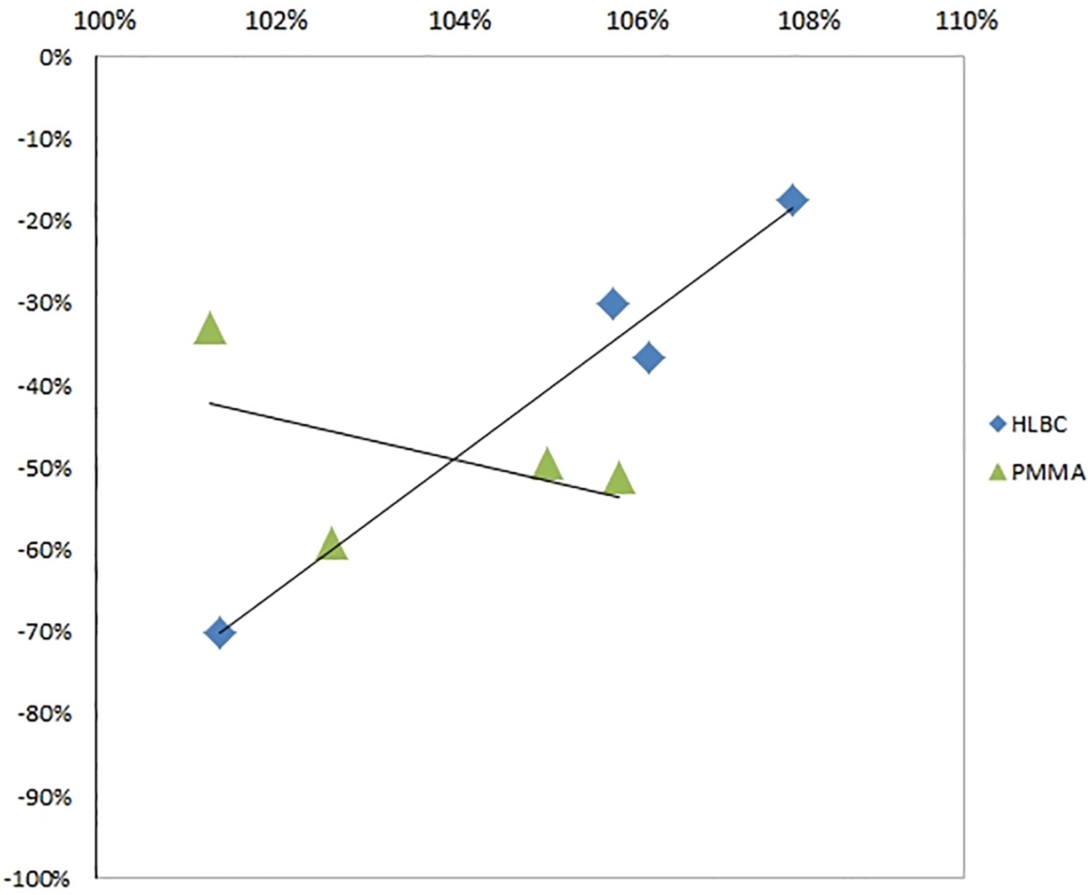

Fig. 10. The ratio of opacity increasing % and the ratio of Tc-99m-MDP activity decreasing % from 3rd week after surgery to 8th week after surgery values for each individual animal in PMMA (triangle) and HLBC (diamond) groups were determined. A linear regression analysis was carried out.

4.2. Observations and examined descriptive parameters of lungs

4.2.1. Observations based upon the X-ray CT of chest

According to the selection of voxels as ROIs inside the chest with certain HUs the followings were found: lung parenchyma (**Fig. 2.E**), pleura, endothoracic fascia, some intercostal muscles and epipleural fat, interlobar fissures (**Fig. 2.F**), respiratory- and heart muscles, diaphragm, lung tissues (**Fig. 2.G**), blood inside the vessel, aorta and heart, lymphatic fluid and interlobar fissures other tissues **(Fig. 2.H)**, and bones **(Fig. 2.I)** (Prokop, 2003; van Rikxoort, 2013). Slightly differences of tissue attenuations were observed visually based on region of the lungs (**Fig. 2.D)**.

4.2.2. Examined descriptive parameters of lungs

4.2.2.1. Frequency distributions of attenuation data (height, width and position parameters of Gaussian curve)

The voxel density histograms show no significant differences between the mean values of width of three groups (**Fig. 5.**).

4.2.2.2. Cut-off ranges (COR) of attenuation associated with calculated fractal dimension (FD)

The FCF could be evaluated very well by separating it to two components (**Fig. 7.**). Both of these Gaussian curves ("A" and "B") could be characterized by height, maximum position and width of the peak.

The mean of height of "B" curve of SDO group increased significantly when compared to the CON group (KW p=0.002, MWph p=0.036) and to the SAO group (KW p=0.002, MWph p=0.024), but not significantly when the CON was compared to the SAO group (**Fig. 11.B top)**. The mean of widths of "B" curves of the SDO group increased significantly (KW p=0.016, MWph p=0.036) compared to the CON group, and also significantly when compared to SAO group (KW p=0.016, MWph p=0.024) but not significantly when the CON group was compared to the SAO group (KW p=0.016, MWph p=0.429) (**Fig. 11.B middle**). The means of different maximum positions are not changed significantly between SDO, SAO and CON groups (**Fig. 11.B bottom**).

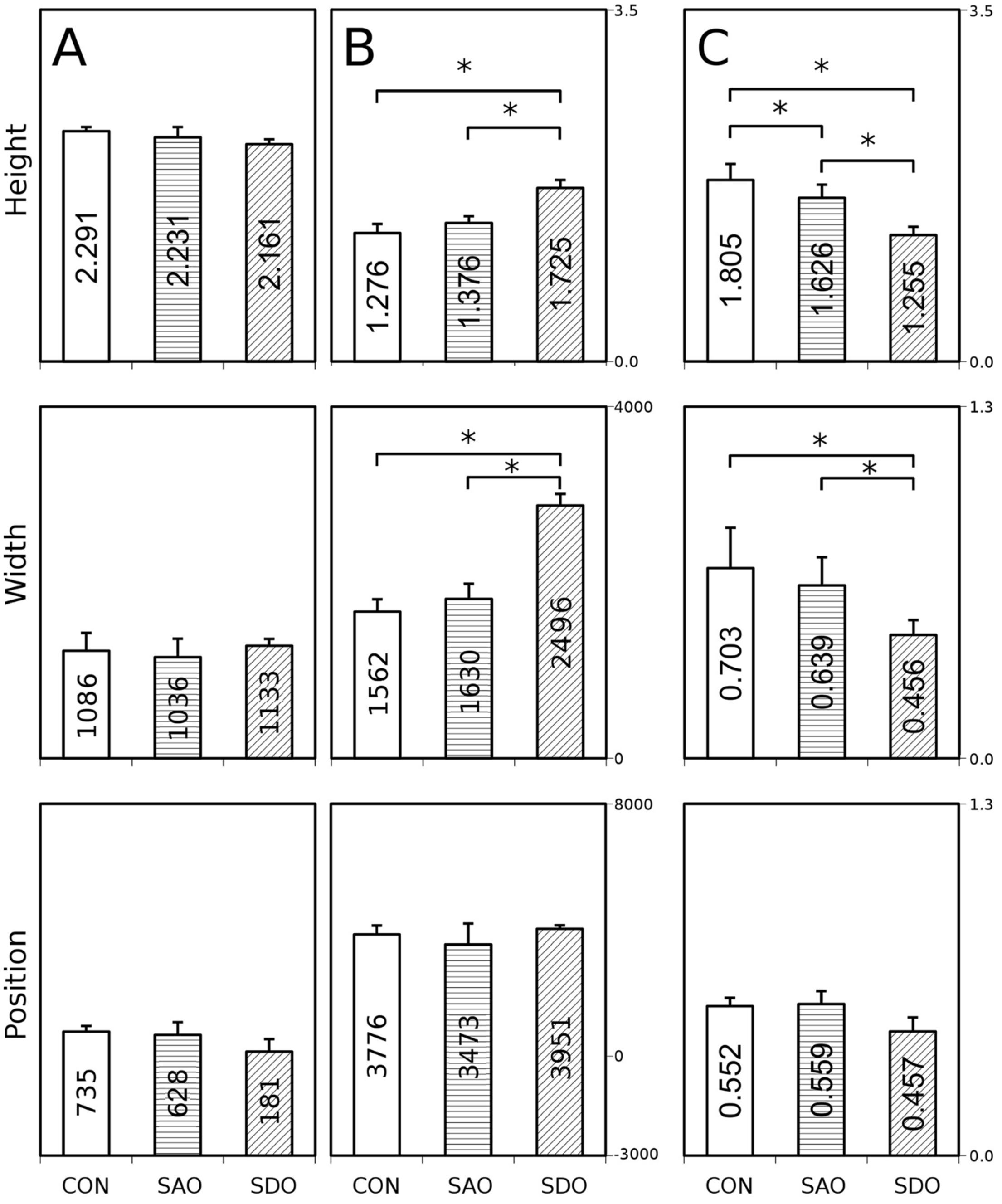

Fig. 11. Calculated height, width and position parameters of the FCF. **A.**: Height, width and position parameters of Gaussian curve „A” (CON, SDO, SAO groups). **B.**: Height, width and position parameters of Gaussian curve „B” (CON, SDO, SAO groups). **C.**: The ratios of the relevant parameters of Gaussian curves „A” and „B” (CON, SDO, SAO groups). $*p < 0.05$, Kruskal-Wallis (KW) test with Mann–Whitney post hoc (MWph) test.

4.2.2.3. FD – COR mathematical function's descriptor parameters analyzed

The visible difference between the ratios of height is significant in SDO group compared to the CON group (KW p=0.005, MWph p=0.0357) and the SDO group compared to the SAO group (KW p=0.005, MWph p=0.024) and in SAO group compared to the CON group (KW p=0.005, MWph p=0.042) as well (**Fig. 11.C. top**).

The ratio of width of SDO and CON groups (KW p=0.021, MWph p=0.036) and SDO and SAO groups (KW p=0.021, MWph p=0.024) show a slight but significant difference (**Fig. 11.C. middle)** but the difference between SAO and CON groups is not significant.

4.3. Examined parameters of earthworms

4.3.1. Parameters of pre-treatment for optimal earthworm immobilization

All *E. hortensis* earthworms' body masses decreased significantly from the beginning of the experiment until the first day. We also observed that in their body weight and the quantity of excrements decreased significantly in the first day and then only slightly thereafter (**Fig. 3.A.** and **B.**). At the third day of the experiment their gastrointestinal tract was considered clean from excrements according to our visual observation. The body masses of *Eisenia h.* were 1.1± 0.3g in the beginning of the experiment evaluating the pre-treatment.

In both of A and B groups the mass of earthworms decreased (Mann-Whitney, $p<0.05$) from the beginning of the experiment to test the pre-treatment until the first day. In group A none of the earthworms showed significant physiological and morphological alterations and their body mass remained near to the body mass measured on the first day until the third day (Mann-Whitney, $p>0.05$). The body mass of earthworms in group B changed variously and generally strongly. At the fourth day an increase in body mass was found because their body had begun to swell due to the Ringer solution (Mann-Whitney, $p<0.01$). All of the earthworms in group A moved under the polystyrene plates each time when they were checked.

According to observations and data about body mass increasing as well (**Fig. 3.B.**) in group B some of the earthworm's body begun to swell even at the first day. At the fourth day all of the earthworms were swollen in such a manner that they were considered not to be useful for our planned MRI examination. At the fourth day five from the ten earthworms were swollen significantly and one of them was dead. The body mass of the earthworms corresponds to this observation.

In the group A the change of the body mass as function of the time and the survival data were significantly better than in the control group B (Student's t-test, p=0.04) (**Fig. 3.A.** and **B.**). To keep the earthworms until the third day in Ringer solution with polystyrene plates in their boxes seemed to be optimal preparation for further experiments.

In summary a 3 days long preparation time with the application of polystyrene plates was found optimal. Thus both the experiments to immobilize earthworms and to examine morphology of the organs with MRI were carried out in earthworms pre-treated in the way as described before.

4.3.2. Application of alcohols for immobilization

After 30–60 min spent in propan-2-ol immersion, animals' muscles were completely relaxed. Thus they were immobilized for the duration of the experiments. The use of the airtight box was convenient for better handling of earthworms and avoiding gas exchange, it also kept the airspace in a steady state concentration the alcoholic vapor.

Ethanol and propan-2-ol treatment caused 5 min long immobilization in the aforementioned doses after the earthworm came into contact with fresh air.

However alcohols seemed to be useful, promising and effective method to immobilize earthworms for more than 3 h if the body surface contact with the alcohol solution was maintained. On the other hand, fluids may disturb MR imaging modalities and greatly impair the result. This was avoided by the airtight box and bed, because of the bed kept the earthworm's body over the alcoholic immobilization fluid's level, but the vapor of alcohol was in contact with the earthworms. The special bed avoided shifting of the anesthetized animals inside the box and enabled movement of the experimental specimens properly to the MRI modality as well. Indeed during the scan earthworms were not moving. Repeat exposure of the alcohol anesthesia induced a slight tolerance which was overcome by increasing the dose of alcohol.

For the sake of completeness we need to mention, that with a slightly overdose of propan-2-ol the hearts can be „switched off”. Thereby blood streaming ceases and consequently the whole body of earthworms lose their tone. Moreover, after the propan-2-ol treatment has ceased and the propan-2-ol is excreted from the earthworms (predominantly through the skin, in a few hours) then earthworm’s hearts restarted pumping - and the animals became reanimated.

4.3.3. MRI observations of immobilized earthworms

Using MRI both in *E. hortensis* and *L. terrestris* the whole intestinal tract and the corresponding special calciferous gland (gland of Morren) is visible at the 11-12th segment, as „black point”, an organ abundant of calcium. Reproductive organs are visualized, as well (**Fig. 12.**).

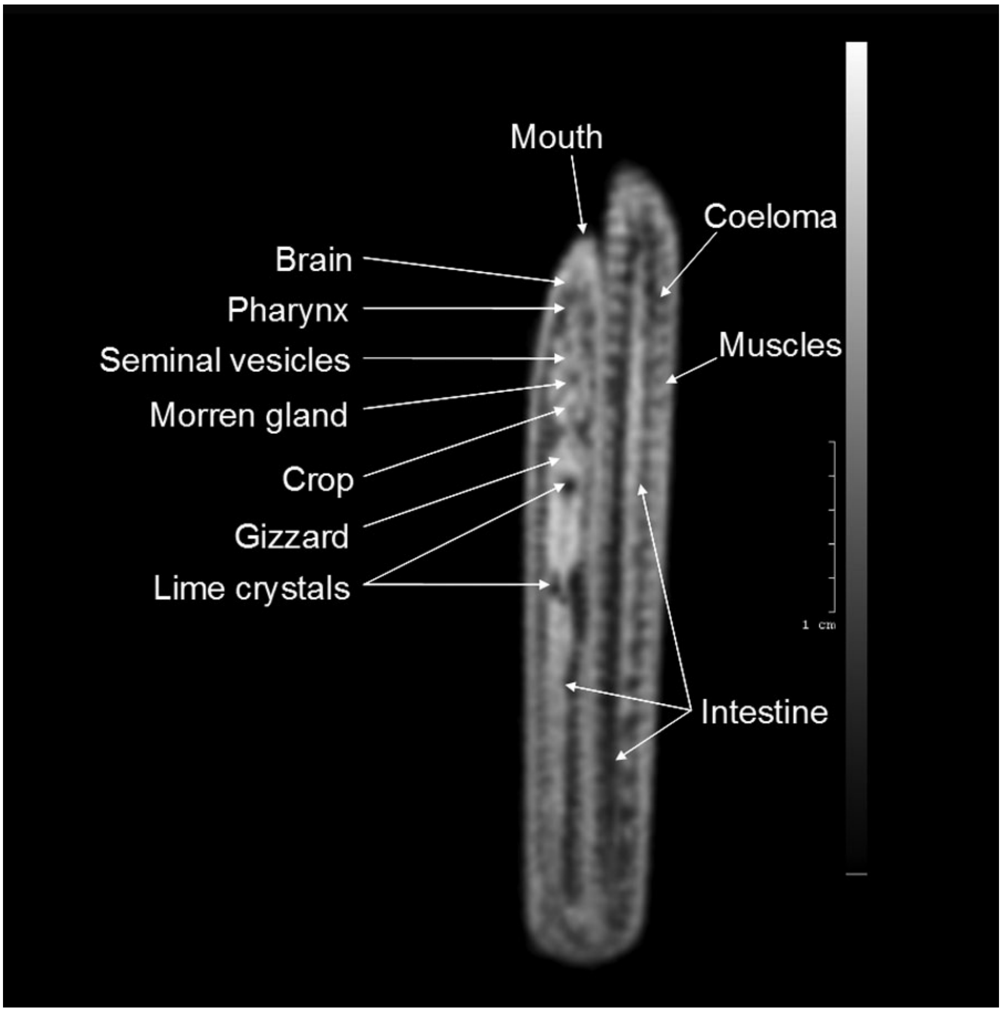

Fig. 12. Organs of earthworm (*E. hortensis*) are visualized by nanoScan PET/MRI (Mediso Ltd, Hungary). T1 weighted spoiled gradient echo sequence, 3 dimensional acquisition scheme.

In *L. terrestris* with MRI, besides the kidneys (*nephridia*), also the gut, the hearts, and the brain could be visualized, but assign of ROI seemed not to be reliable (data not shown) (Budán 2013a; Budán 2013b).

4.3.4. FDG uptake of earthworms

FDG uptake of earthworm (*L. terrestris*) between 150 and 160 minutes after injection enabled the visualization of the brain, the hearts, the kidneys (*nephridia*), the gastrointestinal tract and the seminal vesicles. However, despite that the uptake in those organs could be visualized, the quantitative evaluation was hindered by the poor resolution of PET and the still relative small size of earthworms (**Fig. 13.**).

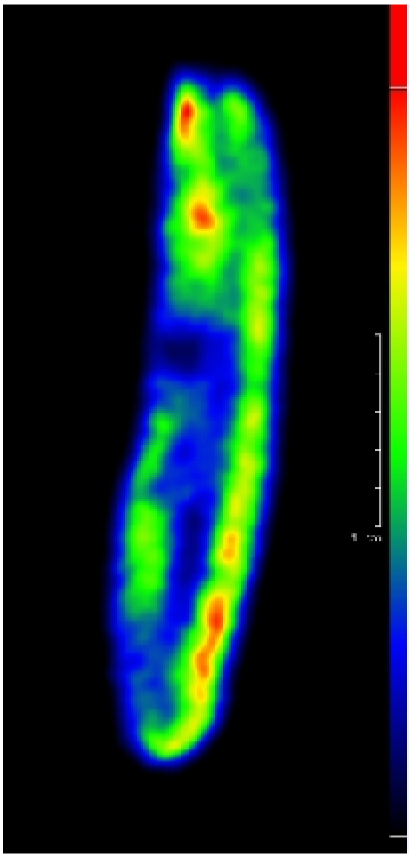

Fig.13. FDG uptake of earthworm (*L. terrestris*) between 150 and 160 minutes after injection. The brain, the hearts, the kidneys, the gastrointestinal tract and the seminal vesicles were visualized.

The ratio of mean last and mean first interval time's FDG uptake % of the frontal part of earthworms in the Cd exposed group were (n=4) 113.49 % and in the control group (n=4) 146.64 % (**Fig. 14.**).

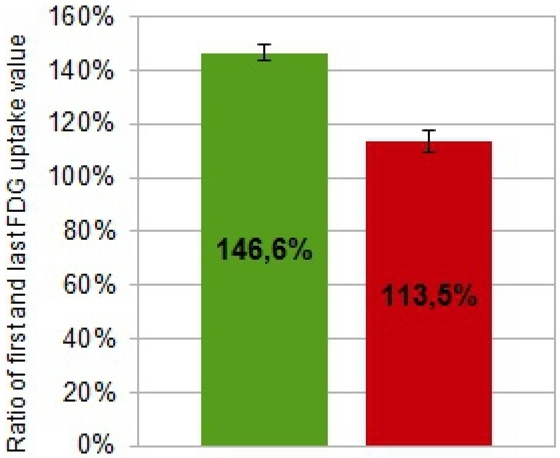

Fig. 14. Ratio of means of first and last interval time's FDG uptake % of the frontal part of earthworms (*L. terrestris*). Control group (Green) and Cd exposed group (Red).

There was a significant difference between the Cd exposed and control groups (n=4, p=0.001) (**Fig. 14.**).

5. DISCUSSION

5.1. Imaging of bonegrafts enhanced bone healing

The specific circumstances and differences of experimental set-ups may influence slightly the results as discussed below.

Specific technical properties of utilized CT, as well as other factors, can influence the measurements, see above (Coles, 1995).

The Tc-99m MDP isotope activity is proportional to the population of osteoblast cells, which indicate actual rate of healing process. However, the osteoblast activity is a more important marker of actual in situ bone formation at the moment of measurement. The osteoblast activity and proliferation is controlled by molecular environment and micromorphology of trabecular bone structure. The role of filling material is to help the bone rebuilding and promote osteoblast activation. In vivo quantification with the NanoSPECT/CT is highly accurate, in precise determination of the absolute activity in a ROI over a broad range of activities was verified by earlier literature analysis (Forrer, 2006).

5.1.1. Inflammatory mechanisms affecting bonegrafts and bone formation

Crosstalk amongst inflammatory cells is essential to the formation and repair of bone (Loi, 2016). For example the polymorphonuclear leukocytes and cells of the monocyte-macrophage-osteoclast lineage, as well as mesenchymal stem cells from osteoblast lineage and vascular lineage are needed to crosstalk for proper bone healing (Loi, 2016). Pathologic conditions, such as neoplasticity, hormonal changes, inflammation, ischemia, remodeling may cause abnormal Tc-99m MDP uptake in soft-tissues, thereby, limiting the sensitivity of this method with false positive results (Peller, 1993). On the other hand, animals excluded from evaluation with signs of inflammation and lack of bone opacity increasing are also explained by the signal transduction mechanisms of bone healing. Activated macrophages express cytokines including interleukin-1 (IL-1), interleukin-6 (IL-6) and tumor necrosis factor alpha (TNFα), which mediate periprosthetic osteolysis too (Vaishya, 2013). Indeed, inflammatory factors could activate a layer of synovial like cells, which line the bone cement interface supported by a stroma containing macrophages, described in loose prostheses (Goldring, 1986). Increased bone resorption and suppressed bone formation have often dysregulated inflammatory signal transducers in the background (Loi, 2016). This could occur as the consequence of the *ab ovo* inflammatory mechanisms, induced by the surgical procedure. For example particulate debris derived from PMMA cement, is observed commonly in the membrane surrounding loose joint prostheses causing an inflammatory response and contributing to osteolysis and failure of the implant (Gelb, 1994).

In summary, bone grafts may enhance and also inhibit bone healing via inflammatory factors and mechanisms.

5.1.2. Potential distorting factors of bone formation model's in vivo imaging

The effective atomic number for PMMA is 6.48 and for the PMMA body phantom the beam-energy profile manifested in the CT numbers for 80 kVp, 100 kVp, 120 kVp, and 135 kVp as 110 HU, 123 HU, 133 HU, and 135 HU (Sookpeng, 2016). Thereby the results may depend slightly on specific beam-energy set-up of CT.

The reconstruction method can slightly affect the results too (Otsu, 1979). Thus direct comparison of different CT methods most likely may cause bias (Coles, 1995).

The 99mTc-MDP is administered intravenously and is delivered to the skeletal system based on vascular distribution. The degree of radiotracer uptake depends primarily on two factors: blood flow and, perhaps more importantly, the rate of new bone formation (Genant, 1974; Love, 2003). Moreover, both of the osteoblast activity and blood flow parameters, relevant in bone formation, are regulated by several factors, such as insulin-like growth factor (IGF I, II), fibroblast growth factor (FGF), TGF-β and platelet-derived growth factor (PDGF), etc. (Albrektsson, 2001).

Although neither the osteoblast-like cells, nor the collagen sponges accumulate 99mTc-MDP (Chopra, 2007), but the hydrophilic micro-sized surface features of matter promote differentiation of rat osteoblast-like cells into calvaria cells, which can be labelled by Tc-99m-MDP (Andersson, 2003). In addition, also the hydrophobic bone surfaces contribute to that slightly (Andersson, 2003).

5.1.3. Normalization and filtration in order to improve data evaluation

The mean opacity as well as Tc-99m-MDP uptake values of examined ROI can be normalized to the same parameter of an intact ROI of the same object, or specific ROI of experimental animal, respectively. This method also averts theoretically possible bias, caused by properties of experimental set-up (Coles, 1995) as well as independent environmental factors of bone grafts materials, such as temperature, mechanical stress, etc.

The adequate selection of X-ray attenuation "density" cut-offs ordered to filter-out the tissues (or objects), irrelevant from viewpoint of examinations is a widely used method (Gillies, 2016; Kumar, 2012; Szigeti, 2016).

However it can be utilized only if the specific attenuation ranges are well characterized and can be discerned from the examined tissues as well. Indeed, different substances and tissues have different radiodensities: -100 to -50 HU, muscle +10 to +40 and bone from +700 for cancellous bone to +3,000 for cortical bone (Feeman, 2010b). Thus the loss of data can be averted.

For example the bones in rat's rib cage have +1400 – +3800 HU attenuation value, depending on the ratio of bony and cartilaginous tissues (Szigeti, 2016). HLBC are considered to have similar attenuation values as cancellous bones (MacNeill, 1999). The attenuation value of PMMA was detailed earlier. The applied graft materials themselves in this experimental set-up cannot been imaged, because of their attenuation is below 1400 HU. In summary, we can state, that the filtration of attenuations below 1400 HU enables the proper imaging of mineralized bone tissues. Thus, only the result of bone mineralization process was followed up utilizing the in vivo X-ray CT imaging technique, in the examined time periods, respectively.

5.1.4. Examined bone grafts effect on bone formation

The mean opacity increase of examined voxels in both groups between 3 and 8 weeks after surgery indicates the progress of bone tissue mineralization. Bone formation process was enhanced either by PMMA or HLBC, respectively (**Fig. 8.A** and **B**). Most of the grafts generally provided template to guide the repairing tissue (Chen, 2016; Thoren, 1995). Thus, autonomic healing is achievable in PMMA bone cement brand (Lewis, 2009). It has to be noted that the difference between the mean opacity values of the two experimental groups was statistically not significant, despite the fact that normalization of C5 vertebrae to intact C4 vertebrae and filtration of HU values below 1400 HU measures were carried out (**Fig. 8.A** and **B**).

Still, the applied bone graft attributions may cause slightly increase of mean opacity of HLBC group when compared to PMME group (Aberg, 2011). Indeed, in MC3T3-E1 cell culture, PMMA particles impaired cell proliferation and inhibited *RUNX2*, *OSTERIX* and *DLX5* osteoprogenitor gene expression in a dose-dependent manner (Chiu, 2010).

HLBC enhanced bone formation earlier so as PMMA (Aberg, 2011). This was highlighted in specific Tc-99m-MDP uptake profil of both groups starting at the third week until eighth week after surgery. In PMMA group, Tc-99m-MDP uptake was slightly decreased, whereas, a strong decrease in HLBC group was obtained in a statistically significant manner (**Fig. 8.C** and **D**).

The increase of mean opacity ratio from third week to eighth week following surgery was stronger in PMMA group than in HLBC group (**Fig. 9.A**). However, in a previous publications it was indicated that PMMA enhanced bone formation is less exquisite and delayed when compared to HLBC's bone formation enhancement (Sheikh, 2017; Sheikh, 2013). Indeed, the low mean opacity value in PMMA group at third week after surgery was reflected in the mean opacity ratio (**Fig. 8.A** and **9.A**). This result constitute a spectacular example of advantages of multimodal imaging, since the aforementioned data are in concordance with Tc-99m-MDP uptake data. This uptake represents functional information that might highlight the features of bone formation process (**Fig. 9.B**).

Thus, the change in the ratio by itself could not be used as a reliable descriptive parameter for bone formation, especially with such a low sample number as was the case in this experiment. In this investigational set-up, Tc-99m-MDP uptake ratio was informative in regard to the osteoblast activity (Aberg, 2011) (**Fig. 9.B**).

Multimodal 99mTc-MDP NanoSPECT/CT imaging utilizing radiomics evaluation has elucidated the decreasing 99mTc-MDP uptake in relation to bone opacity change increase (**Fig. 8.** and **9.**). The results of linear regression analysis pointed out the spectacular discrepancy between the examined group trends. Variables of PMMA group showed negative, while HLBC group's revealed positive correlation (**Fig. 10.**).

Clearly, PMMA lacks both osteoinductive and osteoconductive mechanisms (Vaishya, 2013). Consequently, in PMMA group, osteoblast activity indicated healing process showed a medium negative correlation with bone density.

However, HLBC showed a strong positive significant correlation between increased opacity ratio and decreased Tc-99m MDP activity. Probably because revascularization of cancellous autografts take place earlier than the cortical grafts, (as early as the fifth day following implantation) due to their porous architecture (Sheikh, 2017; Sheikh, 2013). In addition, in HLBC group the creeping-substitution mechanism has enhanced vascularization and albumin-coated surface promoted osseointegration (Weszl, 2012; Aspenberg, 1990).

Aforementioned pathologic conditions cause abnormal Tc-99m MDP uptake in soft-tissues (Peller, 1993) but according to the results of autopsy they can be excluded in rats taking part in this experiment. Also results - in this experimental set-up - confute potential abnormal uptake of Tc-99m MDP by inflamed locations, because the HLBC group took up more Tc-99m MDP than PMMA group, but PMMA is known to possess slightly proinflammatory effect, as disadvantage – contrary to HLBC group (**Fig. 8.C** and **D**) (Li, 2013).

5.2. Imaging of air pollution induced alterations of the lungs

5.2.1. Attenuation of lung tissues based upon simple X-ray CT scans

In our experimental setup attenuation ranges using HU as basis of certain ROIs **(Fig. 2.E, F, G, H, I)** correspond to attenuation scale of relevant anatomical regions inside the chest (Prokop, 2003; van Rikxoort, 2013). Minor differences of spatial attenuation of lung tissue voxels are represented according to the upper region’s cartilage content, contrary to lower regions where cartilage is absent (**Fig. 2.D**).

5.2.2. Simple attenuation-frequency histogram-based parameters of lung tissues

According to the results of simple HU-frequency histogram-based parameters, such as positions and widths (**Fig. 5.**) in all of the examined animal groups assigned the calculated data can be neither the basis of detection nor the categorization of air pollution exposure. This classical evaluation method could not distinguish tissue alterations. The absence of gating or short period of observation could contribute to this, as well.

Contrary to small animal CT imaging the respiratory gating is not applied methods in the clinical practice. However the scanning time of new generation CT is decreased even below breath-hold time of some affected patients, but still this is a real problem (van Rikxoort, 2013). To perform it in certain patients (for example patients with decreased lung capacity due to COPD) is unpleasant if even possible, gating increases time of examination and consequently X-ray exposure, usually without gating relevant part of attenuation data is lost or not be able to interpret based on radiological point of view.

5.2.3. Fractal dimension cut-off range mathematical function histogram-based parameters of lung tissues

From FCF separated Gaussian curve „A” obtained in our method is probably mostly the quantitative summary of mean values of FD which are ordered to voxels **(Fig. 7.)** containing air in the lung parenchyma in 90 % airways (**Fig. 2.E)** (Prokop, 2003). Lower FD values presents air in less branching upper airways, while the higher FD values are most likely ordered to voxels containing air in more branching lower airways together with bronchiole, respectively (**Fig. 7.)** (Nagao, 2002). The Gaussian curve „B” is most likely the mean FD values of voxels of containing fluids the lung tissue (**Fig. 2.H, G)**, besides bones (**Fig. 2.I, Fig. 7.)**. Higher cut-off density of Gaussian curve „B” corresponds to the slightly increased attenuation of aforementioned higher airways with some cartilage content contrary to lower airways (and *per se* to alveoli, respectively) (**Fig. 2.D**). Mucus content (and the consequently formed air-bubbles) in of airways (**Fig. 2.F**) increase quantity of voxels in CORs to which the overlapping FD was ordered between the two Gaussian curves (**Fig. 7**).

Sulfurous gases are irritant and induce inflammation, bronchoconstriction and bronchitis that increase production of mucus (EPA 2014b; Bossé, 2010; Yamashiro, 2011). Significantly increased height of SDO group compared to the other two groups (**Fig. 11.B**) is explained by overproduction of mucus, which can form plugs that entrap air or temporally and partly obstructs even upper airways too (Williams, 2006). This is supposed to shift X-ray attenuation patterns to higher values too.

Airway clearance of mucus depends on the interactions between physical properties of the mucous gel, serous fluid content, and ciliary function, besides airflow (Kim, 1997). Wagner et al. found in Spargue-Dawley rat model that 80 ppm concentration of SO_2 (besides overproduction of mucus) caused epithelial cells to lose their ciliae (Wagner, U., 2006). Also number of voxels with fluid content may increase caused by inflammation of lung tissues (see below).

The increase of width parameter of SDO group (**Fig. 11.B**) refers to two process in the same time: the first, rising number of voxels representing tissues with thickening walls of the airways, caused by SO_2 exposure, that penetrates even in deeper airways (EPA 2014b) and induce inflammation in the alveoli leading to appearance of fluid, derived from necrotic cells (Williams, 2006) which increase attenuation (Castañer, 2005). Thereby increased number of voxels with higher COR values can be supposed due to the presence of fluid. Indeed, biomarkers of individual harms due to air pollution and even association of carcinogenesis are defined well (Demetriou, 2012).

The other process is the formation of mucus-plugs, as mentioned earlier, trapping air inside the alveoli and leading to further formation of micro-sized bubbles (Bossé, 2010; Moldoveanu, 2009) inside the lung parenchyma distorting normal FCF pattern increasing the number of voxels with lower HU (represented in our evaluation method with lower COR) while lung tissue (with relatively higher attenuation) is damaged. This is underpinned by Williams et al because mucus production is an early response to exposure with air-born harms, for example air pollution (Williams, 2006) that fits into our experimental set up.

Only a slight difference was observed between Gaussian curve "B" of SAO and CON groups (**Fig. 11.A, B**). Besides mean values of positions **(Fig. 11. bottom)** between each group, also width **(Fig. 11. middle)** of SAO group compared to CON group **(Fig. 5. middle)** did not changed significantly, despite that lung volume increases due to smoke exposure (Churg, 2008). Diseased areas in the lungs occurred and theoretically the destroyed walls of airways and alveoli could lead to emphysema (Wright, 1988). Indeed, according to Nagao and Murase FD analysis of air content inside the lungs represents emphysema well, but different technical parameters and calculation methods hinder the direct comparison of their results with our results (Nagao, 2002). In that case the expected compensatory increase of air in the lungs would decrease "the branching nature of airways", most likely reflected in our evaluation method as an increase of high parameter of Gaussian curve “A” and decrease of the same parameter in Gaussian curve “B”. However, emphysema, appears only in long term experiments through the inflammatory activation of CD8+ T cells (Maeno, 2007).

But the question arises: why was not position parameter of SDO group (**Fig. 5.B**) altered, when width was increased in such a spectacular manner? Probably in the case of voxels with COR that ordered them to Gaussian curve “B” the image gained from the results of increased density of lung tissue caused by inflammation was partially quenched by the also occurred mucus, which has a protective purpose (Williams, 2006) and appears in lower airways too (Churg, 2008) but is capable to form aforementioned plugs and micro-sized bubbles as well (Moldoveanu, 2009) (**Fig. 5. bottom**) as mentioned above.

According to ratio of height, between “A” and “B” Gaussian curve (**Fig. 5.C**), height and width of “B” Gaussian curve and the calculated C value (**Fig. 5.B and C**), we can state that all three groups could be distinguished by this novel radiomics-based pattern of FCF’s, characteristic to each tested air pollutant exposure. Mainly the feature of mucus inside the lungs and character of lung tissue’s inflammation too alter both of voxels attenuation values (and thereby COR) and the corresponding FD values, as well forming the mentioned FCFs. So SAO group could be distinguished from CON group, because fume derived nano-sized solid particles accumulate in deeper airways and alveoli (van Dijk, 2001; Lahnstein, 2008) and as inflammatory agents (Hassett, 2014) increase water permeability and dilates cell volume thickening of airway walls leading to narrowing of the airways (besides some mucus production) and therefore even minor alterations are reflected well in our radiomic approach using ratios of “A” and “B” Gaussian curve (**Fig. 11.C**). According to comprehensive details CT examinations - detecting the alterations of X-ray absorption quantities of diseased lung tissue – are supposed to result in increased number of voxels both with higher density (mucous tissues) and with lower density (cavities) in the reconstructed three-dimensional tissue density volumes. Spatial density patterns in small pulmonary regions could be very informative for diagnostic purpose.

Indeed the individual patterns of imaging and the parameters gained by calculations of FD number distributions and the comparison of their ratios (**Fig. 11.C**) in SDO, SAO and CON groups, hallmark the early effects of different air pollutants and presumably the development of the lung diseases such as bronchitis and COPD and/or asthma and lung cancer can be characterized too (van Rikxoort, 2013). Because the results obtained in our study (**Fig. 11.B,C**) could be the basis of differentiating those air pollutions in a very early stage by specific FCF pattern therefore we can suppose that the development of the lung diseases such as bronchitis and COPD and/or asthma and lung cancer can be characterized too (van Rikxoort, 2013). The molecular feature and presence of mucus in smaller airways (Williams, 2006) and inflammation profile of lung tissues (Jeffery, 1998) seems to be a key biomarker both of air pollutions and mayas well characterize certain diseases (for example COPD, asthma) because corresponds to inflammatory issues and therefore contribute to our CT and also FD analysis based results (Williams, 2006).

Thus, according to the literature (Williams, 2006; Churg, 2008.) we can suppose, that our method can be converted to human usage and it would enable to warn patients to avoid environmental exposure or to treat properly the symptoms of the early disease, prevent disease aggravation and avoiding the chances to exacerbate the COPD and/or asthma bronchiale symptoms. Here we highlight importance of time of exposure and genetic susceptibility (Churg, 2008; Maeno, 2007) to emphysema (Maeno, 2007) that may occur later and will be evidently reflected in the afore mentioned examined parameters (van Rikxoort, 2013).

However early symptoms of COPD could be similar to bronchitis as chronic bronchitis could also cause COPD due to the redundant regulation of the development of lung tissues forming the structures of the airways while lung cells proliferate, as a physiological response to compensate the necrosis of cells (Horowitz, 2009; Hinck, 2004). In vertebrates mainly fibroblast growth factor, transforming growth factor-β superfamily and bone morphogenic protein are involved in the development of lung structures. For secondary signal transmission the mitogen-activated protein kinase pathway is used, *inter alia* (Horowitz, 2009). In lung morphogenesis four families of guidance proteins (SEMAPHORIN and NEUROPILIN/PLEXIN, SLIT and ROBO, EPHRIN and EPH, and NETRIN and UNC5/DCC) and their receptors take part in a redundant manner, complemented with negative feedback regulatory pathways (Hinck, 2004). Thus, the source of harm may influence the ratios between damages of tissue types even in an early stage of lung diseases (Horowitz, 2009). But according to FCF in our experimental setup the SO_2 caused rather inflamed and mucous typed bronchitis (with air-bubbles), than damaged by emphysema (see above) – despite that chronic exposure of SO_2 may induce COPD as well (Wagner, 2006). This fact suggests that the FCF derived radiomic data represent the pathogenic process in lung diseases too, besides the early effects of air pollution (van Rikxoort, 2013; Nagao, 2002).

Still certain states of exposed tissues were well represented by calculated data of FCF, according to the demonstrated radiomics analysis results of experimental groups. FD and lacunarity parameters describe non-Euclidean structures (Al-Kadi, 2008; Mandelbrot, 1989; Fazzalari, 1996; Shlesinger, 1991; Nagao, 2002; Nagao, 2001; Helmberger, 2014) but also to certain COR correlated voxels (**Fig. 2.**) corresponding calculated FD values (**Fig. 6.**) represented alterations well, in comparison to other treatments (**Fig. 11.**) – in our experimental set-up even without calculation of lacunarity and avoiding gating technique. However calculation of lacunarity as well combined with additional FD calculation methods (for example porosity, connectivity) could be a promising basis of further methodical advances.

The essence of our findings means an automatic, comprehensive, quantitatively improved and early method for detection of air pollution exposure or therapy follow-up in the clinic and drug discovery/development in the laboratory. Moreover, this method and evaluation technique paves the way for environmental monitoring to make decisions about necessary interventions (see below).

5.3. Imaging of earthworms

5.3.1. Pre-treatment for optimal earthworm immobilization

Using Ringer solution the gastrointestinal soil content was totally eliminated. Earthworms kept in Ringer solution for at least 3 days instead of soil were more suitable for MR imaging purposes than animals used directly without removing soil from the intestinal lumen. Elimination of the gastrointestinal soil content reduced the signal level caused by magnetic susceptibility artifacts of MR imaging compared to those results where earthworms were kept in soil (data not shown). Also the immobilization of earthworms using propan-2-ol was distorted by soil content. However, according to our experiences with soil content in the intestines of earthworms the immobilization procedure can be still carried out, but the applied dose and time to totally immobilized state between individual earthworms may alter in a more exquisite manner, than in earthworms with empty intestines. This step may be essential to avoid the theoretical absorbance of the materials be the soil content of intestines – regardless of the experiment's purpose, which could be: testing of potential chemopreventive agents or environmental exposures, respectively. Thus, the purpose of experiments after this general pre-treatment can be selected: The pre-treatment can be complemented with either long term or short term exposures and potential chemopreventive effects as well to elucidate their effects.

Another important aspect is to avert dehydration as well as swelling of the earthworms. In group A, the earthworm's body mass remained near to the body mass measured on the first day until the third day unlike in earthworms body mass in group B caused by swelling due to Ringer solution (**Fig. 3. A and B**). Thus we can state that polystyrene plates in earthworm's boxes are capable to protect earthworms from swelling (and consequently death) because indeed they can climb on polystyrene plates *ad libitum* and thus prevent being totally immersed in fluid.

5.3.1.1. Immobilization of earthworms

Generally, with the dose range of propan-2-ol and ethanol used we observed effects on invertebrates approximately similar to those reported by Reagan-Shaw et al. where the article reports the calculation of pharmaceutical doses from humans to other vertebrates (Reagan-Shaw, 2007).

Diluted ethanol has anesthetic effects (Petrics, 1986), and using alcohols to immobilize earthworms have such benefits as a simple, reliable, non-invasive, and reversible approach. Further merit is that the animals do not extrude coelomic fluids, which is abundant in immune cells so called coelomocytes (Cooper, 2002). Therefore, immune-toxicological assessment of metal pollution on phagocytic activity (Brulle, 2006; Brulle, 2007) could remain intact. However, biochemical reactions may be influenced due to energy intake derived from metabolism of ethanol. This is supposed to distort the results of FDG PET imaging.

The gradual anaesthetizing method for earthworms utilizing propan-2-ol losing only minimal coeloma was successful, because to olfactory desensitization of animals to alcohol exists also among nematoda species (Bettinger, 2004). Thus, the opportunity to examine large sized earthworms metabolic parameters affected by Cd exposures *via* PET/MRI (utilizing FDG radiotracer) is open, especially because of Budán et al. used to immobilize earthworms propan-2-ol, which can be supposed not influencing directly the glucose uptake, neither the correlated metabolic reactions (Budán 2013a; Budán 2013b; Budán, 2014b).

The immobilizing effect is caused by direct influence of alcohol on the cell membrane. It is exerted by secondary intracellular transmitters, such as activation of the polyphospho-inositide-specific phospholipase C that triggers intracellular signaling responses. Through this pathway, more signal transmissions will be activated, including the formation of inositol-1,4,5-trisphosphate (IP3), the release of Ca2ţ from intracellular storage sites (Opper, 2010) with the consequent activation of cytosolic Ca2ţ - dependent enzymes and the formation of diacylglycerol leading to the stimulation of protein kinase C (Hoek, 1990). Another benefit is in using alcohols and leaving animals for 2–3 hr in the anesthetic fluid, the hearts of the animals could be stopped. Skin respiration still functions and this state is also reversible. With the mentioned “overdosing” the tested agents specific features pharmacokinetic (for example affinity to specific organs or tissues, practically to certain receptors) and pharmacodynamic (for example interactions with antagonists and biological responses) could be tested by “switching off” the circulation. Alcohols are appropriate anesthetic agents because in invertebrate among alcohol dehydrogenase (ADH) family only ADH3 isoenzyme exists (Albalat, 2009) and ADH3 oxidize low chained alcohols poorly (for example ethanol) or not at all (for example propan-2-ol) (Wagner, 1984).

The optimal immobilizing effect of propan-2-ol, compared to ethanol is because ethanol is metabolized by ADH3 enzyme into acetaldehyde that increases anion gap, unlike propan-2-ol. The increased anion gap causes acidosis and thereby can affect several physiological functions. Thus using alcohols as anesthetics the opportunity to repeat experiments with the same animal is possible.

Moreover, this anesthesia method of applying alcohols could be presumably extended to most of the *annelid* species (with proper modifications of the immobilization protocol, if needed).

5.3.2. Imaging of earthworms utilizing MRI

MRI is performed with higher efficiency if the target organism avoids internal muscle contractions and movements (**Fig. 12.**). Both of the chloragogeneous tissues and the kidneys (*nephridia)* seems to be important organs to indicate the Cd exposure, with FDG PET (see below). Also the reproductive organs relevance cannot be excluded.

According to Ramseier et al, in Cd exposed *L. terrestris* 85% to 95% of Cd quantity accumulated in intestinal and associated chloragogenous tissue (Ramseier, 1989). Indeed, Cd has a special affinity to the coelomocytes, see below (Shyamasree, 2017; Plytycz, 2011; Morgan, 2002; Molnár, 2012; Cotter-Howells, 2005). Thus, visualization of chloragogenous tissues may be useful for further experimental approaches, for example utilizing SPECT with ^{99m}Tc tracer, besides the PET with FDG tracer, (since microscopic alterations were already observed by Morgan et al. (Morgan, 2002).

Also it is important to mention, that the kidneys (*nephridia*) in earthworm as well as MTs molecules function in the similar way as in more developed species (Stürzenbaum, 2001). Stürzenbaum et al. highlighted more forms of MT and pointed on the importance of MT-2 in Cd excretion. However, the exact function of the kidneys in this aspects are still unknown, since MT-2 was concluded to sequester metals within acidified compartments more using lysosomes in the chloragogeneous tissues (Stürzenbaum, 2001).

Reproductive organs of earthworms are affected by Cd too, because Cd delays sexual maturation as well as inhibits reproduction (Takács, 2016). With the morphological visualization of this organs a novel way may be open to study possible morphological changings, induced by environmental effects. However, contrary that MRI enabled the visualization of reproductive organs, the exact comparison to control still may be hindered by the small size and complex shape of that organs.

5.3.3. Imaging of earthworms utilizing FDG PET

The ratio of mean last and mean first interval time's FDG uptake % of the frontal part of earthworms decreased in Cd exposed group in comparison to the control group, in statistical significant manner **(Fig. 14.**). Thus, the model is enabled indicating environmental exposure of Cd in the examined experimental set-up.

Chloragogenous tissue of earthworm is physiologically the analogue of the vertebrate liver in regard to carbohydrate metabolism, except from lactate-dehydrogenase function and hormonal regulation of metabolism, which clearly not exists in this species (Prento, 1987). Usually in earthworms the chloragogen cells as well as eleocytes bioaccumulate heavy metals, derived from the environment (Shyamasree, 2017; Plytycz, 2011; Morgan, 2002; Molnár, 2012; Cotter-Howells, 2005) due to the high riboflavin content (Galay-Burgos, 2003; Homa, 2010) see below. According to Prento P., in *L. terrestris* among normal circumstances the glucose level in body fluids, such as the blood as well as the coelomic fluid is in equilibrium and is as low as <0.01-0.05/µg/µl (Prento, 1987). In summary, Prento P. supposed, that all cell types (except the gut epithelium) in *L. terrestris* has the ability to take up glucose efficiently and also to building it into glycogen (Prento, 1987). However, the chloragogeneous tissue of *L. terrestris* has a low metabolic rate, in regard to dehydrogenase activity (Domínguez, 2018), but Cd exposure presumably damaged glucose transport enzymes and/or glucose storage and metabolism capacity of the chloragogeneous tissue. Indeed, at cellular level, the enzymes of the Krebs energy cycle - pyruvate and a-ketoglutarate dehydrogenase are vulnerable to Cd pollution too (Rea, 2018). Also, according to the literature, in hexokinase IV enzyme the SH groups are not involved in the actual catalytic process, but is supposed to help to stabilize the active enzyme's conformation (Fasella, 1963). Cd does possess a high molecular affinity to riboflavins (Shyamasree, 2017; Galay-Burgos, 2003; Homa, 2010). Thus, Cd targets with distinct mechanisms the coelomocytes (and at cell level the mitochondria), which are abundant in riboflavins (Plytycz, 2011). Thus, taking in consideration the mentioned equilibrium with coleoma in regard to glucose concentration, underpins exactly our results (Prento, 1987). Also here we need to highlight the aforementioned specific susceptibility of *L. terrestris* to heavy metal pollutants (Plytycz, 2011; Mazur, 2011).

It seems to contribute also to the observed difference between Cd exposed and control group, that in control animals other glucose storage function (for example glucose storage in the muscles), apart from the chloragogeneous tissues, are healthy. Indeed, glycogen are transported with chloragogen cells from chloragogeneous tissues into other organs of the earthworms (Prento, 1987). This is important, because we can suppose, that Cd exposed earthworms could not been able to take up as much quantity of FDG (in the upper body part) as the control because the mentioned equilibrium of glucose level among coleoma and other organs with time may decrease glucose (and in hexokinase reaction not reacted FDG) level from the upper body part to the lower body part. In the same time, the Cd exposure may also decrease transport and storage function, which increases in healthy animals the glucose (and FDG) level in organs of upper body part - because those organs are practically reservoir compartments for glucose (Prento, 1987).

However, behind the background of those results more phenomenon may co-exist. As an analogue of developed species, when they are exposed to Cd, then the dysfunctions or even failure of the kidneys may occur. Two reasons underpin this theory: first is that kidneys may have a high energy consumption needing a high glucose (or other energy-carrier molecules) catabolism activity. The second reason could correspond to the first reason (namely that kidneys are high energy consumers) but apart from that kidneys also reabsorb glucose (among others) utilizing an active transport enzyme system with several active protein groups – and Cd exposure impairs both of those functions. Indeed, kidneys have the potential to accumulate Cd (as mentioned earlier). For example rats have been treated with different Cd-binding proteins derived from *E. fetida* and earthworm protein-I (estimated molecular weight, 63,000-70,000 Daltons) and -II (estimated molecular weight about 7,000 Daltons) was recovered from the kidney supernatants, both as MTs. Thus, the proteins were degraded and thereby Cd liberated, which induced MT biosynthesis in the kidneys.

However, Cd bound to earthworm protein-III (estimated apparent molecular weight about 2,000 Daltons) was recovered primarily from urine indicating some elimination of Cd in that special experimental set-up (Suzuki, 1980).

Another aspect may influence the FDG uptake, that if Cd (or other causes) impair the kidneys, then losing of glucose (as well as the analogue of glucose, namely the potential quantity of FDG, which has not underwent the hexokinase-reaction) may occur, while their resorption is damaged and consequently glucosuria appears (Marsenic, 2009). Normally 20 % of FDG is excreted by humans with healthy kidneys, but according to Marsenic, in the case of impaired kidneys this occurs in a more exquisite manner (Marsenic, 2009). In the case of earthworms the loss of glucose and FDG is supposed to enter into the coleoma again, as mentioned above (Prento, 1987). Thus, theoretically this mechanism could exert a relevant effect on the uptake of FDG, namely that a greater part of FDG could have been excreted through the Cd damaged kidneys. This theory underpins our results, but it is important to mention, that the exact correlation of FDG uptake and renal failure in unclear, even in human clinical context. For example according to the study of Kode et al. the SUV of renal failure patients with the standard protocol times were proper, and no adjustment of their protocol was needed (Kode, 2017). (However, renal failure in human species is defined as an 85–90% loss of kidney function with a glomerular filtration rate less than 15 ml/min/1.73m^2 (Kode, 2017). Literature reported an association between the severity of the renal failure in patients and the inaccuracy of the SUVs (Yasuda, 1998). On the other hand, according to Toriihara et al. in chronic renal failure patients on hemodialysis has in the soft tissues, (such as spleen and blood pool) even significantly higher physiological FDG uptake occur, in comparison to the results of control group (with normal kidney function) (Toriihara, 2015).

Furthermore, oxidative damage caused by Cd exposure and cell damage (Novais, 2011) contributes directly and indirectly as well to the observed results, as mentioned above.

For the sake of completeness we can mention, that apoptotic cell death may take part also in Cd induced damage. According to Tokumoto et al, Cd increased P53 protein levels in NRK-52E cells (without stimulation of *P53* gene expression or inhibition of proteasome activity) but induced phosphorylation of P53 protein too and thereby caused apoptosis (Tokumoto, 2011). Also in vivo, the orally administrated Cd for 12 months in the mouse kidney did not induced severe kidney injury, but caused suppression of *UBE2D* genes and accumulation of P53 protein, leading to apoptosis in the cells of the renal tubules. Thus, *UBE2D* family members may be one of the critical targets of renal toxicity caused by Cd. However, Cd causes renal dysfunction with damage to kidney proximal tubule cells as well. The precise mechanisms behind those toxic effect remains unclear (Tokumoto, 2011), but the changes may be reflected in the results of FDG-PET imaging.

The exact placement of ROIs in regard to FDG-PET are troublesome, due to the aforementioned poor resolution of PET (Zang-Hee, 2011). In the earthworms the role of reproductive organs in FDG accumulation of the upper part of body could not been elucidated utilizing the current experimental model. Thus, FDG uptake of the chloragogenic tissues, kidneys (*nephridia*), theoretically the reproductive organs, or other stand alone organs too, as biomarker of environmental pollution may not established based upon this experimental set-up. Still, the parts of body above and below the *clitellum* can be discerned. This information may be enough to indicate Cd exposure utilizing this newly developed model.

In summary, we can state, that the kidneys of earthworms in regard to the decreased FDG uptake of the upper body part caused by Cd pollutant seems to contradict to the expectations – and apart from that the relevance of kidneys in the FDG signal of upper body seems to be at least secondary.

5.3.4. Limitations of earthworm model

Some examined biomarkers (especially some sensitive gene's expression pattern) could have been distorted by the mentioned pretreatment to ensure that the bowels of earthworms are empty. That could limit the utility of our experimental method and requires to validate the usefulness of our test according to each specific aspect as desired.

It is important to mention, that most likely other factors (for example organic compound depleting GSH (see above), or other metals with weak Lewis acidic attributions) may contribute to the Cd-related FDG uptake decreasing effect. Here we need to mention Vogel's ECW model, which enables the calculation of Lewis acidic-basic conditions when more compounds are presented with such a chemical behavior (Vogel, 1996). Thus, Vogel's ECW model could be utilized to estimate the contribution of other Lewis acidic agents to Cd's thiol-reacting groups depleting effects.

Also, protective factors (chelating agents, compounds with thiol-groups, antioxidants, etc.) may hide the deleterious effects of Cd (and/or other harmful materials). These influencing factors could be mapped with further analytical methods (for example mass-spectrometry (MS) or atomic absorption spectroscopy (AAS)).

At last we need to highlight, that Cd exerts partly specific effects in regard to metabolic enzymes, also in some aspects depending of species (Plytycz, 2011). For example in *E. fetida* after 8 weeks of exposure with 80 ppm Cd the activity of esterases, malate dehydrogenase, phosphoglucomutase and glutamate oxalate transferase were not affected (Scaps, 1997). However, the fast moving band after electrophoretic separation for phosphoglucose isomerase disappeared (Scaps, 1997). Thus some data in regard to enzyme activities may not be representative for other species.

6. CONCLUSION

The above presented novel animal models enable to detect early the mentioned health hazards (Szigeti, 2016; Budán, 2014a), or may advance the diagnosis of bone diseases, after clinical adaptation (Budán, 2018). The newly developed experimental set-ups with radiomics-based evaluation methods could improve health by early detection and sensitive monitoring the effects of the examined health hazards. The bone formation monitoring utilizing radiomics-based evaluation method as well as the attenuation value correlated FD distribution pattern analysis of the chest X-ray CT may be even adapted into clinical practice to monitor surgical, pharmaceutical, and physical therapies. Also, the radiomics-based evaluation methods could be used in other fields of environmental monitoring and protection too, for example indicating Cd pollution in the soil. Moreover, these methods are cost-effective, present quick and quantitative results, and utilize the smallest possible number of sample - in coherence with the European Union (EU) directive 2010/63/EU on the protection of animals (Hartung, 2010).

The locomotor organs and the lung diseases, or environmental health hazards besides the loss of health and life-quality also represents a heavy financial burden to individuals, families and society (Bone and Joint Initiative USA, 2016; Lopez, 2006). A great part of those costs could be avoided though, since opportunities are known to effectively prevent (or mitigate) hazards, or properly diagnose and treat consequential disease (see below). Exposure to environmental pollution can be minimized with proper monitoring, too. This enables interventions, if required (see below).

After clinical adaptations of the newly developed bone formation and chest X-ray CT quantitation methods still further studies are needed to gain knowledge about specificity and sensitivity. Also the soil pollution test needs further experiments to elucidate the Cd concentration, which can be statistically significantly detected.

6.1. The opportunities based upon the newly developed animal models, with radiomics-based evaluation

6.1.1. Possible applications of the bone formation model

The multimodal imaging of bone opacity and Tc-99m-MDP uptake changes, with radiomics based evaluation represents well the resultants of bone formation influencing factors. Presumably crosstalk amongst inflammatory cells, factors, and mechanisms, as well as the vascularization and presence of necessary minerals contribute to the observed results, fitting into the literature (Khan, 2000; Puetzer, 2010; Massari, 2019; Genant, 1974; Love, 2003; Albrektsson, 2001).

The reported novel multimodal ^{99m}Tc-MDP SPECT/CT radiomic approach may be useful to compare several experimental bone replacement materials in preclinical settings. In addition, tracking of clinical bone formation can be established based on the results of this study. Multimodal in vivo imaging with radiomics-based evaluation may support the optimal therapeutic strategy not only in correlation to bone healing, bone grafting and bone replacement, but also may advance the prognosis of the osteogenesis diseases.

6.1.2. Possible applications of the radiomics-based evaluation of the respiratory organ

Based on the below mentioned results, we can state that the classification could be distinguished in statistically significant manner without lung segmentation or ROIs (Szigeti, 2016). Moreover, we found a novel, reliable, accurate, automatized and remarkably faster than 8-24 weeks mentioned in the literature (Jobse, 2011), method to obtain radiomic-based data analysis using simple CT scans in a mouse experimental model. The implementation of our data analysis is straightforward and simple and to utilizing it in clinical CT images not requires any additional hardware. Furthermore as we could demonstrate the early diagnostic possibility of COPD-related lung and airway changes are close to clinical level noise-containing data (van Rikxoort, 2013). By defining the ratios of FD distribution functional parameters we are convinced, that the translation and validation of our algorithm and data analysis in human clinical data is warranted (van Rikxoort, 2013).

The radiomics analysis calculation of FCF may be useful for early diagnostic purposes of air pollution exposure and of the lung diseases too. As potential key biomarkers the molecular feature and pattern of mucus in smaller airways (Williams, 2006) as well as the inflammation profile of lung tissues (Jeffery, 1998) correlate to our results. Furthermore both of air pollutions caused inflammation and most likely certain diseases (for example COPD, asthma, etc.) may be also distinguished based upon their fine-patterns, probably opening new opportunities for early detection and treatment of lung diseases. It could be also extended to diagnosis and follow-up therapy of other inflammatory pulmonary diseases for example asthma, or cystic fibrosis (van Rikxoort, 2013), where pathologic mucus production is also (Williams, 2006) involved or other lung diseases with morphologic alterations, for example tuberculosis (Chen, 2014) or lung carcinomas (van Rikxoort, 2013).

6.1.3. Opportunities based upon the earthworm model

6.1.3.1. Opportunities of earthworm’s MRI

Utilizing T1 weighted spoiled gradient echo sequence and 3 dimensional acquisition scheme the whole intestinal tract and the corresponding special calciferous gland (gland of Morren) is visible at the 11-12th segment, as „black point”, an organ abundant of calcium. Reproductive organs are visualized, among others, as well (**Fig. 12**). However, the resolution has not enabled the exact signing of ROI to apply quantitative data analysis. Most likely with advanced experimental set-up and/or even larger sized earthworms species those hindrances could become overcome. For example the histopathological and morphological changes caused by heavy metal environmental exposure (namely Pb) may be detected in vivo with our novel model, if the technical opportunities improve (Tang, 2017). Presumably other heavy metal pollutants effect can be traced in a sensitive and quicker manner. Reliability could be tested if histopathological data could underpin the results, or typical organ-specific alterations could be highlighted (Tang, 2017).

Nevertheless, the frontal and hind part of earthworms can be distinguished properly. This enables to define position, necessary for multimodal PET/MRI fusion hybrid imaging.

6.1.3.2. Opportunities of earthworm’s PET imaging

The FDG uptake of earthworms indicate the environmental exposure of Cd in the examined experimental set-up.

Numerous environmental pollutions exert long lasting and well-known in vivo effects on aforementioned biomarkers and presumably independently from environmental moisture content and also absence of earth for at least the time of optimal pre-treatment (3 days) (Tang, 2017). For example, the certain exposures in annelids influence the following biomarkers: immuno-stimulants change composition and decrease the numbers of the coelomocytes (Homa, 2007; Homa, 2013), endocrine disruptors activate or antagonize estrogen receptors (Keay, 2012), heavy metal (for example Cd) pollution increases the expression of stress-related genes (heat shock proteins, MTs, GST, SOD, etc.) (Roh, 2006), or organic Pb compound cause morphological change (inflexible metameric segmentation) (Rao, 2003), certain organophosphorus insecticide inhibit acetylcholinesterase enzyme activity (Rao, 2004) and *per se* genotoxic heavy metal (trivalent and hexavalent Cr) damage DNA (evaluated on the earthworm's coelomocytes using the comet assay (Bigorgne, 2010; Budán, 2017), etc. (Shyamasree, 2017). These effects (or their indirect, secondary effects) may be followed-up utilizing in vivo imaging techniques, if suitable radiotracer could be administered in order to indicate properly the mentioned physiological effects. For example we can suppose, that the effects of other heavy metals (or even other harmful agents) could be detected with this method, after some modifications, namely utilizing 64-copper (^{64}Cu) isotopes (Carolyn, 2009).

Thus, the raw FDG uptake data (compared to an intact control) could be informative to recognize the presence of some harmful source(s) in a quick test, which - despite the available quantitative information - could have been practically used more as a qualitative test to decide if potential agricultural soils are seeming useful, or currently are they not useful due to heavy metal pollutants, and/or may underwent other, more specific, and costly as well as long-term, tests. Thus, the novel in vivo earthworm test could not only indicate potential health risk in a very fast manner, but also underpin decisions to examine more samples with other (analytical) methods, or not. Earthworms with already empty intestines, according to our method would need only to be treated with suspected heavy metal contaminated water (and compared to an intact control) (Budán, 2014a). Furthermore, soil samples could be macerated in aqueous medium, with the option to pretreat or without a pre-treating with acids to enhance the dissolution of heavy metals in water. Most likely the newly developed in vivo animal test with modifications could be adapted in order to carry out in situ soil tests. For example with the addition of DMBA or Cd or other ROS generating and GSH depleting agents, the harmful effects of 222-Radon (^{222}Rn) derived from the soil could be detected, when compared to standards or control, respectively.

6.2. Risk groups and interventions

The details of risk factors, which are corresponding to our studies, as well as all options for interventions are out of the scope of this dissertation. Nevertheless here we mention some risk groups of bone and lung diseases, or circumstances, when the monitoring of Cd level is warranted. Also we highlight the corresponding therapeutic options or interventions, respectively – based on the newly developed in vivo animal tests.

The proper application of those models (for example on risk groups - after necessary clinical adaptations, or to assess the effects of potential harmful environmental pollutants) may provide early and quantitative information, which could underpin decisions about therapeutic interventions, if they are necessary. Also they may enhance the decisions about choosing the suitable, properly fast, but also cost-effective interventions.

6.2.1. Risk groups

Smoking - besides the lung diseases - also contributes to the progression of osteoporosis and/or increase the risk of hip fracture (Kanis, 2005; Law, 1997). Indeed, recently Sasaki et al. highlighted in an animal model, that cigarette smoke exposure deteriorated bone quality of the lumbar vertebrae by disorientation of collagen fibers and the biological apatite c-axis (Sasaki, 2018). Moreover, smoking also increases Cd intake, as mentioned above (Ros, 1987; WHO, 2011).

6.2.1.1. Risk groups of bone diseases

Among population the high risk groups for bone diseases are people with poor Ca and vitamin D supply, people who do not have proper physical activity, or are at old age (above 65 years) as well as postmenopausal women. The same is true on people with less bodyweight or taking some medicines (for example glucocorticoids) (DHHS, 2004).

6.2.1.2. Risk groups of lung diseases

The prevalence of lung diseases are increased among people living in areas with polluted air, namely urban smog (for example combustion products), microsized dust, etc. Newborns and infants since they are especially susceptible for air pollution related diseases (WHO, 2005) as well as children and the elderly people, due to the narrowed airways, *inter alia*. (EPA 2014b). Also asthmatics, who are in high-risk populations the greater impact of SO_2 pollution, especially if elevated lung ventilation rates occur (for example during jogging, or while exercising and playing) (EPA 2014b). Genetic factors, such as Alpha 1-antitrypsin deficiency also increases the risk of lung diseases (Lucas, 2013).

Moreover, ^{222}Rn is a naturally occurring radioactive gas causing approximately the half of human annual background radiation exposure globally. Chronic exposure to ^{222}Rn (including its decay products) derived from soil and construction materials is estimated to be the second leading cause of lung cancer and neoplasms (while smoking is the first) (Robertson, 2013). ^{222}Rn exposure causes cancer of the lung among the general population from residential source and among underground miners the risk is *per se* higher (Ghissassi, 2009). Thus, the air pollution model could be utilized to detect higher ^{222}Rn exposure even without modifications.

6.2.1.3. Risk groups of cadmium poisoning

Byber K et al. summarized both the occupational and the general Cd exposure sources in a detailed manner (Byber, 2015). Here we need to highlight, that the risk to be affected by Cd's deleterious effects is additionally increased (besides the aforementioned smoking) among population living in areas near to some industrial and mining sites (Wu, 2016) or in such an urban region, where combustion gases are concentrated (JECFA, 1989; Ros, 1987; WHO, 2011; Friberg, 1986; Rea, 2018; Galal-Gorchev, 1991).

Further risk factor can be mineral deficiency of Ca, Zn and Fe, or the female gender, especially postmenopausal women (Kakei, 2013), or the presence of further nephrotoxic agents (for example As), as well as the decreased gene expression of MT, or occuring of autoantibodies against MT (Nordberg, 2012; Perry, 1976).

Drinking soft water, or living in a house with aqueducts built from old galvanized pipes or polyvinyl chloride (PVC) pipes may increase also Cd intake (Rea, 2018; Galal-Gorchev, 1991). The solubility of Cd in water increases when acidic conditions are presented. Thus, suspended or sediment-bound Cd may dissolve, increasing the concentration of Cd in water (Ros, 1987). Also food processing (because Cd was used as plating material in food industry) may increase the risk of Cd intake in certain foods, such as processed meats, refined grains, instant coffee, and cola drinks (Galal-Gorchev, 1991).

In working environments with high Cd exposure levels, workers have also developed hypercalciuria, phosphaturia, and polyuria and some have suffered from renal colic due to recurrent stone formation. In a few cases even renal failure occurs (Rea, 2018).

In the case of certain samples collected from the sites of potential soil pollutions (for example agricultural soils fertilized with superphosphate in the past) utilizing aforementioned chemical or physical treatments could provide more knowledge about the potential hazard of Cd (and other harmful materials). Also samples of leachate water could been collected from mining sites or from the vicinity of landfills. The same is true on water samples derived from older water pipes. Earthworms treated with these water samples (which could be optionally concentrated) instead of Ringer solution could only in a few hours (or days) present a proper results, which could underpin decisions about necessary interventions.

6.2.2. Preventions and interventions regard to the studied diseases and environmental pollution

Thus, the cessation of smoking may advance life expectancy greatly both of patients with osteoporosis, as well as patients with COPD - or at least improve outcome, for example slow down worsening of the symptoms. It is also important to mention, that primer (or even primordial) prevention of smoking, such as anti-smoking campaigns (Hu, 1995) if they are successful (Liu, 2009; Rohrbach, 2002) *per se* improves public health greatly, from the aspects of the aforementioned diseases (Blankenship, 2000).

6.2.2.1. Prevention or treatment of bone diseases

Generally speaking, for primer prevention of bone diseases the following factors are essential: appropriate physical activity, nutrition (intake of proper quantity of Ca and vitamin D, etc.), and to avoid smoking – and (if it is possible) to substitute medicaments, which possess the risk of deteriorating skeletal system (as a side effect). The secondary prevention, namely the early detection (for example with bone mineral density (BMD) test) and proper treatment are crucial to avoid crippling deformities and fractures. As tercier prevention to avert further health loss (for example fracture, etc.) specific, effective treatments (for example antiresorptive therapy) exist – and not only useful for the most frequent osteoporosis, but also for hyperparathyroidism, rickets, osteomalacia, and some congenital bone disorders or for bone disease associated with kidney failure. For severe cases also anabolic therapy and hip protector (to decrease change of fracture when the patient falls) is recommended (DHHS, 2004).

6.2.2.2. Strategies for ameliorating lung diseases symptoms and slow down progression

Avoiding air pollution as possible and cessation of smoking (Shaker, 2011) as well could decrease inflammation (Wright, 1990), improve the state of the symptoms and slow down progression of lung diseases. The importance of this study is that theoretically it could open the way for early intervention in less unequivocal cases, for example for elastase inhibitors to treat patients with emphysema (Madsen, 2012) or modulation of inflammatory agents with anti-inflammatory drugs, or blocking of intracellular signal transduction with mitogen-activated protein kinase inhibitors (Gergely, 2012).

To detect early COPD and asthma (Jobse, 2011) and to elucidate the exact role of involved cellular regulatory pathways, for example FGF2, transforming growth factor-β superfamily and BMPs (Horowitz, 2009) may be crucial for choosing the optimal therapeutic approach. For secondary signal transmission the mitogen-activated protein kinase pathway is used, *inter alia* (Horowitz, 2009). Therefore we can state, that if specific radiomics-based information can be possessed about the involved factors, then optimized individual therapy could be provided for patients in order to improve life expectancies.

Also early diagnosis and proper adjuvant therapy increases significantly the life expectancy of patients with lung cancer (Goffin, 2009). These methods efficacy could be examined from a novel viewpoint in a randomized placebo - control trial, utilizing our new in vivo chest CT approach. On the examined patients the chest CT could be performed after as well as previously the treatments.

6.2.2.3. Interventions to mitigate the hazards of environmental cadmium pollution

According to the Agency for Toxic Substances and Disease Registry (ATSDR) the monitoring of risk groups (as part of the secondary prevention) can be performed by measuring urinary Cd (which is an indicator of internal dose), or low-molecular weight (LMW) proteinuria, etc. (ATSDR, 2008; Järup, 2009). European Food Safety Authority (EFSA) determined a tolerable weekly intake (TWI) of 2.5 μg/kg Cd based on relationship between urinary Cd levels and tubular proteinuria (assessed by beta-2-microglobulin excretion) (EFSA, 2009; Järup, 2009) To avoid occupational harmful effects of Cd the exposure needs to be kept below the threshold limit value (TLV), which is both for Cd dust and fumes 0.05 mg/m^3 (Rea, 2018). Nevertheless, representative leachate water samples collected in the vicinity of such workplaces, industrial areas or landfills may represent Cd pollution and with our novel method could been examined.

The practical benefit of such monitoring is obvious, since from 1980 to 2011 an intervention program of soil replacement in the polluted paddy fields was continually carried out, with the purpose to decrease Cd pollution (Aoshima, 2012). Also industrial techniques in order to prevent soil pollution are applied (Yoshida, 1999). Nevertheless still advanced monitoring methods are carried out to detect environmental Cd level (Yoshida, 1999).

Besides the costly soil replacement a novel promising technology has been developed, namely the bioremediation. Bioremediation utilizes microorganisms, which enable to remove or recover heavy metals from polluted water as well as lands, either ex situ or in situ (Aoshima, 2012; Yoshida, 1999). The microorganisms used in bioremediation developed and adopted different detoxifying mechanisms such as biosorption, bioaccumulation, biotransformation and biomineralization (Ruchita, 2015). Decadmiation, or the removal of Cd from fertilizer during manufacturing is only technically feasible for fertilizers based on phosphoric acid, because acid can be treated with ion exchangers, in order to remove Cd selectively by complexing or precipitating it (Vermeul, 1996).

In summary, we are convinced, that the aforementioned strict monitoring of Cd pollution is necessary (Dixit, 2015) and it may be improved utilizing our novel in vivo earthworm test system, using multimodal imaging data acquisition with radiomics-based evaluation approach.

7. SUMMARY

Multimodal in vivo (X-ray CT/SPECT/PET/MRI) fusion hybrid imaging provides quantitative, comparable, sensitive, longitudinal and robust data, revealing important anatomical and functional information, respectively. Radiomics data handling and evaluation is an approach to increase further the biological value of information obtained by in vivo imaging. These data can be either morphologic, results of biochemical reactions, as well as positions of moving organ’s time-related information. The purpose of radiomics is to increase reliability, precision, accuracy or robustness of data, or decrease sample number, respectively. The main goal of this study, was to examine and present a spectrum of radiomics-based imaging in animal experiments, with the opportunity to adapt it to individual clinical imaging or monitoring of environmental systems, respectively.

In developed countries the diseases of locomotor- and the respiratory- system are among the major public health problems. The latter is exacerbated by air pollution. Apart from that, environmental pollution is continuously growing and it exerts harmful effects on mankind in multifarious ways.

According to the estimations in 2004 in the US leading to approximately 1.5 million fractures, which required bone grafting in ca. 500.000 cases. According to the WHO in 2012 around 7 million people died as a result of air pollution, including 3.1 million premature deaths caused by indoor and urban outdoor air pollution. In 2016 the air pollution is estimated to reduce the average global life expectancy with 1 year. According to the EPA sulfur dioxide and ground-level ozone precursors (nitrogen oxides and volatile organic compounds) derived mainly from fuel combustion are among the most frequent health hazards. Mineral oil and heavy metals are waste products mostly of municipal, industrial and commercial sectors and they represent 60% of soil pollution. Among them Cd has the ability to accumulate with biomagnification process, the excretion of Cd is very slow but its deleterious effects are severe and multifarious. Therefore possible contamination with Cd requires to be minimized.

Our research group has established *in vivo* animal models utilizing radiomics-based evaluation to elucidate details of bone formation (bone graft healing) and air-pollution related lung diseases. Also a novel in vivo imaging approach to detect the effect of soil pollutant Cd in earthworm (*Eisenia hortensis* and *Lumbricus terrestris*) was developed.

Utilizing X-ray CT and MDP SPECT with radiomics-based evaluation enabled the statistically significant discerning of poly (methyl methacrylate)-based bone cement graft (PMMA) and albumin coated, sterilized, antigen-extracted freeze-dried human bone grafts (HLBC). With X-ray CT reconstructed attenuation corresponding specific voxel's fractal dimension distribution profile, abstracted their quantity with histograms, separated to Gaussian-curves with calculated descriptive parameters, the discerning from each other of a sulfur dioxide gas exposed, of an air-diluted fresh mainstream cigarette smoke mixed with ozone-air gas mixture treated, and also of a control group was enabled. Using in vivo earthworms, after proper immobilization, the early effect of Cd pollution was revealed with FDG PET/MRI modalities.

Multiple testing with the same animal, combined with radiomics-based evaluation methods increased cost-effectivity and decreased the necessary sample number of animals, in coherence with the European Union (EU) directive 2010/63/EU on the protection of animals.

The health hazards and diseases investigated in the present work are prime examples of high individual and societal costs both in quality of life and in financial sense. The combination of screening, imaging and radiomics-based monitoring offers and effective opportunity to diagnose early and treat properly the lung or bone diseases and also to minimize the exposure of environmental pollutions. Moreover the bone formation evaluation method as well as the attenuation value correlated FD distribution pattern analysis of the chest X-ray CT may be even adapted into clinical practice to monitor surgical, pharmaceutical, and physical therapies. The developed earthworm test system may enhance the required strict environmental monitoring. This can even underpin decisions to decrease Cd concentration with the extensive and costly soil replacement intervention, if it is necessary.

The thesis also leads the way to further more widespread studies both in clinical prevention and environmental protection enhanced by radiomics evaluation methods of image data.

8. ACKNOWLEDGEMENT

I would like to express my sincere gratitude to Dr. Zoltán Gyöngyi, my supervisor, for his patient and selfless support and guidance not only as a scientist but also as a man throughout the years I spent in his team.

I also thank Dr. Domokos Máthé and Dr. Krisztián Szigeti for providing me the opportunity to work in the CROmed Translational Research Centers, which always embraced me with its friendly and supporting atmosphere.

I would like to thank Professor István Kiss for providing me a supportive environment in the Department of Public Health Medicine to finish my doctoral thesis.

I especially thank Dr. Károly Berényi the valuable support to carry out statistical analysis, and Miklós Weszl, Noémi Kovács, Ildikó Horváth, and Gellért Gerencsér, who supported the experimental work.

I also would like to thank to all contributors, co-authors, my colleagues in the laboratory and in the Institute, and my friends for their help throughout my studies.

Finally, I thank my parents, my family and my love, for their encouragement and support.

The present dissertation was supported by EFOP 3.6.1-16-2016-00004.

9. PUBLICATION LIST

9.1.Publications related to the present thesis

F. Budán, N. Kovács, P. Engelmann, I. Horváth, DS. Veres, P. Németh, K. Szigeti, D. Máthé:
Longitudinal in vivo MR imaging of live earthworms
Journal of Experimental Zoology Part A: Comparative Experimental Biology
J Exp Zool A Ecol Genet Physiol. 321(9) pp: 479-89. 2014.
i.f.:1,349
cit.:1
independent cit.: 1

K. Szigeti, T. Szabó, C. Korom, I. Czibak;ó, I. Horváth, D.S. Veres; Z. Gyöngyi, K. Karlinger, R. Bergmann, M. Pócsik, F. Budán, D. Máthé:
Radiomics-based differentiation of lung disease models generated by polluted air based on X-ray computed tomography data
BMC Medical Imaging 16(1)14. 2016. doi: 10.1186/s12880-016-0118-z
i.f.: 1,31
cit.: 9
independent cit.: 8

F. Budán, Krisztián Szigeti, Miklós Weszl, Ildikó Horváth, Erika Balogh, Reem Kanaan, Károly Berényi, Zsombor Lacza, Domokos Máthé, Zoltán Gyöngyi:
Novel radiomics evaluation of bone formation utilizing multimodal (SPECT/X-ray CT) *in vivo* imaging
PLoS ONE 13(9): e0204423. 2018
i.f.: 2,766
cit.:1
independent cit.: 1

9.2. Presentations related to the present thesis

F Budán, N Kovács, I Horváth, DS Veres, P Engelmann, P Németh, K Szigeti, D Máthé
PET/MRI/SPECT/CT in vivo longitudinal imaging of Earthworm (Lumbricus terrestris L.), as a novel means of environmental monitoring
Word Molecuar Imaging Congress (WMIC) Poster Session 4 P535
WMIC, Savannah, GA, USA, 2013. 09. 18-21.

F. Budán, N. Kovács, I. Horváth, D. Veres, P. Engelmann, P. Németh, K. Szigeti, D. Máthé: PET/MRI/SPECT/CT in vivo longitudinal imaging of Earthworm (Lumbricus terrestris L.), as a novel aspect for toxicological testing. P494. 16:00 European Association of Nuclear Medicine (EANM) Poster Session 3 **(**Exhibit Hall B) P494**.** France, Lyon, 2013. 09. 19-23.

Budán F., Szigeti K., Szabó T., Horváth I., Veres D., Czibak I., Korom Cs., Karlinger K., Máthé D.:
Tüdőbetegségek korai felismerése röntgen CT fraktáldimenzió-számítás alapú kiértékelésével
Fiatal Higiénikusok X. Fóruma.
Pécs, Hungary, 2014, 05. 14-16.
Egészségtudomány. 2014 (2) 16.

D. Máthé, F. Budán, Cs. Korom, D.S. Veres, K. Szigeti
Early X-ray CT radiomic identification of lung tissue harm origins in mice
EANM, Hamburg, Germany, 2015. 10. 10-14.

Budán F., Szendi K., Bodó K., Diós P., Horváth I., Szigeti K., Máthé D., Engelmann P., Gyöngyi Z., Gerencsér G., Varga Cs.:
Akut kadmium és UV sugárzás interakcióinak kimutatása kerti giliszta (Eisenia hortensis) fajban, fejlesztett „üstökös vizsgálat” (comet assay) módszerrel
Magyar Higiénikusok Társasága LXIV. Vándorgyűlése

Győr, 2016. 10. 5-7.
Egészségtudomány 2017.(1) 84-85.

Budán F., Szabó N., Gerencsér G., Szigeti K., Máthé D., Gyöngyi Z.:
Radiomikai biomarkerek fejlesztése a népegészségtan szolgálatában
Népegészségügyu képző- és kutatóhelyek országos egyesületének XII. Konferenciája
Népegészségügy, 2018 (2) 89
Budapest, Hungary. 2018. 08. 29-31.

Radiomics evaluation of multimodal (SPECT/X-ray CT) in vivo imaging of a bone healing model
F. Budán, K. Szigeti, M. Weszl, K. Berényi, N. Szabó, Zs. Lacza, D. Máthé, Z. Gyöngyi
Népegészségügyi Képző-és Kutatóhelyek Országos Egyesületének XII. Konferenciája
Népegészségügy, 2018 (2) 92
Budapest, Hungary 2018. 08. 29-31.

9.3 Other own publications, mentioned in the thesis

Budán F, Varjas T, Nowrasteh G, Varga Z, Boncz I, Cseh J, Prantner I, Antal T, Pázsit E, Gobel G, Bauer M, Gracza T, Perjési P, Ember I, Gyöngyi Z. Early modification of c-myc, Ha-ras and p53 expressions by N-methyl-N-nitrosourea. 2008. In Vivo. 22(6):793-797.

Diós P, Szigeti K, Budán F, Pócsik M, Veres DS, Máthé D, Pál S, Dévay A, Nagy S. Influence of barium sulfate X-ray imaging contrast material on properties of floating drug delivery tablets. 2016.Eur J Pharm Sci. 95:46-53.

Diós P, Nagy S, Pál S, Pernecker T, Kocsis B, Budán F, Horváth I, Szigeti K, Bölcskei K, Máthé D, Dévay A. Preformulation studies and optimization of sodium alginate based floating drug delivery system for eradication of Helicobacter pylori.

2015. Eur J Pharm Biopharm. 96.196-206.

Gergely P, Budán F, Szabó I, Mezey G, Németh Á, Huszár A, Iványi J, Gombos K, Knapp Á, Őrfi L, Kéri G, Ember I. Kinase inhibitors reduce 7,12-dimethylbenz[a]anthracene-induced oncosuppressor gene expression in short-term experiments. 2012. Eur. J. Oncol (17)1, 11-21.

Szigeti K, Hegedűs N, Rácz K, Horváth I, Veres DS, Szöllősi D, Futó I, Módos K, Bozó T, Karlinger K, Kovács N, Varga Z, Babos M, Budán F, Padmanabhan P, Gulyás B, Máthé D. Thallium Labeled Citrate-Coated Prussian Blue Nanoparticles as Potential Imaging Agent. Contrast Media & Molecular Imaging. Paper 2023604. 10 p. 2018.

10. LIST OF ABBREVIATIONS

^{11}C	11-carbon
^{123}I	123-iodine
^{13}N	13-nitrogen
^{15}O	15-oxygen
^{18}F	18-fluor
^{222}Rn	222-Radon
^{32}P	32-phosphorus
3D	3 dimensional
^{45}Ca	45-calcium
^{64}Cu	64-copper
^{67}Ga	67-gallium
^{68}Ga	68-gallium
^{99m}Tc	99-technetium
AAS	atomic absorption spectroscopy
ADAM9	*A disintegrin and metalloproteinase 9*
Ag	silver
Al	aluminium
As	arsenic
ATSDR	Agency for Toxic Substances and Disease Registry
BI	binary images
BMD	bone mineral density
BMPs	bone morphogenic proteins
Ca^{2+} ion	calcium ion
CAD	computer-aided diagnosis and detection
CBCT	conebeam CT
Cd	cadmium
CD	Crohn’s disease
CDMI	Crohn’s Disease Magnetic Resonance Imaging Index
CHCs	chlorinated hydrocarbons
CM	contrast materials
Co	cobalt
COPD	chronic obstructive pulmonary disease
COR	cut-off range
Cr	chromium
CrVI	hexavalent chromium
CT	X-ray computed tomography
CTA	coronary CT angiography
Cu	copper
Cs	cesium
DAT	123I-ioflupane-dopamine transporter
DCE-CT	dynamic contrast-enhanced computed tomography
DFS	disease free survival
DMBA	7,12-dimethylbenz[a]anthracene
DNA	deoxyribonucleic acid
DXA	dual X-ray absorptiometry
EDX	energy-dispersed X-ray microanalysis

EFSA	European Food Safety Authority
EGFR	epidermal growth factor receptor
EPA	United States Environmental Protection Agency
FCF	FD – COR mathematical function
FD	fractal dimension
FDG	18F- fluor-dezoxy-glucose
FDK	Feldkamp–Davis–Kress
Fe	iron
FEV	forced expiratory volume
FGF-2	fibroblast growth factor 2
fMRI	functional MRI
GABA	γ-aminobutyric acid
GIT	gastrointestinal tract
GLCM	gray level co-occurrence matrix
GLRLM	gray-level run-length matrix
GSH	glutathione
GSTs	glutathione S-transferases
H	protium
Hg	mercury
HU	Hounsfield Unit
ICV	intracerebroventricular
IDMN	normalized inverse difference moment
IGF-I	insulin-like growth factor 1
IP3	inositol-1,4,5-trisphosphate
LASSO	Least Absolute Shrinkage and Selection Operator
LMW	low-molecular weight
LOR	last output reference
LUT	lookup tables
MACE	major adverse cardiac events
MAO	monoamine oxidase
MaRIA	Magnetic Resonance Index of Activity
MBB	E-2-(4’-methoxybenzylidene)-1-benzosuberone
MEGS	Magnetic Resonance Enterography Global Score
MIP	maximum intensity projection
Mn	manganese
MNU	N-methyl-N-nitrosourea
Mo	molybdenum
MRE	magnetic resonance enterography
MRI	magnetic resonance imaging
MS	mass-spectrometry
MTs	methalothioneines
NAD^+/NADH ratio	ratio of oxidized and reduced forms of nicotinamide adenine dinucleotide
Ni	nickel
NMR	nuclear magnetic resonance
NRS	napkin-ring sign
OECD	Organisation for Economic Co-Operation and Development
OHAT	US Office of Health Assessment and Translation

OS	overall survival
PAHs	polycyclic aromatic hydrocarbons
Pb	lead
PET	positron emission tomography
PH	pulmonary hypertension
PO_4^{3-} ion	phosphate ion
RAS	renine-angiotensine system
RF	Random forest
ROI	region of interest
ROS	reactive oxygen species
SD	standard deviation
Se	selenium
SEM	scanning electron microscopy
SIMPle	Small Intestinal MRI Pathology Inflammation Score
SO_2	sulfur dioxide gas
SOD	superoxide-dismutase
SPECT	single photon emission tomography
Sr	trontium
STP	standard pressure and temperature
SUV	standardized uptake volume
Tc-99m-MDP	^{99m}Tc-Methyl diphosphonate
TEM	transmission electron microscopy
TGFb	transforming growth factor b
TGF-β1	transforming growth factor β1
TLV	threshold limit value
TWI	tolerable weekly intake
U	uranium
VEGF	vascular endothelial growth factor
VOC	volatile organic compounds
VOI	voxels of interests
WHO	World Health Organisation
Zn	zinc

11. REFERENCES

[Aberg, 2011] Aberg, J. et al., (2011) In vivo evaluation of an injectable premixed radiopaque calcium phosphate cement. Int J Biomater. 2011;2011:232574. doi: 10.1155/2011/232574

[Aerts, 2014] Aerts HJWL., et al., (2014) Decoding tumour phenotype by noninvasive imaging using a quantitative radiomics approach. Nature Communications 5:4006

[Agbandji, 2012] Agbandji L, E.A. et al., (2012) Comparison of heavy metals contents for some cigarettes brands. Am. J. Pharmacol. Toxicol., 7: 149-153.)].

[Albalat, 2009] Albalat R., (2009) The retinoic acid machinery in invertebrates: ancestral elements and vertebrate innovations. Mol Cell Endocrinol 1-2:23–35.

[Albrektsson, 2001] Albrektsson, T., Johansson C. (2001) Osteoinduction, osteoconduction and osseointegration. Eur Spine J. 10 :S96–S101. DOI 10.1007/ s005860100282

[Al-Kadi, 2008] Al-Kadi OS., Watson D. (2008) Texture Analysis of Aggressive and Nonaggressive Lung Tumor CE CT Images. IEEE Transactions on Biomedical Engineering 55: 1822-1830. ; EPA (United States Environmental Protection Agency) 1996. Oxidant Air Pollutants and Lung Cancer: An Animal Model. Available: http://cfpub.epa.gov/ncer_abstracts/index.cfm/fuseaction/display.abstractDetail/abstract/2323 [accessed 11. 12. 2014]

[Anat, 1983] Anat, J. (1983) 136, 1, pp. 1-14 Printed in Great Britain Remodelling of bone and bones: growth of normal and transplanted caudal vertebrae S. A. Feik and E. Storey

[Andersson, 2003] Andersson HLA-S, et al., (2003) Response of rat osteoblast-like cells to microstructured model surfaces in vitro. Biomaterials. (24)4, 649-654.

[Annadhason, 2012] Annadhason A. (2012) Methods of Fractal Dimension Computation. International Journal of Computer Science and Information Technology & Security (IJCSITS).(2)1.ISSN: 2249-9555

[Aoshima, 2012] Aoshima K. (2012) [Itai-itai disease: cadmium-induced renal tubular osteomalacia]. [Article in Japanese]. Nihon Eiseigaku Zasshi. 67(4):455-63

[Apte, 2018] Apte JS, et al., (2018) Ambient PM2.5 Reduces Global and Regional Life Expectancy. Environ. Sci. Technol. Lett., 5 (9) 546–551

[Aspenberg, 1990] Aspenberg P, Thoren K. (1990) Lipid extraction enhances bank bone incorporation. An experiment in rabbits. Acta Orthop Scan. 61: 546-548

[ATSDR, 2008] ATSDR, (2008) Draft toxicological profile for cadmium. September Atlanta, GA: Agency for Toxic Substances and Disease Registry. 450

[Bach, 2012] Bach PB, et al., (2012) Benefits and harms of CT screening for lung cancer: a systematic review. JAMA. Jun 13;307(22):2418-29. doi: 10.1001/jama.2012.5521

[Badawi, 2000] Badawi, A. F. et al., (2000) Effect of chlorinated hydrocarbons on expression of cytochrome P450 1A1, 1A2 and 1B1 and 2- and 4-hydroxylation of 17β-estradiol in female Sprague-Dawley rats. Carcinogenesis. (21)8 1593–1599

[Basdra, 1999] Basdra EK, and Komposch G. (1999) Komposch G. Transmission and scanning elecron microscopic analysis of mineralized loci formed by human periodontal ligament cells *in vitro*. J Orofac Orthop 60, 77-86

[Bettinger, 2004] Bettinger JC, McIntire SL. (2004) State-dependency in C. elegans. Genes Brain Behav. 3(5):266-72

[Bigorgne, 2010] Bigorgne E, et al., (2010) Genotoxic effects of nickel, trivalent and hexavalent chromium on the Eisenia fetida earthworm. Chemosphere 80:1109–1112

[Blankenship, 2000] Blankenship, KM, Bray, SJ, Merson, MH, (2000) Structural interventions in public health Blankenship. AIDS. 14 (suppl 1) 511-521

[Blazsek, 2009] Blazsek J, et al. (2009) Aminobisphosphonate stimulates bone regeneration and enforces consolidation of titanium implant into a new rat caudal vertebrae model. Pathol Oncol Res. ;15: 567–577

[Blumgart, 1926] Blumgart HL and Yens OC (1926) Studies on the velocity of blood flow: I. The method utilized. J Clin Invest. 4, 1–13

[Bone and Joint Initiative USA, 2016] Bone and Joint Initiative USA. (2016) The Impact of Musculoskeletal Disorders on Americans — Opportunities for Action. Bone and Joint Initiative USA.

[Bonewald, 2003] Bonewald LF, et al., (2003) Staining alone is not sufficient to confirm that mineralization in vitro represents bone formation. Calcif Tissue Int. (5)72 537 – 47

[Borah, 2001] Borah B, et al., (2001) Three-dimensional microimaging (MRmicroI and microCT), finite element modeling, and rapid prototyping provide unique insights into bone architecture in osteoporosis. Anat Rec. 265(2) 101-110.

[Bossé, 2010] Bossé Y, et al., (2010) It's Not All Smooth Muscle: Non-Smooth-Muscle Elements in Control of Resistance to Airflow. Annu Rev Physiol 201072: 437-462

[Bostrom, 2005] Bostrom M.P.G, Seigerman D.A. (2005) The Clinical Use of Allografts, Demineralized Bone Matrices, Synthetic Bone Graft Substitutes and Osteoinductive Growth Factors: A Survey Study, First Online: 09 September

[Bousquet, 2007] Bousquet J, Dahl R, Khaltaev N. (2007) Global Alliance against Chronic Respiratory Diseases. Eur Respir J. 29: 233–239.

[Boyde. 1976] Boyde A. (1976) Scanning electron microscopic studies of bone. The biochemistry and physiology of bone. New York, NY7 Academic Press

[Braman, 2006] Braman SS., (2006) The global burden of asthma. Chest. 130(1 Suppl):4S-12S.

[Brousseau, 1997] Brousseau P, et al., (1997) Evaluation of earthworm exposure to contaminated soil by cytometric assay of coelomocytes phagocytosis in *Lumbricus terrestris* (Oligochaeta). *Soil Biol Biochem.* 29(3-4):681-684.

[Brulle, 2006] Brulle F, et al. (2006) Cloning and real-time PCR testing of 14 potential biomarkers in Eisenia fetida following cadmium exposure. Environ Sci Technol 8:2844–2850.

[Brulle, 2007] Brulle F, et al,. (2007) The strong induction of metallothionein gene following cadmium exposure transiently affects the expression of many genes in Eisenia fetida: a trade-off mechanism? Comp Biochem Phys C 4:334–341

[Bruns, 2001] Bruns E, et al., (2001) Bioaccumulation of lindane and hexachlorobenzene by the oligochaetes Enchytraeus luxuriosus and Enchytraeus albidus (Enchytraeidae, Oligochaeta, Annelida). Hydrobiologia. 463:185–196.

[Buchman, 1998] Buchman SR, et al., (1998) Use of microcomputed tomography scanning as a new technique for the evaluation of membranous bone. J Craniofac Surg 9(1):48-54

[Bucholz, 2002] Bucholz, RW., (2002) Nonallograft osteoconductive bone graft Substitutes. Clin Orthop 395:44Y52

[Budán, 2008a] Budán F. et al., (2008a) Early modification of c-myc, Ha-ras and p53 expressions by N-methyl-N-nitrosourea. In Vivo 22(6) 793-798

[Budán, 2008b] Budán F. et al., (2008b) Studies on the potential molecular biomarkers of environmental methyl-nitroso-urea exposure. Hungarian Epidemiology. 5(1) 55-62. [abstract in English

[Budán, 2008c.] Budán F. et al, (2008c) Early modification of c-myc, Ha-ras and p53 expressions by chemical carcinogens. Hungarian Epidemiology. 5(3-4) 201-212. [abstract in English]

[Budán, 2009a] Budán F., et al., (2009a) The effect of E-2-(4'-methoxybenzylidene)-1-benzosuberone on different key gene expression of mice exposed to N-methyl-N-nitrosourea 17 th Congress of Society of Public Health. Romania, Tirgu Mures 17-19 April, Hungarian Epidemiology Supplementum, 6: 2009, pp: 27

[Budán, 2009b] Budán F. et al (2009b) Az E-2-(4-metoxibenzilidén)-1-benzoszuberon (MBB) előkezelés okozhatta-e az onko/szuppresszor gének expressziójának emelkedését metil-nitrozó-karbamid (MNU) karcinogénnel kezelt CBA/Ca egerek májában? Congressus Pharmaceuticus Hungaricus XIV. Budapest, november 13-15. Gyógyszerészet 53. 522-526. 2009. Supplementum pp: 81 [abstract in Hungarian]

[Budán, 2009c] Budán F. et al, (2009c) Early Modification of c-myc, Ha-ras and p53 Expressions by Chemical Carcinogens (DMBA, MNU). In Vivo 23(4) 591-598.

[Budán, 2013a] Budán F. et al., (2013a) PET/MRI/SPECT/CT in vivo longitudinal imaging of Earthworm (Lumbricus terrestris L.), as a novel aspect for toxicological testing. P494. 16:00 European Association of Nuclear Medicine (EANM) Poster Session 3 **(**Exhibit Hall B) P494**.** France, Lyon, 19-23 October, 2013

[Budán, 2013b] Budán F. et al., (2013b) PET/MRI/SPECT/CT in vivo longitudinal imaging of Earthworm (Lumbricus terrestris L.), as a novel means of environmental monitoring. Word Molecuar Imaging Congress (WMIC) Poster

Session 4 P535 WMIC, Savannah, GA, USA, 09. 18-21

[Budán, 2014c] Budán F, et al (2014c) Longitudinal in vivo MR imaging of live earthworms. J. Exp. Zool. 9999A:1–11

[Budán, 2014b] Budán F, et al (2014b) Longitudinal in vivo MR imaging of live earthworms Journal of Experimental Zoology Part A: Comparative Experimental Biology J Exp Zool A Ecol Genet Physiol. 321(9). 479-489.

[Budán, 2014a] Budán F, et al (2014a) Tüdőbetegségek korai felismerése röntgen CT fraktáldimenzió-számítás alapú kiértékelésével. Fiatal Higiénikusok X. Fóruma. Pécs, 2014, 05. 14-16. Egészségtudomány 2014. (2) 16.

[Budán, 2017] Budán F, et al 2017 Akut kadmium és UV sugárzás interakcióinak kimutatása kerti giliszta (Eisenia hortensis) fajban, fejlesztett „üstökös vizsgálat" (comet assay) módszerrel. Magyar Higiénikusok Társasága LXIV. Vándorgyűlése. Győr, 2016. 10. 5-7. Egészségtudomány. É2017. (1). 84-85.

[Budán, 2018b] Budán F, et al., (2018b) Novel radiomics evaluation of bone formation utilizing multimodal (SPECT/X-ray CT) *in vivo* imaging. PLoS ONE 13(9): e0204423.

[Budán, 2018a] Budán F, et al., (2018a) Radiomikai biomarkerek fejlesztése a népegészségtan szolgálatában Népegészségügyu képző- és kutatóhelyek országos egyesületének XII. Konferenciája, Népegészségügy, 2: 2018, pp: 89, Budapest, augusztus 29-31.

[Budán, 2018c] Budán F, et al., (2018c) Radiomics evaluation of multimodal (SPECT/X-ray CT) in vivo imaging of a bone healing model. Népegészségügyi Képző-és Kutatóhelyek Országos Egyesületének XII. Konferenciája, Népegészségügy, 2: 2018, pp: 92, Hungary, Budapest 29-31 August

[Busato, 2016] Busato A, et al., (2016) In vivo imaging techniques: a new era for histochemical analysis. European Journal of Histochemistry; 60:2725

[Byber, 2015] Byber K, (2015) Cadmium or cadmium compounds and chronic kidney disease in workers and the general population: a systematic review. Critical Reviews in Toxicology. DOI: 10.3109/10408444.2015.1076375

[Carolyn, 2009] Carolyn J. A, Riccardo F. (2009) Radiopharmaceuticals for PET Imaging of Cancer: Advances in Preclinical and Clinical Research. Cancer Biother Radiopharm. 24(4) 379–393

[Castañer, 2005] Castañer E, et al., (2005) Diseases affecting the peribronchovascular interstitium: CT findings and pathologic correlation. Curr Probl Diagn Radiol. 34: 63-75

[Cederbaum, 2012] Cederbaum AI. (2012) Alcohol metabolism. Clin. Liver. Dis. 16(4). 667-685

[Celli, 2004] Celli BR, et al., (2004) The Body-Mass Index, Airflow Obstruction, Dyspnea, and Exercise Capacity Index in Chronic Obstructive Pulmonary Disease. N Engl J Med 350: 1005-12

[Chartresa, 2019] Chartresa N., et al, (2019) A review of methods used for hazard identification and risk assessment of environmental hazards. Environment

International 123, 231–239

[Chen, FM 2016] Chen FM, Liu X. (2016) Advancing biomaterials of human origin for tissue engineering. Prog Polym Sci.; 53: 86–168.

[Chen, RY, 2014] Chen RY, et al., (2014) PET/CT imaging correlates with treatment outcome in patients with multidrug-resistant tuberculosis. Sci. Transl. Med. 6(265) 265ra166

[Chiu, 2010] Chiu R, et al., (2010) Polymethylmethacrylate particles impair osteoprogenitor viability and expression of osteogenic transcription factors Runx2, osterix, and Dlx5. J Orthop Res. 28(5): 571-577

[Chopra, 2007] Chopra A. (2007) 99mTc-Methyl diphosphonate. Mar 29 [Updated 2009 Aug 24]. In: Molecular Imaging and Contrast Agent Database (MICAD). Bethesda (MD): National Center for Biotechnology Information (US); 2004-2013. Available from: tps://www.ncbi.nlm.nih.gov/books/NBK24575

[Churg, 2008] Churg A, Cosio M, Wright JL. (2008) Mechanisms of cigarette smoke-induced COPD: insights from animal models. Am J Physiol Lung Cell Mol Physiol 294: L612–L631

[Coles, 1995] Coles ME, et al., (1995) The use of attenuation standards for CT scanning. SCA Conference Paper; 9513.

[Cooper, 2002] Cooper EL, Kauschke E, Cossarizza A. (2002) Digging for innate immunity since Darwin and Metchnikoff. BioEssays 4:319–333

[Cortet, 1999] Cortet J, et al. (1999) The use of invertebrate soil fauna in monitoring pollutant effects. Eur J Soil Biol 35:115–134.

[Cotter-Howells, 2005] Cotter-Howells J, et al., (2005) Metal compartmentation and speciation in a soil sentinel: the earthworm, Dendrodrilus rubidus. Environ Sci Technol. 39(19) 7731–7740.)

[Crookes, 1902] Crookes W, Hittorf J. (1902) The New International Encyclopedia 5. Dodd, Mead & Co. 470 p

[Cui, 2018] Cui LB, et al., (2018) Disease Definition for Schizophrenia by Functional Connectivity Using Radiomics Strategy. Schizophrenia Bulletin. (44)5 1053–1059

[Deja, 2014] Deja S. et al., (2014) Metabolomics provide new insights on lung cancer staging and discrimination from chronic obstructive pulmonary disease. J Pharm Biomed Anal. 21;100C:369-380

[Demetriou, 2012] Demetriou CA, et al., (2012) Occup Environ Med. 69:619–627.

[Depeursinge, 2015] Depeursinge, A. et al., (2015) Predicting adenocarcinoma recurrence using computational texture models of nodule components in lung CT. Med. Phys. 42. 2054–2063

[Dewi, 1995] Dewi M. Lewis., (1995) Isotope production and the future potential of accelerators. 14th International Conference on Cyclotrons and their Applications (CYCLOTRONS 95), Faure, Cape Town, South Africa, 8-13 Oct 1995

[Diós, 2015] Diós P. et al, (2015) Preformulation studies and optimization of sodium alginate based floating drug delivery system for eradication of Helicobacter pylori. Eur J Pharm Biopharm. 96.196-206

[Diós, 2016] Diós P. et al., (2016) Influence of barium sulfate X-ray imaging contrast material on properties of floating drug delivery tablets. Eur J Pharm Sci. 95:46-53.

[Dixit, 2015] Dixit R, et al., (2015) Bioremediation of Heavy Metals from Soil and Aquatic Environment: An Overview of Principles and Criteria of Fundamental Processes. Sustainability, 7, 2189-2212

[Dominguez, 2004] Dominguez J. (2004) Earthworm ecology. Boca Raton: CRC Press. 401–424

[Domínguez, 2018] Domínguez, J . (2018) Earthworms and Vermicomposting. Chapter 5. 63-77. publ.2018 http://dx.doi.org/10.5772/intechopen.76088

[Doran, 1994] Doran JW, and Parkin TB (1994) Defining and assessing soil quality. In J. W. Doran, D. C. Coleman, D. F. Bezdicek B. A. Stewart, editors. Defining soil quality for a sustainable environment. Madison, Wisconsin, USA: SSSA, Inc.

[Drewes, 1974] Drewes CD, Pax RA. (1974) Neuromuscular physiology of the longitudinal muscle of the earthworm, Lumbricus terrestris. I. Effects of different physiological salines. J Exp Biol 60:445–452

[Ducy, 2000] Ducy P, et al. (2000) The osteoblast: a sophisticated fibroblast under central surveillance. Science. 289:1501–1504

[Duffy, 2013] Duffy JP and Hubbard RB, (2013) Lung cancer survival in England: trends in non-small-cell lung cancer survival over the duration of the National Lung Cancer Audit British Journal of Cancer. 109, 2058–2065

[EFSA, 2009] EFSA, (2009) Press release 20 March. EFSA sets lower tolerable intake level for cadmium in food (http://www.efsa.europa. eu/EFSA/efsa_locale-1178620753812_1211902396263.htm; accessed 23, 03. 2009.

[Elinder, 1992] Elinder CG. (1992) Cadmium as an environmental hazard. IARC Sci Publ.; (118):123-32.

[Ellender, 1988] Ellender, G, Feik, A, Carach, B.J (1988) Periosteal structure and development in a rat caudal vertebra. J. Anat. 158, pp. 173-187

[EPA, 1996] EPA, (1996) Oxidant Air Pollutants and Lung Cancer: An Animal Model. Available: http://cfpub.epa.gov/ncer_abstracts/index.cfm/fuseaction/display.abstractDetail/abstract/2323 [accessed 11. 12. 2014]

[European Commission, 2006] European Commission. (2006) Communication from the Commission to the Council, the European Parliament, the European Economic and Social Committee and the Committee of the regions: thematic strategy for soil protection. COM 231. Last accessed 04/04/2007: http://ec.europa.eu/environment/soil

[Faroon, 2012] Faroon O, et al., (2012) Toxicological profile for cadmium U.S. Department of Health and Human Services Public Health Service Agency for

Toxic Substances and Disease Registry September

[Fasella, 1963] Fasella P, Gordon G. H. (1963) Studies of the enzyme hexokinase. IV. The role of sulfhydryl groups. Archives of Biochemistry and Biophysics. (100)2. 295–297

[Fazzalari, 1996] Fazzalari NL and Parkinson IH. (1996) Fractal dimension and architecture of trabecular bone. The Journal of Pathology. 178: 100–05

[Feeman, 2010a] Feeman TG., (2010a) The Mathematics of Medical Imaging: A Beginner's Guide. New York: Springer-Verlag;

[Feeman, 2010b] Feeman TG. (2010b) The Mathematics of Medical Imaging: A Beginner's Guide. Springer Undergraduate Texts in Mathematics and Technology. Springer.

[Ferlay, 2012] Ferlay, J, ed. (2012) GLOBOCAN 2012: Estimated Cancer Incidence, Mortality and Prevalence Worldwide in 2012 v1.0, IARC CancerBase No. 11, ISBN-13 (Database), 978-92-832-2447-1

[Fitzgerald, 1983] Fitzgerald TA. (1983) Comparison of research cost: man--primate animal--other animal models, Journal of medical primatology; 12:138-45

[Fogelman, 1978] Fogelman I, et al. (1978) The use of whole-body retention of Tc-99m diphosphonate in the diagnosis of metabolic bone disease. J Nucl Med.; 19(3): 270-275.

[Forrer, 2006] Forrer F, et al., (2006) In vivo radionuclide uptake quantification using a multi-pinhole SPECT system to predict renal function in small animals. Eur J Nucl Med Mol Imaging. (10) 1214-1217

[Freedman, 1981] Freedman D, Diaconis P. (1981) On the histogram as a density estimator: L2 theory. Zeitschrift für Wahrscheinlichkeitstheorie und Verwandte Gebiete. ;57:453–76

[Friberg, 1986] Friberg L, et al., (1986) Handbook of the toxicology of metals. Vol. II. Amsterdam, Elsevier, pp. 130–184.

[Fuller-Espie, 2011] Fuller-Espie SL, Bearoff FM, Minutillo MA. (2011) Exposure of coelomocytes from the earthworm *Eisenia hortensis* to Cu, Cd, and dimethylbenz[a]anthracene: An *in vitro* study examining reactive oxygen species production and immune response inhibition. Pedobiologia 54S. S31–S36

[Galal-Gorchev, 1991] Galal-Gorchev H. (1991) Dietary intake of pesticide residues, cadmium, mercury and lead. Food Additives and Contaminants, 8:793–806.

[Galay-Burgos, 2003] Galay-Burgos M, et al., (2003) Developing a new method for soil pollution monitoring using molecular genetic markers. Biomarkers 8, 229–239

[Galloway, 1975] Galloway MM. (1975) Texture analysis using gray level run lengths. Comput Graphics Image Process. 4:172–179

[GBD, 2016] GBD (2016) Disease and Injury Incidence and Prevalence Collaborators. Global, regional, and national incidence, prevalence, and years lived with disability for 328 diseases and injuries for 195 countries, 1990–2016:

a systematic analysis for the Global Burden of Disease Study Lancet 2017; 390: 1211–59

[Gelb, 1994] Gelb H, et al., (1994) In vivo inflammatory response to polymethylmethacrylate particulate debris: effect of size, morphology, and surface area. J. Orthop Res. 12(1):83-92

[Genant, 1974] Genant HK, et al., (1974) Bone-seeking radionuclides: an in vivo study of factors affecting skeletal uptake. Radiology. Nov;113(2):373–382.

[Gerencsér, 2010] Gerencsér G, et al. (2010) Ecotoxicological studies on Hungarian peloids (medicinal muds). Appl Clay Sci 50:47–50

[Gergely, 2012] Gergely P, et al., (2012) Kinase inhibitors reduce 7,12-dimethylbenz[a]anthracene-induced oncosuppressor gene expression in short-term experiments. Eur. J. Oncol (17)1, 11-21.

[Ghissassi, 2009] Ghissassi FE, et al., (2009) A review of human carcinogens—Part D: radiation. 8(10)751-752

[Gillies,.2016] Gillies RJ. et al., (2016) Radiomics: Images Are More than Pictures, They Are Data. Radiology; 278:563–577

[Gobas, 1993] Gobas F.A.P.C., Zhang X., Wells R., (1993) Gastrointestinal Magnification: The Mechanism of Biomagnification and Food Chain Accumulation of Organic Chemicals. Environ. Sci. Technol. 27, 2855-2863

[Goffin, 2009] Goffin J, et al., (2009) Lung Cancer Disease Site Group of Cancer Care Ontario’s Program in Evidence-Based Care: First-line systemic chemotherapy in the treatment of advanced nonsmall cell lung cancer: a systematic review. 2010. J Thorac Oncol 5, 260–274. ; Jemal A, Siegel R,Ward E, Hao Y, Xu J, et al.: Cancer statistics, 2009. CA Cancer J Clin 59, 225–249

[Goldring, 1986] Goldring SR, (1986) Formation of a synovial-like membrane at the bonecement interface: Its role in bone resorption and implant loosening after total hip replacement. Arthritis Rheum. 29(7):836e842

[Grove, 2015] Grove, O. et al., (2015) Quantitative computed tomographic descriptors associate tumor shape complexity and intratumor heterogeneity with prognosis in lung adenocarcinoma, PLoS ONE 10 (3) e0118261.

[Guimarães, 2019] Guimarães B, Römbke J, Amorim MJB. (2019) Novel egg life-stage test with Folsomia candida - A case study with Cadmium (Cd). Sci Total Environ. 10;647:121-126

[Guvenç, 2003] Guvenç, N, et al., (2003) Investigation of soil multi-element composition in Antalya, Turkey Environment International. (29)5. 631–640.

[Gyöngyi, 2013] Gyöngyi Z, (2013) Deuterium Depleted Water Effects on Survival of Lung Cancer Patients and Expression of Kras, Bcl2, and Myc Genes in Mouse Lung. Nutrition and Cancer. 65(2) 240-246

[Hahn, 1950] Hahn, E. L. (1950) Spin Echoes. Phys. Rev. 80, 580

[Hammond, 1970] Hammond and Storey, (1970) Measurement of growth and resorption of bone in rats fed meat diet. Calcified Tissue Research 4, 291-304

[Haralick, 1973] Haralick RM, Shanmugam K, Dinstein I. (1973) Textural Features for Image Classification. IEEE Transactions on Systems, Man, and Cybernetics. SMC-3(6) 610–621

[Hartung, 2010] Hartung T. (2010) Comparative analysis of the revised Directive 2010/63/EU for the protection of laboratory animals with its predecessor 86/609/EEC - a t4 report. ALTEX.; 27(4): 285-303

[Hassett, 2014] Hassett DJ, Borchers MT, Panos RJ., (2014) Chronic obstructive pulmonary disease (COPD): evaluation from clinical, immunological and bacterial pathogenesis perspectives. J Microbiol. 52: 211-26

[Helmberger, 2014] Helmberger M, et al., (2014) Quantification of tortuosity and fractal dimension of the lung vessels in pulmonary hypertension patients. PLoS One. 9(1):e87515

[Hinck, 2004] Hinck L. (2004) The versatile roles of "axon guidance" cues in tissue morphogenesis. Dev Cell. 7: 783–793

[Hirano, 2010] Hirano T. and Tamae K., (2010) Heavy Metal-Induced Oxidative DNA Damage in Earthworms: A Review Applied and Environmental Soil Science Volume, Article ID 726946, 7 pages

[Hirt, 2003] Heribert Hirt and Kazuo Shinozaki, (2003) Plant Responses to Abiotic Stress. Springer Science & Business Media, okt. 8. Springer Verlag Berlin-Heidelberg 2004

[Hoek, 1990] Hoek JB, Rubin E. (1990) Alcohol and membrane-associated signal transduction. Alcohol Alcohol 2-3:143–156

[Homa, 2007] Homa J, et al., (2007) Disrupted homeostasis in coelomocytes of *Eisenia fetida* and *Allolobophora chlorotica* exposed dermally to heavy metals. *Eur J Soil Biol.*; 43(S1):273-280

[Homa, 2010] Homa, J., et al., (2010) Metal-specific effects on metallothionein gene induction and riboflavin content in coelomocytes of the stubby earthworm Allolobophora chlorotica exposed dermally to metal chlorides. Ecotoxicol. Environ. Saf. 73, 1937–1943.

[Homa, 2013] Homa J, et al., (2013) Dermal exposure to immunostimulants induces changes in activity and proliferation of coelomocytes of Eisenia andrei. J Comp Physiol B 183:313–322

[Horowitz, 2009] Horowitz A, Simons M. (2009) Branching morphogenesis. Circ Res. 104: 784-795. ; Hinck L. The versatile roles of "axon guidance" cues in tissue morphogenesis. 2004. Dev Cell. 7: 783–793

[Hu, 1995] Hu T, Sung H,. Keeler TE, (1995) Reducing cigarette consumption in California: tobacco taxes vs. an anti-smoking media campaign. Am J Public Health, 85:1218-1222

[Hutton, 2014] Hutton BF. (2014) The origins of SPECT and SPECT/CT. Eur J Nucl Med Mol Imaging. 41 Suppl 1:S3-16.

[Järup, 2003] Järup, L, (2003) Hazards of heavy metal contamination. British Medical Bulletin. (68). 167–182

[Järup, 2009] Järup L, Åkesson A. (2009) Current status of cadmium as an environmental health problem. Toxicology and Applied Pharmacology. 238. 201–208

[JECFA, 1989] JECFA, (1989) Toxicological evaluation of certain food additives and contaminants. Geneva, World Health Organization, Joint FAO/WHO Expert Committee on Food Additives; Cambridge, Cambridge University Press, pp. 163–219 (WHO Food Additives Series No. 24)

[Jeffery, 1998.] Jeffery PK., (1998) Structural and inflammatory changes in COPD: a comparison with asthma. Thorax. 53. 129-36.

[Jensen, 1992] Jensen, A., and Bro-Rasmussen, F. (1992) Environmental Contamination in Europe. Reviews of Environmental Contamination and Toxicology. (125) 101-181

[Jeyabalan, 2012] Jeyabalan A. (2012) Particulate allergens aggravate allergic asthma in mice. Thorax 67: 25

[Jing, 2003] Jing ZL, Lu DZ and Guang HY. (2003) Fractal Dimension in Human Cerebellum Measured by Magnetic Resonance Imaging. Biophysical Journal. 85: 4041-46.

[Jobse, 2011] Jobse BN, et al. (2011) Detection of Lung Dysfunction Using Ventilation and Perfusion SPECT in a Mouse Model of Chronic Cigarette Smoke Exposure. J Nucl Med 54: 616-623

[Jobse, 2012] Jobse BN, et al., (2012) Imaging lung function in mice using SPECT/CT and per-voxel analysis. PLoS One. 8: 1-17.

[Kakei, 2013] Kakei M, Sakae T, and Yoshikawa M. (2013) Combined effects of estrogen deficiency and cadmium exposure on calcified hard tissues: Animal model relating to itai-itai disease in postmenopausal women. Proc. Jpn. Acad., Ser. B 89

[Kanis, 2005] Kanis JA, et al., (2005) Smoking and fracture risk: a meta-analysis. Osteoporos Int. 16(2) 155-162

[Kanishi, 1993] Kanishi D. (1993) 99mTc-MDP accumulation mechanisms in bone. Or Surg Or Med Or P. 1993;75(2): 239-246.

[Keay, 2012] Keay J, Thornton JW. (2012) Hormone-activated estrogen receptors in annelid invertebrates: implications for evolution and endocrine disruption. Endocrinology 150:1731–1738

[Khakwani, 2013] Khakwani, A. et al. (2013) Lung cancer survival in England: trends in non-small-cell lung cancer survival over the duration of the National Lung Cancer Audit. British Journal of Cancer 109: 2058–2065.)

[Khan, 2000] Khan SN, Bostrom MP, Lane JM., (2000) Bone growth factors. Orthop Clin North Am. 31(3):375-88

[Kibblewhite, 2008] Kibblewhite MG, et al. (2008) Soil health in agricultural systems. Phil Trans R Soc B 363:685–701

[Kim, 1997] Kim WD. (1997) Lung mucus: a clinician's view. Eur Respir J. 10: 1914–1917.

[Koblinger, 1985] Koblinger L and Hofmann W. (198)5 Analysis of human lung morphometric data for stochastic aerosol deposition calculations. Phys Med Biol. 30: 541-556.

[Koch, 1956] Koch HJ. et al., (1956) Analysis of trace elements in human tissues. I. Normal Tissues. Cancer. 9;499-511

[Kode, 2017] Kode V, et al., (2017) Impact of Renal Failure on F18-FDG PET/CT Scans. Front Oncol. 7 155

[Kolossváry, 2017] Kolossváry M, et al., (2017) Radiomic Features Are Superior to Conventional Quantitative Computed Tomographic Metrics to Identify Coronary Plaques With Napkin-Ring Sign. Circ Cardiovasc Imaging. 10(12). pii: e006843.)

[Kolossváry, 2018] Kolossváry M. et al., (2018) Cardiac Computed Tomography Radiomics: A Comprehensive Review on Radiomic Techniques. J Thorac Imaging. 33(1):26-34

[Környei, 1997] Környei J., (1997) A nukleáris medicina fizikai, kémiai alapjai. Bevezetés az in vivo izotópalkalmazásba.] [Book in hungrian.] Kossuth Egyetemi Kiadó, Debrecen

[Kossmann, 2017] Kossmann CM., et al. (2017) ADAM9 expression promotes an aggressive lung adenocarcinoma phenotype. Tumour Biol. 39(7):1010428317716077

[Kumar, 2012] Kumar V, et al. (2012) Radiomics: the process and the challenges. Magn Reson Imaging. Nov;30(9):1234-48

[Kurth, 2001] Kurth AA and Müller R. (2001) The effect of an osteolytic tumor on the three-dimensional trabecular bone morphology in an animal model. Skeletal Radiol. 30(2) 94-98.

[Lahnstein, 2008] Lahnstein K, et al, (2008) Pulmonary absorption of aerosolized fluorescent markers in the isolated rabbit lung. 2008. Int J Pharm. 351: 158-64

[Larison, 2000] Larison JR, et al,. (2000) Cadmium toxicity among wildlife in the Colorado Rocky Mountains. Nature (6792)406 1181-183)

[Larkin, 2014] Larkin TJ, et al. (2014) Analysis of image heterogeneity using 2D Minkowski functionals detects tumor responses to treatment. Magn Reson Med. 71 402-410

[Łaszczyca, 2004] Łaszczyca P, et al. (2004) Profiles of enzymatic activity in earthworms from zinc, lead and cadmium polluted areas near Olkusz (Poland). Environ Int 7:901-910

[Lauber, 2017] Lauber DT, et al, (2017) State of the art in vivo imaging techniques for laboratory animals. Lab Anim. 51(5):465-478.

[Lavelle, 2006] Lavelle P, et al. (2006) Soil invertebrates and ecosystem services. European J Soil Biology 42:S3–S15.

[Law, 1997] Law MR, Hackshaw AK. (1997) A meta-analysis of cigarette smoking, bone mineral density and risk of hip fracture; recognition of a major effect. Br Med J 315. 841–846.

[Lawrence, 1947] Lawrence JH et al., (1947) Radioactive phosphorus, P-32: a six-year clinical evaluation of internal radiation therapy. J Lab Clin Med. 32, 943-969

[Lee, 2006] Lee SH et al., (2006) Heme oxygenase 1 mediates anti-inflammatory effects of 2',4',6'-tris(methoxymethoxy) chalcone. Eur J Pharmacol. 532(1-2):178-186

[Legoza, 2010] Legoza J. (2010) Modern képalkotó diagnosztika és sugáregészségügy. Article in hungarian. Egészségtudomány. 2010. (2) 17-27.

[Leveque, 2013] Leveque T, et al. (2013) Assessing ecotoxicity and uptake of metals and metalloids in relation to two different earthworm species (Eiseina hortensis and Lumbricus terrestris). Environ Pollut 179:232–241.

[Lewis, 2009] Lewis G, et al., (2009) A room-temperature autonomically-healing PMMA bone cement: influence of composition on fatigue crack propagation rate. J Appl Biomater Biom. 7(2): 90-96

[Li, 2013] Li N et al., (2013) Therapeutic potentials of naringin on polymethylmethacrylate induced osteoclastogenesis and osteolysis, in vitro and in vivo assessments. Drug Des Devel Ther. 8:1-11

[Linn, W, 1987] Linn, W, et al (1987) Replicated dose-response study of 11 sulfur dioxide effects in normal, atopic, and asthmatic volunteers. American Review of 12 Respiratory Disease. 136:1127-1134.

[Liu, H, 2009] Liu H. (2009) The Effect of Anti-Smoking Media Campaign on Smoking Behavior: The California Experience. ANNALS OF ECONOMICS AND FINANCE 10-1, 29–47

[Liu, X, 2016] Liu X, et al., (2016) Cadmium (Cd) distribution and contamination in Chinese paddy soils on national scale. Environ Sci Pollut Res. 23. 17941

[Loi, 2016] Loi F, et al., (2016) Inflammation, Fracture and Bone Repair. Bone. 86: 119–130

[Lopez, 2006] Lopez AD, et al., (2006) Chronic obstructive pulmonary disease: Current burden and future projections. Eur Respir J 27: 397–412.

[Love, 2003] Love C, et al., (2003) Radionuclide Bone Imaging: An Illustrative Review. RadioGraphics. 23:341–358.

[Lucas, 2013] Lucas SD, et al., (2013) Targeting COPD: advances on low-molecular-weight inhibitors of human neutrophil elastase. Med Res Rev. 33 Suppl 1:E73-101

[MacNeill, 1999] MacNeill SR, et al., (1999) In vivo comparison of synthetic osseous graft materials. A preliminary study. J Clin Periodontol. 26. 239–245.)

[Madsen, 2012] Madsen JL, et al., (2012) Synthesis and evaluation of silanediols as highly selective uncompetitive inhibitors of human neutrophil elastase. J Med Chem. 13. 55(17). 7900-7908

[Maeno, 2007] Maeno T, et al., (2007) CD8+ T Cells are required for inflammation and destruction in cigarette smoke-induced emphysema in mice. J Immunol. 178(12):8090-6.

[Maki, 1999] Maki DD. et al., (1999) Recent advances in pulmonary imaging. Chest. 116(5):1388-1402

[Mandelbrot, 1967] Mandelbrot B. (1967) How long is the coast of Britain? Statistical self-similarity and fractional dimension. Science.156:636–638.

[Mandelbrot, 1989] Mandelbrot BB. (1989) Fractal geometry: what is it, and what does it do? Proc.R.Soc.Land. A 423, 3-16

[Maneesh, 2018] Maneesh D, et al, (2018) Sa1987 - small Intestinal MRI Pathology Inflammation Score (Simple) Predicts Disease Severity and Response to Therapy in Experimental Crohn's Disease (CD). Gastroenterology. (154)6 S-438)

[Mannino, 2007] Mannino DM and Buist AS., (2007) Global burden of COPD: risk factors, prevalence, and future trends. Lancet; 370: 765–73;

[Marsenic, 2009] Marsenic O., (2009) Glucose control by the kidney: an emerging target in diabetes. Am J Kidney Disease. 53(5):875-883

[Martelli, 2006] Martelli A, et al., (2006) Cadmium toxicity in animal cells by interference with essential metals. Biochimie. 2006. 88(11):1807-14

[Massari, 2019] Massari L, et al. (2019) Biophysical stimulation of bone and cartilage: state of the art and future perspectives. Int Orthop. doi: 10.1007/s00264-018-4274-3. [Epub ahead of print]

[Máthé, 2015] Máthé D., et al, (2015) Early X-ray CT radiomic identification of lung tissue harm origins in mice

EANM, Hamburg, Germany, 10. 10-14.

[Mazur, 2011] Mazur AI, et al., (2011) Riboflavin storage in earthworm chloragocytes and chloragocyte-derived eleocytes and its putative role as chemoattractant for immunocompetent cells. Pedobiologia. 54S. S37– S42

[McIntyre, 2003] McIntyre, T., (2003) Phytoremediation of heavy metals from soils. Advances in Biochemical Engineering/Biotechnology. (78) 97–123

[McNeill, 2006] McNeill A, et al., (2006) Levels of toxins in oral_tobacco products_ in the UK. Tob Control. 15(1): 64-7.

[Minkowski, 1903] Minkowski H. (1903) Volumen und Oberfläche. Math Ann. 57 447–495

[Moldoveanu, 2009] Moldoveanu B, et al., 2009) Inflammatory mechanisms in the lung. J Inflamm Res. 2: 1–11.

[Molnár, 2012] Molnár L, et al., (2012) Coldstress induced formation of calcium and phosphorous rich chloragocyte granules (chloragosomes) in the earthworm Eisenia fetida. Comp Biochem Physiol A Mol Integr Physiol. 163(2) 199–209

[Morgan, 2002] Morgan AJ, Turner MP, Morgan JE. (2002) Morphological plasticity in metal-sequestering earthworm chloragocytes: morphometric electron microscopy provides a biomarker of exposure in field populations. Environ Toxicol Chem. 21(3) 610–618

[Morvan, 2008] Morvan X, et al. (2008) Soil monitoring in Europe: a review of existing systems and requirements for harmonisation. Sci Total Environ 391:1–12

[Muralikrishna, 2017] Muralikrishna IV, and Manickam V. (2017) Introduction. Environmental Management, 1–4.doi:10.1016/b978-0-12-811989-1.00001-4

[Nagao, 2001] Nagao M, et al., (2001) Fractal Analysis of Cerebral Blood Flow Distribution in Alzheimer's Disease. The Journal of Nuclear Medicine. 42: 1446-50.

[Nagao, 2002] Nagao M, Murase K. (2002) Measurement of heterogeneous distribution on Technegas SPECT images by three-dimensional fractal analysis. Annals of Nuclear Medicine. 16: 369-376.

[NCHS, 1999] National Center for Health Statistics (US), (1999) Total deaths for each cause by 5-year age groups. Hyattsville (MD): U.S. Department of Health and Human Services

[Nomiyama, 1982] Nomiyama, K., et al., (1982) Cadmium health effects in monkeys with special reference to the critical concentration of cadmium in the renal cortex. In: Cadmium 81, (Proceedings Third International Cadmium Conference, Miami), Metal Bulletin Ltd., London, 151-156

[Nordberg, 1984] Nordberg M. (1984) General aspects of cadmium: transport, uptake and metabolism by the kidney. Environ Health Perspect. 54:13-20

[Nordberg, 2012] Nordberg G, et al., (2012) Kidney dysfunction and cadmium exposure – factors influencing dose–response relationships. J Trace Elem Med Biol. 26:197–200. ;

[Novais, 2011] Novais SC, et al, (2011) Reproduction and biochemical responses in Enchytraeus albidus (Oligochaeta) to zinc or cadmium exposures. Environmental Pollution. 159. 1836-1843.

[Nunamaker, 1998] Nunamaker, DM. (1998) Experimental Models of Fracture Repair. CLINICAL ORTHOPAEDICS AND RELATED RESEARCH Number 355S, pp S56-S65. 1998. S57

[OECD, 1984] OECD, (1984) OECD guideline for testing chemicals. Section 2: effects on biotic systems. Method, 207. Earthworm, acute toxicity tests. Paris, France,

[OECD, 2009] OECD, (2009) Organisation for Economic Co-Operation and Development. Guidel. Test. Chem. No 232. Collembolan Reprod. Test Soil. https://doi.org/10.1787/9789264076273-en

[Opper, 2010] Opper B, Németh P, Engelmann P. (2010) Calcium is required for coelomocyte activation in earthworms. Mol Immunol. 11–12:2047–2056.

[Otsu, 1979] Otsu N. (1979) A threshold selection method from gray-level histograms. IEEE Trans. Sys., Man., Cyber. 9(1) 62–66.

[Panagos, 2013] Panagos P, et al., (2013) Contaminated Sites in Europe: Review of the Current Situation Based on Data Collected through a European Network. Journal of Environmental and Public Health Volume, Article ID 158764, 11 pages

[Pant, 2003] Pant N. et al, (2003) Lead and cadmium concentration in the seminal plasma of men in the general population: correlation with sperm quality. Reprod Toxicol. 17(4):447-50

[Pauwels, 2001] Pauwels RA, et al., (2001) Global strategy for the diagnosis, management, and prevention of chronic obstructive pulmonary disease. NHLBI/WHO Global Initiative for Chronic Obstructive Lung Disease (GOLD) Workshop summary. Am J Respir Crit Care Med.; 163: 1256-76

[Peller, 1993] Peller PJ, Ho VB, Kransdorf MJ. (1993) Extraosseous Tc-99m MDP uptake: a pathophysiologic approach. Radiographics. 13(4) 715-734

[Perjési P, 2000] Perjési P, et al. (2000) Effect of E-2-(4'-methoxybenzylidene)-1-benzosuberone on the 7,12 dimethylbenz[alpha]anthracene-induced onco/suppressor gene action in vivo II: A 48-hour experiment. Anticancer Res. 20(3A):1839-1848

[Perrin, 2012] Perrin, A. and Souques, M. (2012) Electromagnetic Fields, Environment and Health, Chapter 2. MRI and Static Electric and Magnetic Fields. DOI: 10.1007/978-2-8178-0363-0_2, Springer-Verlag France

[Perry, 1976] Perry HM et al., (1976) The biology of cadmium. Med Clin North Am. 60(4):759-769

[Petrics, 1986] Petrics GB, Larsson LI. (1986) Enkephalins may act as sensory transmitters in earthworms. Cell Tissue Res 1:33–37

[Petrou, 2006a] Petrou M, Sevilla PG. (2006a) Image processing: dealing with texture. Chichester, England: John Wiley & Sons Ltd. 634

[Petrou, 2006b] Petrou M, Sevilla PG. (2006b) Image Processing: Dealing With Texture. New York: Wiley

[Pienn, 2014] Pienn M, et al., (2014) Non-invasive determination of pulmonary hypertension with dynamic contrast-enhanced computed tomography: a pilot study. European Radiology. (24)3. 668-676.

[Pinkus, 1977] Pinkus LM, et al., (1977) The glutathione S-transferases as a possible detoxification system of rat intestinal epithelium. Biochem Pharmacol. 26(24):2359-2363

[Plytycz, 2011] Plytycz B, et al., (2011) Species-specific sensitivity of earthworm coelomocytes to dermal metal (Cd, Cu, Ni, Pb, Zn) exposures: Methodological approach. Pedobiologia 54S S203– S210

[Popovic, 2001] Popovic JR. (2001) National Hospital Discharge Survey: 1999 National Hospital Discharge Survey: annual summary with detailed diagnosis and procedure data. Vital Health Stat. 13(151):i–v . 1–206

[Prento, 1987] Prento P. (1987) Blood sugar, sugar metabolism and related enzymes in the earthworm, Lumbricus terrestris L. Comp. Biochem. PhysioL. (86B)2, 333-341

[Prokop, 2003] Prokop M, Galanski M and Schaefer-Prokop C (2003) Spiral and Multislice Computed Tomography of the Body (Thieme Medical Publisher) (available at: http://books.google.nl/books?id=K9GbaGpOdGwC)

[Prüss-Üstün, 2016] Prüss-Üstün, A., et al., (2016) Preventing disease through healthy environments: a global assessment of the burden of disease from environmental risks. World Health Organization

[Puetzer, 2010] Puetzer JL, Petitte JN, Loboa EG, (2010) Comparative Review of Growth Factors for Induction of Three-Dimensional In Vitro Chondrogenesis in Human Mesenchymal Stem Cells Isolated from Bone Marrow and Adipose Tissue. Tissue Engineering Part B: Reviews; (16)4. 435-440.

[Purisha, 2019] Purisha, Z, (2019) An Automatic Regularization Method: An Application for 3-D X-Ray Micro-CT Reconstruction Using Sparse Data. 2019. IEEE TRANSACTIONS ON MEDICAL IMAGING, (38)2. 417-425.

[Rahmim, 2017] Rahmim A, et al., (2017) Improved prediction of outcome in Parkinson's disease using radiomics analysis of longitudinal DAT SPECT images. Neuroimage Clin. 26;16:539-544.

[Ramseier, 1989] Ramseier, S. et al., (1989) Bioaccumulation of cadmium by Lumbricus terrestris. Toxicological & Environmental Chemistry, 22:1-4, 189-196

[Rao, 2003] Rao JV, Kavitha P, Rao AP. (2003) Comparative toxicity of tetraethyl lead and lead oxide to earthworms, Eisenia fetida (Savigny). Environ Res 92:271–276

[Rao, 2004] Rao JV, Kavitha P. (2004) Toxicity of azodrin on the morphology and acetylcholinesterase activity of the earthworm Eisenia foetida. Environ Res 96:323–327

[Rea, 2018] Rea WJ, et al., (2018) Reversibility of Chronic Disease and Hypersensitivity, Volume 4: The environmental aspects of chemical sensitivity. Chapter 4: Inorganic Chemical Pollutants, Cadmium. CRC Press Taylor & Francis Group

[Reagan-Shaw, 2007] Reagan-Shaw S, Nihal M, Ahmad N. (2007) Dose translation from animal to human studies revisited. FASEB J 3:659–661

[Renaud, 2016] Renaud M, et al., (2016) A new rat model for translational research in bone regeneration. Tissue Eng Part C Meth.; 2 doi: 10.1089/ten.TEC.2015.0187

[Ricketts, 2004] Ricketts HJ, et al., (2004) Measurement of annetocin gene expression: a new reproductive biomarker in earthworm ecotoxicology. Ecotoxicol Environ Saf 1:4–10.

[Robertson, 2013] Robertson A, et al., (2013) The Cellular and Molecular Carcinogenic Effects of Radon. Exposure: A Review.Int. J. Mol. Sci. 14. 14024-14063

[Roh, 2006] Roh JY, Lee J, Choi J. (2006) Assessment of stress-related gene expression in the heavy metal-exposed nematode Caenorhabditis elegans: a potential biomarker for metal-induced toxicity monitoring and environmental risk assessment. Environ Toxicol Chem. 25:2946–2956

[Rohrbach, 2002] Rohrbach LA, et al., (2002) Independent Evaluation of the California Tobacco Control Program: Relationships Between Program Exposure and Outcomes, 1996–1998. Am J Public Health. 92(6): 975–984

[Röntgen, 1895] Röntgen, WC, (1895) On a new kind of rays. Sitzgsber. Physik-Med. Ges., Würzburg 137 p. ; Röntgen, WC.: Ann. Phys. Chem. N.F. 1898. 64, 1.

[Ros, 1987] Ros JPM and Slooff W., (1987) Integrated criteria document. Cadmium. Bilthoven, National Institute of Public Health and Environmental Protection (Report No. 758476004)

[Rozendorn, 2018] Rozendorn N, et al., (2018) A review of magnetic resonance enterography-based indices for quantification of Crohn's disease inflammation. Therap Adv Gastroenterol. 11: 1756284818765956

[Ruchita, 2015] Ruchita D, et al., (2015) Bioremediation of Heavy Metals from Soil and Aquatic Environment: An Overview of Principles and Criteria of Fundamental Processes.Sustainability, 7, 2189-2212

[Ruiz, 2011] Ruiz N, et al. (2011) IBQS: a synthetic index of soil quality based on soil macro-invertebrate communities. Soil Biol Biochem 43:2032–2045.

[Saint-Denis, 1999] Saint-Denis M et al., (1999) Biochemical responses of the earthworm Eisenia fetida andrei exposed to contaminated artificial soil: effects of benzo(a)pyrene. Soil Biology & Biochemistry 31, 1837e1846.

[Sasaki, 2018] Sasaki M, et al., (2018) Effects of long-term cigarette smoke exposure on bone metabolism, structure, and quality in a mouse model of emphysema. PLoS One. 13(1):e0191611. doi: 10.1371/journal.pone.0191611. eCollection 2018

[Sauvé, 2002] Sauvé S, et al., (2002) Phagocytic activity of marine and freshwater bivalves: in vitro exposure of hemocytes to metals (Ag, Cd, Hg, and Zn). Aquatic Toxicol. 58(3-4):189-200

[Scaps, 1997] Scaps P., Grelle C., Descamps M. (1997) Cadmium and Lead Accumulation in the Earthworm Eisenia fetida (Savigny) and its Impact on Cholinesterase and Metabolic Pathway Enzyme Activity. Comp biochem physiol 116C;3:233–238.

[Schroeder, 1963] Schroeder HA, Balassa JJ. (1963) Cadmium: uptake by vegetables from superphosphate in soil. Science. 140(3568) 819-820

[Shaker, 2011] Shaker SB, et al. (2011) Rapid fall in lung density following smoking cessation in COPD. 2011. COPD. 8: 2-7

[Sheikh, 2013] Sheikh ZA, Javaid A, Abdallah MA. (2013) Bone replacement graft materials in dentistry. In: Khurshid Z, Zafar SZ, editor. Dental biomaterials (Principle and its Application). 2nd ed: Paramount Publishing Enterprise: Karachi, Pakistan

[Sheikh, 2017] Sheikh ZA, et al., (2017) Natural graft tissues and synthetic biomaterials for periodontal and alveolar bone reconstructive applications: a review. Biomater Res. 21: 9.

[Shlesinger, 1991] Shlesinger MF and West BJ. (1991) Complex fractal dimension of the bronchial tree. Phys Rev Lett. 67: 2106-08

[Shyamasree, 2017] Shyamasree Ghosh, (2017) Environmental pollutants, pathogens and immune system in earthworms. Environmental Science and Pollution Research. https://doi.org/10.1007/s11356-017-1167-8

[Smith, 1996] Smith Jr. TG, Lange GD, Marks WB. (1996) Fractal methods and results in cellular morphology — dimensions, lacunarity and multifractals. Journal of Neuroscience Methods. 69: 123-136

[Sookpeng, 2016] Sookpeng S, et al., (2016) Comparison of computed tomography dose index in polymethyl methacrylate and nylon dosimetry phantoms. J Med Phys. 41(1): 45–51.

[Sousa, 2006] Sousa JP, et al. (2006) Changes in Collembola richness and diversity along a gradient of land-use intensity: a pan European study. Pedobiologia 50:147–156

[Spurgeon, 1996] Spurgeon DJ, and Hopkin SP. (1996) Effects of metal-contaminated soils on the growth, sexual development, and early cocoon production of the earthworm Eisenia fetida, with particular reference to zinc. Ecotoxicol Environ Saf 1:86–95

[Spurgeon, 1999] Spurgeon DJ, Hopkin SP. (1999) Tolerance to zinc in populations of the earthworms Lumbricus rubellus from uncontaminated and metal contaminated ecosystems. Arch Environ Contam Toxicol 3:332–337

[Storey, 1972] Storey, E. (1972) Growth and remodelling of bone and bones. American Journal of Orthodontics 62, 142-165.Storey,

[Studwell, 2011] Studwell AJ and Kotton DN. (2011) A Shift From Cell Cultures to Creatures: In Vivo Imaging of Small Animals in Experimental Regenerative Medicine. Mol Ther. 19(11) 1933–1941

[Stürzenbaum, 2001] Stürzenbaum, S. R., et al., (2001) Metal Ion Trafficking in Earthworms. Journal of Biological Chemistry, 276(36), 34013–34018.

[Suzuki, 1980] Suzuki K.T., Yamamura M., Mori T. (1980) Metabolic Fate of Earthworm Cadmium-binding Proteins in Rats. Arch. Environm. Contain. Toxicol. 9, 519-531

[Szigeti, 2016] Szigeti K, et al., (2016) Radiomics-based differentiation of lung disease models generated by polluted air based on X-ray computed tomography data. BMC Medical Imaging 16(1)14. doi: 10.1186/s12880-016-0118-z

[Szigeti, 2018] Szigeti K, et al., (2018) Thallium labelled citrate coated Prussian blue nanoparticles as potential imaging agent. Contrast Media & Molecular Imaging. Volume 2018 Article ID 2023604, 10 pages https://doi.org/10.1155/2018/2023604

[Tager, 1999] Tager I et al., (1999) Air pollution and lung function growth: is it ozone? Am J Respir Crit Care Med, 160:387.

[Takács S, 2018] Takács S., (2018) Microelements: medicinesor toxins? [Mikroelemek: gyógyszerek vagy mérgek?] Article in Hungarian. [Egészségtudomány] Health Science. 62(1-2) 29-38.

[Takacs V., 2016] Takacs V, (2016) Exposure of *Eisenia andrei* (Oligochaeta;

Lumbricidea) to Cadmium Polluted Soil Inhibits Earthworm Maturation and Reproduction but not Restoration of Experimentally Depleted Coelomocytes or Regeneration of Amputated Segments. Folia Biol (Krakow). 64(4) 275-284

[Tang, 2017] Tang R., et al., (2017) Time-dependent responses of earthworms to soil contaminated with low levels of lead as detected using $_1$H NMR metabolomics. RSC Adv., 7, 34170.

[Thawania, 2018] Thawania R, et al., (2018) Radiomics and radiogenomics in lung cancer: A review for the clinician. Lung Cancer.; 115:34-41

[Thoren, 1995] Thoren K, Aspenberg P, Thorngren KG. (1995) Lipid extracted bank bone. Bone conductive and mechanical properties. Clin Orthop Relat R. 311: 232-246

[Tokumoto, 2011] Tokumoto M, et al., (2011) Cadmium toxicity is caused by accumulation of p53 through the down regulation of Ube2d family genes in vitro and in vivo. J Toxicol Sci. 36(2):191-200

[Toriihara, 2015] Toriihara A, Et al., (2015) Comparison of FDG-PET/CT images between chronic renal failure patients on hemodialysis and controls. Am J Nucl Med Mol Imaging. 5(2) 204–211

[Trón, 2002] Trón L. (2002) Pozitronemissziós tomográfia és a magyar PET-program. Article in Hungarian. Orvosi Hetilap, 143:21(Suppl.3.):1235.

[DHHS, 2004] U.S. Department of Health and Human Services, (2004) Bone Health and Osteoporosis: A Report of the Surgeon General. Rockville, MD: U.S. Department of Health and Human Services, Office of the Surgeon General,

[U.S. EPA, 2008] U.S. EPA, (2008) U.S. EPA. Integrated Science Assessment (ISA) for Sulfur Oxides – Health Criteria (Final Report). EPA-600/R-08/047F. Available at: http://cfpub.epa.gov/ncea/cfm/recordisplay.cfm?deid=198843. [accessed: 20. 03. 2019]

[U.S. EPA, 2009] U.S. EPA, (2009) U.S. EPA. Risk and Exposure Assessment to Support the Review of the SO2 Primary National Ambient Air Quality Standard. EPA-452/R-09-007. July 2009. Available at: https://www3.epa.gov/ttn/naaqs/standards/so2/data/200908SO2REAFinalReport.pdf [accessed : 20. 03. 2019]

[U.S. EPA, 1997] US EPA, (1997) Technology Alternatives for the Remediation of Soils Contaminated with As, Cd, Cr, Hg, and Pb. EPA Document #EPA/540/S-97/500. United States Environmental Protection Agency Office of Emergency and Remedial Response, Washington, DC

[Vaishya, 2013] Vaishya R, Chauhan M, Vaish A.. (2013) Bone cement. J Clin Orthop Trauma. 4(4): 157–163

[Van Audenhaege 2015] Van Audenhaege K, (2015) Review of SPECT collimator selection, optimization, and fabrication for clinical and preclinical imaging. Med Phys. 42(8):4796-813

[van Dijk, 2001] van Dijk WD, Gopal S and Scheepers PT. (2001) Nanoparticles in cigarette smoke; real-time undiluted measurements by a scanning mobility particle sizer. Anal Bioanal Chem. 399: 3573-78.

[van Rikxoort, 2013] van Rikxoort EM, van Ginneken B. (2013) Automated segmentation of pulmonary structures in thoracic computed tomography scans: a review. Phys. Med. Biol. 58 R187–R220

[Varoni, 2010] Varoni MV et al, (2010) Brain renin-angiotensin system modifies the blood pressure response to intracerebroventricular cadmium in rats. Drug Chem Toxicol. 33(3):302-309

[Vermeul, 1996] Vermeul RM, (1996) Cadmium removal from phosacid. In Fertilizers as a Source of Cadmium. pp 31-43. Organisation for Economic Cooperation and Development, Paris, France

[Vogel, 1996] Vogel GC, Drago RS. (1996) The ECW Model. Journal of Chemical Education (73)8, 701-707

[Wagner, FW., 1984] Wagner FW, et al. (1984) Physical and enzymatic properties of a class III isozyme of human liver alcohol dehydrogenase: chi-ADH. Biochemistry 23:2193–2199

[Wagner, U., 2006] Wagner U, et al., (2006) Analysis of airway secretions in a model of sulfur dioxide induced chronic obstructive pulmonary disease (COPD). Journal of Occupational Medicine and Toxicology. 1:12

[Wang, 2015] Wang L, et al., (2015) A review of soil cadmium contamination in China including a health risk assessment. Environ Sci Pollut Res. (22)21. 16441–16452

[Weszl, 2012] Weszl M, et al., (2012) Freeze-dried human serum albumin improves the adherence and proliferation of mesenchymal stem cells on mineralized human bone allografts. J Orthop Res. 30(3): 489-496

[WHO, 1987] WHO, (1987) Selenium. Environmental Health Criteria 58. World Health Organization, Geneva

[WHO, 2005] WHO, (2005) Effects of air pollution on children's health and development : A review of the evidenceAvailable: http://www.euro.who.int/__data/assets/pdf_file/0010/74728/E86575.pdf [accessed 11. 12. 2014].

[WHO, 2009] WHO, (2009) Global health risks: Mortality and burden of diseases attributable to selected major risks. Geneva. Available: http://www.who.int/healthinfo/global_burden_disease/GlobalHealthRisks_report_full.pdf [accessed 11. 12. 2014]

[WHO, 2011] WHO, (2011) Cadmium in Drinking-water Background document for development of WHO Guidelines for Drinking-water Quality. WHO 2011. WHO/SDE/WSH/03.04/80/Rev/1

[WHO, 2012] WHO, (2012) 7 million premature deaths annually linked to air pollution. Available: http://www.who.int/mediacentre/news/releases/2014/air-pollution/en/ [accessed 11. 12. d 2014

[WHO, 2018] WHO, (2018) The top 10 causes of death. https://www.who.int/news-room/fact-sheets/detail/the-top-10-causes-of-death

[Williams, 2006] Williams OW et al., (2006) Airway Mucus From Production to

Secretion. Am J Respir Cell Mol Biol. 34(5): 527–536

[Wright, 1988] Wright JL, Cosio M and Churg A., (1988) Animal models of chronic obstructive pulmonary disease. Am J Physiol Lung Cell Mol Physiol. 2008 295: L1–L15.; Mahler DA, and Wells CK. Evaluation of clinical methods for rating dyspnea. Chest. 93: 580-86.

[Wright, 1990] Wright JL and Churg A. (1990) American Review of Respiratory Disease. 142. 1422-1428

[Wright, 2001] Wright JL, et al., (2001) Animal models of chronic obstructive pulmonary disease. 2008. Am J Physiol Lung Cell Mol Physiol. 295: L1–L15. ; van Dijk WD, Gopal S and Scheepers PT. Nanoparticles in cigarette smoke; real-time undiluted measurements by a scanning mobility particle sizer. Anal Bioanal Chem. 399: 3573-78.

[Wu, 2016] Wu H, et al., (2016) Environmental Exposure to Cadmium: Health Risk Assessment and its Associations with Hypertension and Impaired Kidney Function. Sci Rep. 6: 29989

[Xiaohui, 2012] Xiaohui M, et al. (2012) Molecular toxicity of earthworms induced by cadmium contaminated soil and biomarkers screening. J Environ Sci 24:1504–1510

[Yamashiro, 2011] Yamashiro T, et al. (2011) Kurtosis and skewness of density histograms on inspiratory and expiratory CT scans in smokers. COPD 8: 13-20

[Yasuda, 1998] Yasuda S, et al., (1998) Elevated F-18 FDG uptake in skeletal muscle. Clin Nucl Med. 23(2) 111-112

[Yeh, 1979] Yeh HC, Schum GM and Duggan MT. (1979) Anatomic models of the tracheobronchial and pulmonary regions of the rat. Anat Rec. 195: 483-492.

[Yip, 2016] Yip, S.S., et al., (2016) Associations between somatic mutations and metabolic imaging phenotypes in non-small cell lung cancer, J. Nucl. Med. Off. Publ. Soc. Nucl. Med. (September)

[Yoon, 2015] Yoon, H.J. et al., (2015) Decoding tumor phenotypes for ALK, ROS1, and RET fusions in lung adenocarcinoma using a radiomics approach, Medicine (Baltimore) 94 (October (41)) (2015) e1753

[Yoshida, 1999] Yoshida F, Hata A, Tonegawa H. (1999) Itai-Itai disease and the countermeasures against cadmium pollution by the Kamioka mine. Environmental Economics and Policy Studies, 2: 215-229

[Zang-Hee, 2011] Zang-Hee Cho, et al., (2011) Fusion of PET and MRI for Hybrid Imaging. T.M. Deserno (ed.), Biomedical Image Processing, Biological and Medical Physics, Biomedical Engineering, Springer-Verlag Berlin Heidelberg

[Zhang, 2005] Zhang X. L, et al., (2005) Source diagnostics of polycyclic aromatic hydrocarbons based on species ratios: a multimedia approach. Environmental Science and Technology. (39)23. 9109–9114

12. APPENDIX

Table 1.

Component	Grams/Liter	Concentration (mMol)
Sodium chloride	4.38	75.00
Potassium chloride	0.30	4.00
Calcium chloride	0.22	2.00
Magnesium chloride	0.10	1.00
Tris	1.21	1.00
Sucrose	7.87	23.00
pH adjusted to 7.4 with HCl		

Table 1. The quantities of compounds used to prepare the special earthworm Ringer solution, based on Drewes and Pax's Ringer, but sulfate ions were replaced with chloride ions in all used components.

PLOS | ONE

RESEARCH ARTICLE

Novel radiomics evaluation of bone formation utilizing multimodal (SPECT/X-ray CT) *in vivo* imaging

Ferenc Budán[1,2], Krisztián Szigeti[3], Miklós Weszl[3,4,5], Ildikó Horváth[3], Erika Balogh[1], Reem Kanaan[1], Károly Berényi[1], Zsombor Lacza[4], Domokos Máthé[3,6], Zoltán Gyöngyi[1]*

1 Department of Public Health Medicine, Medical School, University of Pécs, Pécs, Hungary, **2** MedProDevelop, Pécs, Hungary, **3** Department of Biophysics and Radiation Biology, Semmelweis University, Budapest, Hungary, **4** Department of Health Economics, Corvinus University of Budapest, Budapest, Hungary, **5** Institute of Clinical Experimental Research, Semmelweis University, Budapest, Hungary, **6** CROmed Translational Research Centers, Budapest, Hungary

* zoltan.gyongyi@aok.pte.hu

Abstract

Although an extensive research is being undertaken, the ideal bone graft and evaluation method of the bone formation draw still a warranted attention. The purpose of this study was to develop a novel multimodal radiomics evaluation method, utilizing X-ray computed tomography (CT) and single photon emission computed tomography (SPECT) with Tc-99m-Methyl diphosphonate (Tc-99m-MDP) tracer. These modalities are intended to provide quantitative data concerning the mineral bone density (after evaluation it is referred to as opacity) and the osteoblast activity, at the same time. The properties of bone formation process within poly (methyl methacrylate)-based bone cement graft (PMMA) was compared to that of albumin coated, sterilized, antigen-extracted freeze-dried human bone grafts (HLBC), in caudal vertebrae (C5) of rats. The animals were scanned at 3 and 8 weeks after surgery. In both groups, the mean opacity increased, while the mean Tc-99m-MDP activity decreased. The later parameter was significant ($n = 4$, $p = 0.002$) only in HLBC group. The linear regression analysis of PMMA-treated group variables (mean opacity increase; mean Tc-99m-MDP activity decrease), revealed a negative correlation with the medium strength ($r = 0.395$, $p = 0.605$). Whereas, it showed strong positive correlation when HLBC group variables were analyzed ($r = 0.772$, $p = 0.012$). These results indicate that using HLBC grafts is advantageous in terms of the osteoblast activity and bone vascularization over PMMA cement. Using this regression analysis method, we were able to distinguish characteristics that otherwise could not be distinguished by a regular data analysis. Hence, we propose utilizing this novel method in preclinical tests, and in clinical monitoring of bone healing, in order to improve diagnosis of bone-related diseases.

Citation: Budán F, Szigeti K, Weszl M, Horváth I, Balogh E, Kanaan R, et al. (2018) Novel radiomics evaluation of bone formation utilizing multimodal (SPECT/X-ray CT) *in vivo* imaging. PLoS ONE 13(9): e0204423. https://doi.org/10.1371/journal.pone.0204423

Editor: Parasuraman Padmanabhan, Lee Kong Chian School of Medicine, SINGAPORE

Received: May 10, 2018

Accepted: September 9, 2018

Published: September 25, 2018

Data Availability Statement: All relevant data are within the paper and its Supporting Information file.

Funding: The authors received no specific funding for this work. Ferenc Budán is employed by MedProDevelop. Domokos Máthé is employed by CROmed Translational Research Centers. MedProDevelop and CROmed Translational Research Centers provided support in the form of salaries for authors [FB and DM], but did not have any additional role in the study design, data collection and analysis, decision to publish, or preparation of the manuscript. The specific roles of these authors are articulated in the 'author contributions' section.

Competing interests: Ferenc Budán is employed by MedProDevelop. Domokos Máthé is employed by CROmed Translational Research Centers. There are no patents, products in development or marketed products to declare. This does not alter our adherence to all the PLOS ONE policies on sharing data and materials.

Introduction

Bone grafting is the replacement of missing bone utilizing a surgical procedure. The ideal bone grafts possess certain essential properties, such as efficacious and safe use, biocompatibility, appropriate mechanical/chemical attributions, cost-effectiveness, convenient usage, as well as production and availability in a large quantity [1]. Materials, such as poly (methyl methacrylate)-based (PMMA) cements were widely used. Extensive research is going on in animals to detect the safety of newly developed experimental bone graft materials [2]. Clinical studies are also ongoing so as to map the beneficial effects of novel bone grafts. Adding or mixing several materials such as demineralized bone matrix (DBM), ceramics, coral, graft composites, and bone morphogenetic proteins, etc. to the bone cement can improve its biological function [3–5]. Biomaterials, like albumin coated, sterilized, antigen-extracted freeze-dried human bone graft (HLBC), can acquire function via chemical treatments, for example by coating or surface grafting. These modifications improve wound healing or even control cell fate *in situ* [6]. However, ideal bone grafts are still necessary [7]. Furthermore, suitable evaluation methods of specific bone grafts are yet to be developed.

The rat tail model has major advantages over other animal models. These include effectiveness regarding to its cost as well as the accessibility of the bones [8–10]. However, rat bone structure lacks a haversian system [11]. Apart from the bone remodeling process, microstructure of rat bone is similar to more advanced species, with regard to bone formation properties [12]. These properties depend mainly on the osteoblast activity and bone vascularization [13].

Consequently, the bone-healing process could be followed up, utilizing a rat tail model, in order to evaluate the synthetically modified and the biologically derived bone substitutes as well as the xenogeneic bone graft [9, 14].

The X-ray attenuation of a specific voxel correlates to the cube of effective atomic numbers of the components. These effective atomic numbers contribute to the attenuation according to their molar quantity [15, 16].

Thus, the X-ray CT as a noninvasive technique is especially well-suited for applications involving the measurements of bone density, owing to the high signal contrast between bone and soft tissue [16]. The X-ray attenuation (after specific data processing, see below) in this context is referred to as opacity. Moreover, the specific technical properties of the utilized CT (e.g. beam-energy profiles), as well as other factors, can influence the measurements [16]. Therefore, the mean opacity values of the examined region of interest (ROI) can be normalized to the opacity values of an intact ROI of the same object. The same is true of the adequate selection of X-ray attenuation "density" cut-offs in order to filter-out the tissues (or objects), irrelevant from perspective of examinations [17].

In the clinical practice, bone scintigraphy is a widespread screening method that is based on osteoblast labeling by Tc-99m-Methyl diphosphonate (Tc-99m-MDP) [18]. The Tc-99m-MDP accumulates in the bone by chemical adsorption and incorporates into the hydroxyapatite structure [19]. Areas with high osteogenic activity are Tc-99m-MDP absorbers and can be identified with gamma camera [19]. SPECT imaging with a Tc-99m-MDP tracer has been used frequently in nuclear medicine for the *in vivo* diagnosis of abnormalities in bone formation and remodeling, including osteogenic tumors or metabolic bone diseases [18–20].

The multimodal *in vivo* imaging is capable to provide anatomical and functional information simultaneously [21]. This could be applied to obtain more quantified and comparable data. In previous study, the bone formation was investigated with multimodal NanoSPECT/CT in rat tail implant model [22]. The results have revealed that the bone formation is supposed to be detectable three weeks after bone graft insertion with both modalities [22]. Additionally, eight weeks following the bone graft insertion, the healing process might still be ongoing as indicated by the increase in the bone opacity along with the decrease of the standardized uptake volume (SUV) of Tc-99m-MDP [10, 22]. This healing process lasts 12–14 weeks following the surgery [10, 22].

Moreover, multiple testing with the same animal, combined with radiomics evaluation, provides more relevant biological information [10, 17].

The purpose of this study was to find a new radiomics evaluation method, calculating linear regression from the bone opacity and activity of Tc-99 m-MDP, regarding the bone healing properties. HLBC and PMMA were aimed to examine in this study. A further goal of this study, was to highlight that implementing a radiomics evaluation method, can result in reducing the number of animals needed for conducting experiments. This goal is in coherence with the European Union (EU) directive 2010/63/EU on the protection of animals [10, 23].

Materials and methods

Animal model

Two groups (n = 5) of female Wistar rats (Crl(Wi)Br, Charles River; 650–950 g from the breeding colony of Semmelweis University (Hungary)) were kept in light controlled, air-conditioned rooms and fed *ad libitum*. All the procedures were conducted in accordance with the ARRIVE guidelines and the guidelines set by the European Communities Council Directive (86/609 EEC) and approved by the Animal Care and Use Committee of Semmelweis University (protocol number: XIV-I-001/29-7/2012).

The surgical model of Blazsek et al. was applied, described briefly below [14]. In the spongious model of Blazsek et al., rats were anesthetized with sodium pentobarbital (Nembutal (Sigma-Aldrich) 40 mg/kg body weight (b.w.), by intraperitoneal (i.p.) injection). The tail above the C4 vertebrae was ligatured to control bleeding during surgery. The tail was disinfected, then was partly removed after the C5 vertebra. A 5–6 mm incision was made at the level of caudal *vertebrae* (C4–C5). The skin was retracted and the vertebras were exposed under sterile conditions. In the exposed central surface of C5, a 1 mm diameter and 5 mm deep hole was formed using an electric drill, corresponding to the size of a titanium screw. Subsequently, a hole was made (2.0 mm diameter and 3.5 mm depth) creating an "empty" cylinder, which allowed 360° rotation. Screw-type titanium implants (1.2 mm diameter and 3.5 mm length) were fabricated and their surface roughened using sandblasting (Full-Tech Company, Hungary). The sterilized screws were introduced into the 5 mm deep thin hole. Following insertion of the implant the skin was repositioned over the implant and tightly sutured. The surgical wound was protected aseptically by a plastic methyl-methacrylate butyl-acrylate butyl-methacrylate copolymer, diisooctyl phthalate film layer (Plastubol®, Pannonpharma Ltd. Hungary). The rats were kept in individual cages to insure appropriate hygiene and wound healing during the first two weeks following surgery. In each animal, 3 weeks after surgical intervention, the titanium implant was removed and the remained hole was filled with the experimental materials, see below [14].

In this study, one animal group (n = 5) were treated with chemically sterilized, antigen-extracted HLBC (West Hungarian Regional Tissue Bank) and one group (n = 5) with PMMA-based cement (Vertebroplastic, DePuy, USA) experimental materials. The HLBC was pretreated; a human serum albumin coating method (200g/1000ml, BIOTEST) was applied [24].

After the experiment, animals were killed by cervical dislocation. The autopsy was carried out in order to detect potential abnormalities e.g. inflammation.

Detection and image evaluation

The animals (n = 5) were scanned 3 and 8 weeks after surgery using a quantitative multiplexed multipinhole NanoSPECT/CT+ (Mediso, Hungary). The acquisition time was 30 min for X-ray CT. The reconstructed cubic voxel side size was 150 μm in a 198 × 198 × 546 pixel matrix in both the SPECT and CT modalities. Fusion (Mediso Ltd., Hungary) and VivoQuant (inviCRO LLC, US) image analysis softwares were used to further analyze the reconstructed, reoriented and co-registered images by drawing appropriate volumes of interests (VOIs) over the specific caudal (C4, C5) *vertebrae*.

From the whole SPECT image, the C5 and C4 *vertebrae* of tail were selected then VOIs were marked. The isotope activity in VOI was summed. The radioactive dose concentration of Tc-99m-MDP was determined by dividing measured radioactivity in an animal (in MBq) by the whole body weight (in grams) of the animal to calculate the standard uptake volume (SUV) [22].

The summarized absorbance of VOI was calculated. The voxels in VOI with attenuation below 1400 Hounsfield Unit (HU) were cut off in order to filter the soft tissue from total X-ray attenuation of interest vertebra. Thus, only the mineralized bone tissue of C5 and C4 *vertebrae* was evaluated. This attenuation values were normalized in the following manner. The ratio of summarized bone mineral density (attenuation) of treated and control *vertebrae* was calculated representing normalized bone mineral density (in this context is referred to as opacity). From each group, 1 experimental animal with signs of inflammation was removed. These calculations were performed for all animals also 3 and 8 weeks after bone graft insertion as well and the statistical mean and SD were calculated.

The same quantitative multiplexed multipinhole NanoSPECT/CT+ (Mediso, Hungary) was utilized for selected rats (n = 4) to carry out a SPECT examination 3 and 8 weeks after surgery. The rats were scanned 3 h after the injection of 80 MBq of Tc-99m-MDP. After the acquisition, the data were reconstructed with the HiSPECT software.

These results were normalized in the same way as mentioned before. Thus, SUV ratios were used to measure the treatment response less depended on noise and image resolution. Normalized SUV values in this context are referred to as Tc-99m-MDP activity. This process was performed on each animal. The mean and SD values of Tc-99m-MDP activity in specific PMMA and HLBC groups were calculated in both of the examined time periods.

2-tailed Student's t-test was performed for statistical evaluation of the mean and standard deviation (SD) values of bone opacity as well as the Tc-99m-MDP activity in both of the examined time periods. The ratios of mean parameters at three and at eight weeks after bone graft insertion were determined. The means of opacity change were expressed in percent of opacity increasing from third to the eighth week. The mean of Tc-99m-MDP activity change was calculated for both groups utilizing the mentioned ratios between the parameters of three and of eight weeks after bone graft insertion and expressed in the percent of activity decreasing from third week to the eighth week. Finally, a linear regression analysis was carried out to examine the correlation between the opacity change and the Tc-99m-MDP activity change.

Results

The mean opacity increased, while the mean Tc-99m-MDP activity decreased, in both of the groups and at both time points that are at 3 and 8 weeks following treatment. Fig 1 shows *vertebrae* at starting point while Fig 2 represents *vertebrae* after eight weeks. Fig 1 shows the exact anatomical position of VOI and Fig 2 the raw activity of Tc-99m-MDP only for the sake of illustration. Images showing the structure and the activity only represent similar measurements, since a visual comparison of the raw data derived from each acquisition does not provide enough information for proper quantitative evaluation. The CT is useful to detect structure (Fig 1), but the SPECT could provide the data of Tc-99m-MDP activity (Fig 2).

The difference between the PMMA and HLBC opacity values at the third and the eighth weeks were not significant (n = 4, p = 0.378) and (n = 4, p = 0.591), respectively (Fig 3A and 3B).

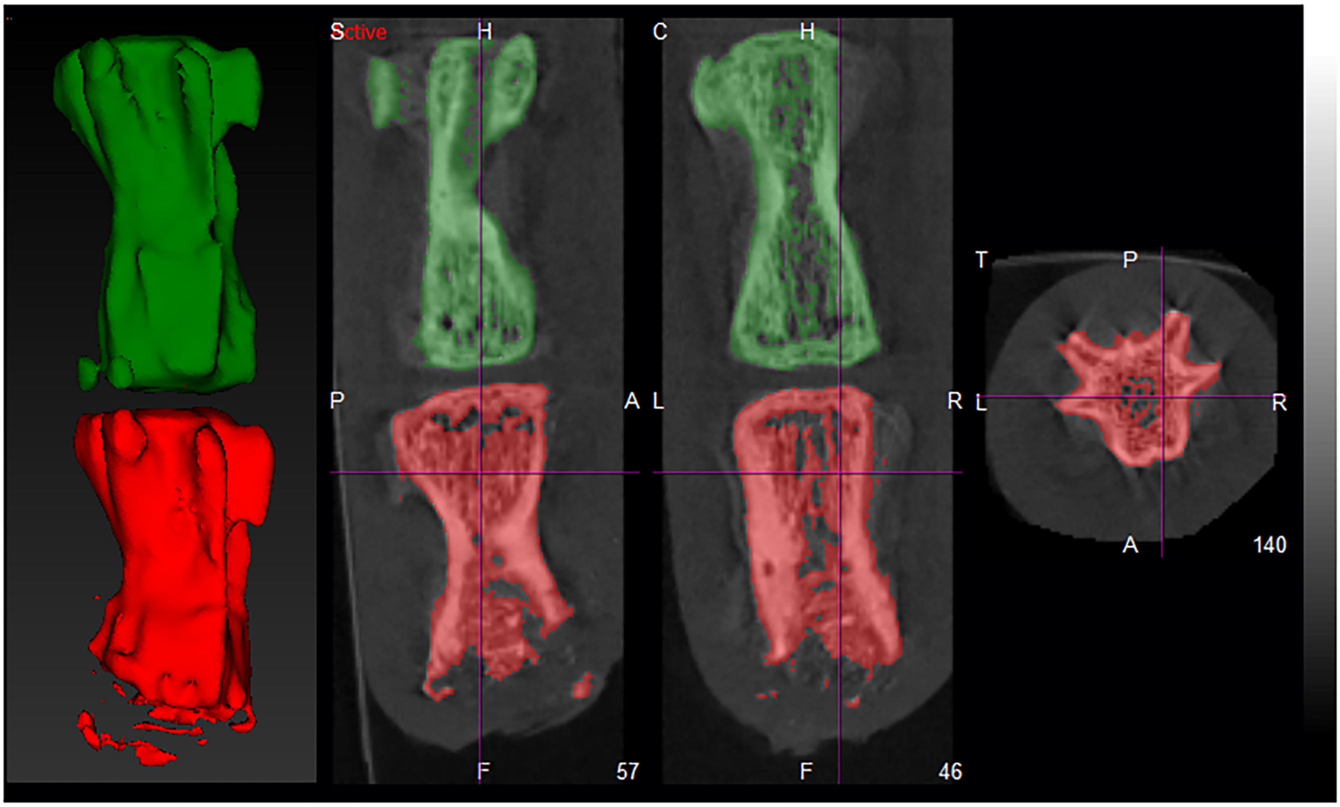

Fig 1. Structure of *caudal vertebrae* of treated rats at starting point. The C5 *vertebra* (red colour) was treated and filled with a bone graft which was selected as VOI for evaluation of CT. The green coloured C4 *vertebrae* show the VOI of control.

https://doi.org/10.1371/journal.pone.0204423.g001

Additionally, the difference between the PMMA and HLBC Tc-99m-MDP activity values at the third week were also not significant (n = 4, p = 0.651) (Fig 3C). Likewise, these differences at the eighth week (n = 4, p = 0.807) were also not significant (Fig 3D).

Only in the HLBC group, the activity of the mean of Tc-99m-MDP decreased significantly (n = 4, p = 0.002) starting from the third week until the eighth week (Fig 3C and 3D).

The mean opacity change in PMMA group compared to the same parameter of HLBC group was not significantly different (n = 4, p = 0.395) (Fig 4A). Similarly, the mean activity change of Tc-99m-MDP in PMMA and HLBC groups was not significant (n = 4, p = 0.468) (Fig 4B).

Performing linear regression analysis (Fig 5), a strong positive correlation was found in HLBC group comparing the increase of bone opacity and decrease of Tc-99m-MDP activity variables (r = 0.772, p = 0.012).

In case of the PMMA treated group, medium negative correlation was found between these two variables (r = 0.395, p = 0.605).

With exception to one rat from each group, autopsy did not reveal any pathological condition including inflammation. In both groups the excluded rats have had inflammation.

Discussion

The mean opacity increase of examined voxels in both groups between 3 and 8 weeks after surgery indicates the progress of bone tissue mineralization. The bone formation process was

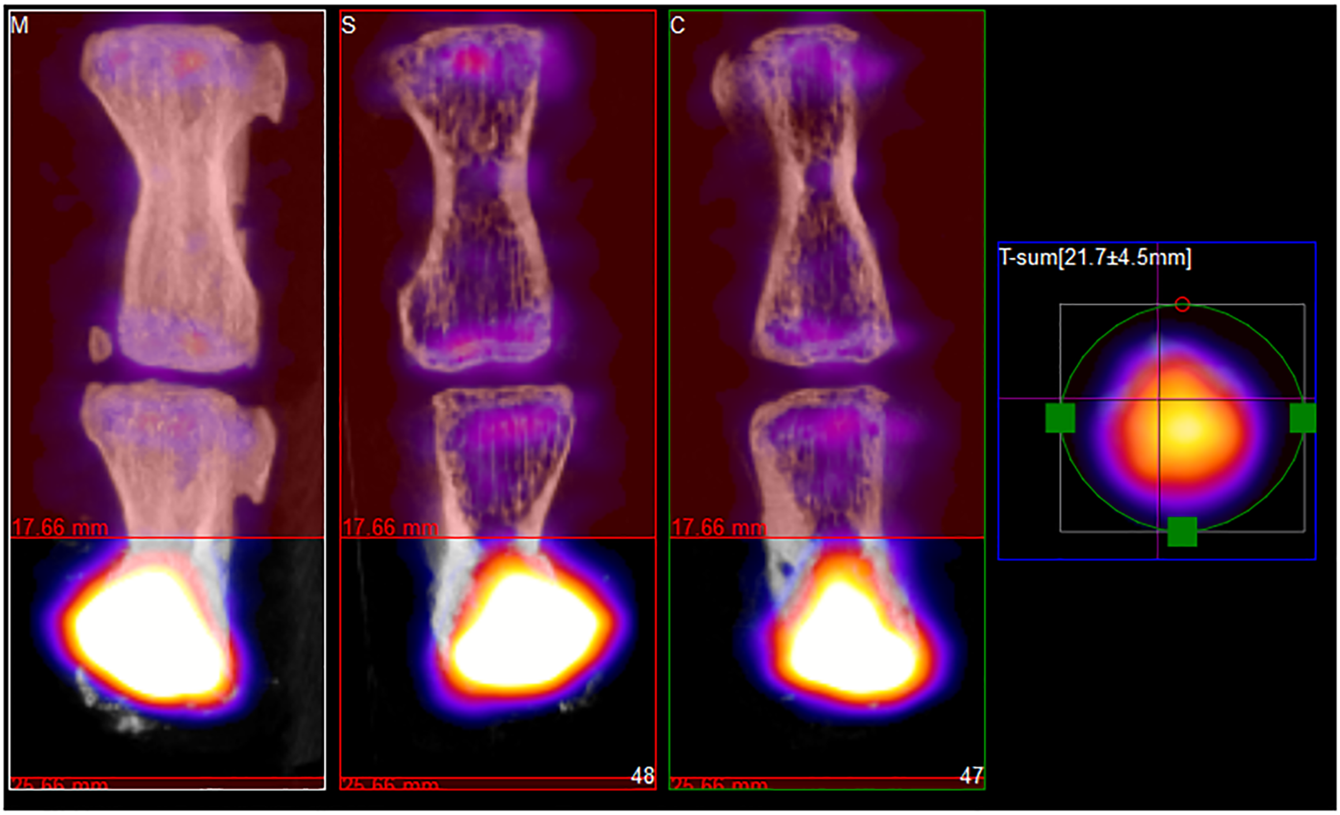

Fig 2. Tc-99m-MDP activity in *caudal vertebrae* of treated rats after eight weeks. The C5 *vertebrae* (down) were treated and filled with a bone graft which was selected as VOI in SPECT at eight weeks after surgery. The colour intensity shows the activity of Tc-99m-MDP in the last region of *vertebra*. The upper bones are C4 control *vertebrae*.

https://doi.org/10.1371/journal.pone.0204423.g002

enhanced either by PMMA or HLBC, respectively (Fig 3A and 3B). Most of the grafts generally provided template to guide the repairing tissue [1, 25]. Thus, autonomic healing is achievable in PMMA bone cement brand [26]. It has to be noted that the mean opacity values of the two experimental groups, could not be distinguished from each other in a statistically significant manner. These indistinguishable values were obtained despite the fact that normalization of C5 vertebrae to intact C4 vertebrae and filtration of HU values below 1400 HU measures were undertaken (Fig 3A and 3B). Still, the applied bone graft attributions may cause slightly increase of the mean opacity of HLBC group when compared to PMME group [22]. Indeed, in MC3T3-E1 cell culture, the PMMA particles impaired cell proliferation and inhibited the expression of *RUNX2* and *DLX5* genes in a dose-dependent manner [27].

The HLBC enhanced bone formation in a previous publication, similarly to PMMA [22]. This was highlighted in specific Tc-99m-MDP uptake profile of both groups starting at the third week until eighth week after surgery. In the PMMA group, the Tc-99m-MDP uptake was slightly decreased, whereas, a strong decrease in HLBC group was obtained in a statistically significant manner (Fig 3C and 3D).

The increase of mean opacity ratio from third week to eighth week following surgery was stronger in the PMMA group than in the HLBC group (Fig 4A). However, in previous publications it was indicated that the PMMA enhanced bone formation less exquisitely and it was delayed when compared to HLBC's bone formation enhancement [28, 29]. Indeed, the low mean opacity value in the PMMA group at third week after surgery was reflected in the mean

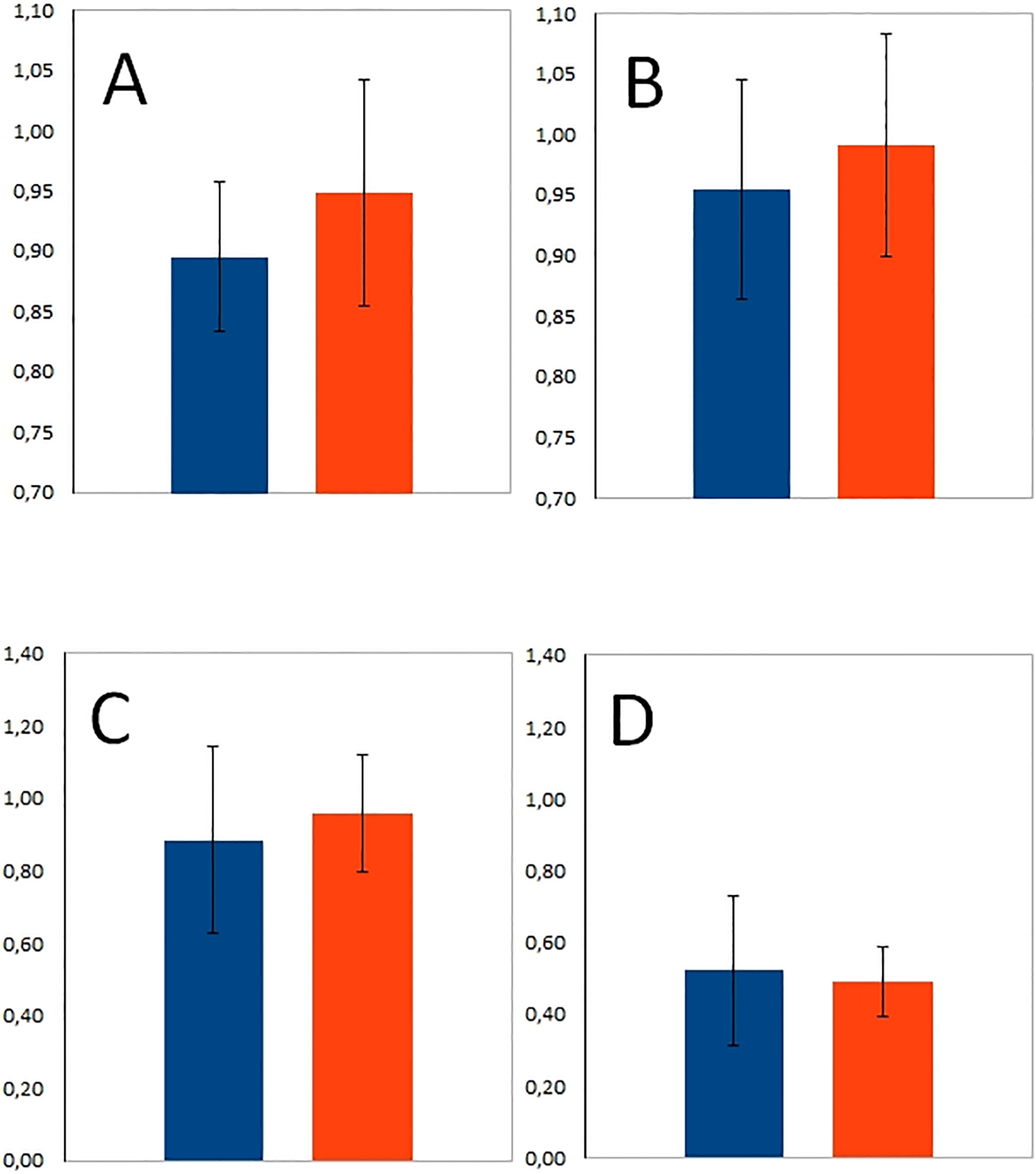

Fig 3. Mean opacity and mean Tc-99m-MDP activity. The figure represents the mean opacity (above) and the mean Tc-99m-MDP activity (below) of PMMA (blue) and HLBC (orange) at third weeks (A, C) and at eight weeks after surgery (B, D).

https://doi.org/10.1371/journal.pone.0204423.g003

opacity ratio (Figs 3A and 4A). This result constitutes a spectacular example of advantages of multimodal imaging, since the aforementioned data are in concordance with Tc-99m-MDP uptake data. This uptake represents functional information that might highlight the features of bone formation process (Fig 4B). Thus, the change in the ratio by itself could not be used as a

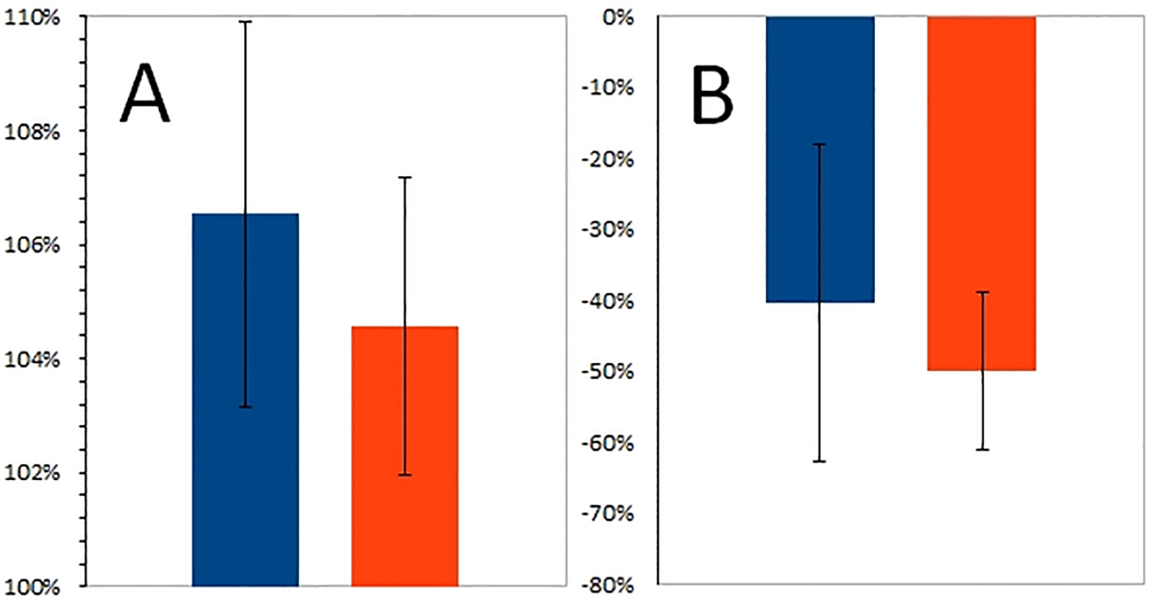

Fig 4. Change ratio %. Change ratio % from third week to eighth week after surgery of mean opacity increase (A) and mean Tc-99m-MDP activity decrease % (B) for PMMA (blue) and HLBC (orange) groups.

https://doi.org/10.1371/journal.pone.0204423.g004

reliable descriptive parameter for bone formation, especially with such a low sample number as was the case in this experiment. In this investigational set-up, Tc-99m-MDP uptake ratio was informative in regard to the osteoblast activity [22] (Fig 4B). However, pathologic conditions such as neoplasticity, hormonal changes, inflammation, ischemia, may cause abnormal Tc-99m MDP uptake in soft-tissues, thereby, limiting the sensitivity of this method with false positive results [30].

Multimodal Tc-99m-MDP NanoSPECT/CT imaging utilizing radiomics evaluation has elucidated the decreasing Tc-99m-MDP uptake in relation to bone opacity change increase (Figs 4 and 5). The results of linear regression analysis pointed out the discrepancy between the examined group trends. The variables of PMMA group showed negative, while HLBC group's revealed positive correlation (Fig 5).

Clearly, the PMMA lacks both osteoinductive and osteoconductive mechanisms [31]. Consequently, in the PMMA group, th osteoblast activity indicated a healing process showing a medium negative correlation with the bone density.

However, the HLBC showed a strong positive significant correlation between the increased opacity ratio and the decreased Tc-99m MDP activity. Probably because revascularization of the cancellous autografts takes place earlier than the cortical grafts', as early as the fifth day following implantation, due to their porous architecture [28, 29]. In addition, in the HLBC group the creeping-substitution mechanism has enhanced vascularization and albumin-coated surface promoted osseointegration [24, 32].

Novelty of our method was that we did not only measure the bone opacity and the activity of a radioactive isotope, which parameters provide conventional data about density, formation and healing of bone, but we calculated linear regression from the opacity and the activity. The advantage of our method is that we could distinguish different bone grafts by healing efficacy which was impossible to achieve by existing techniques. The other advantage is that there is no additional cost since existing SPECT/X-ray CT instruments can be used without modification. The only disadvantage is that we needed to calculate an extra linear regression.

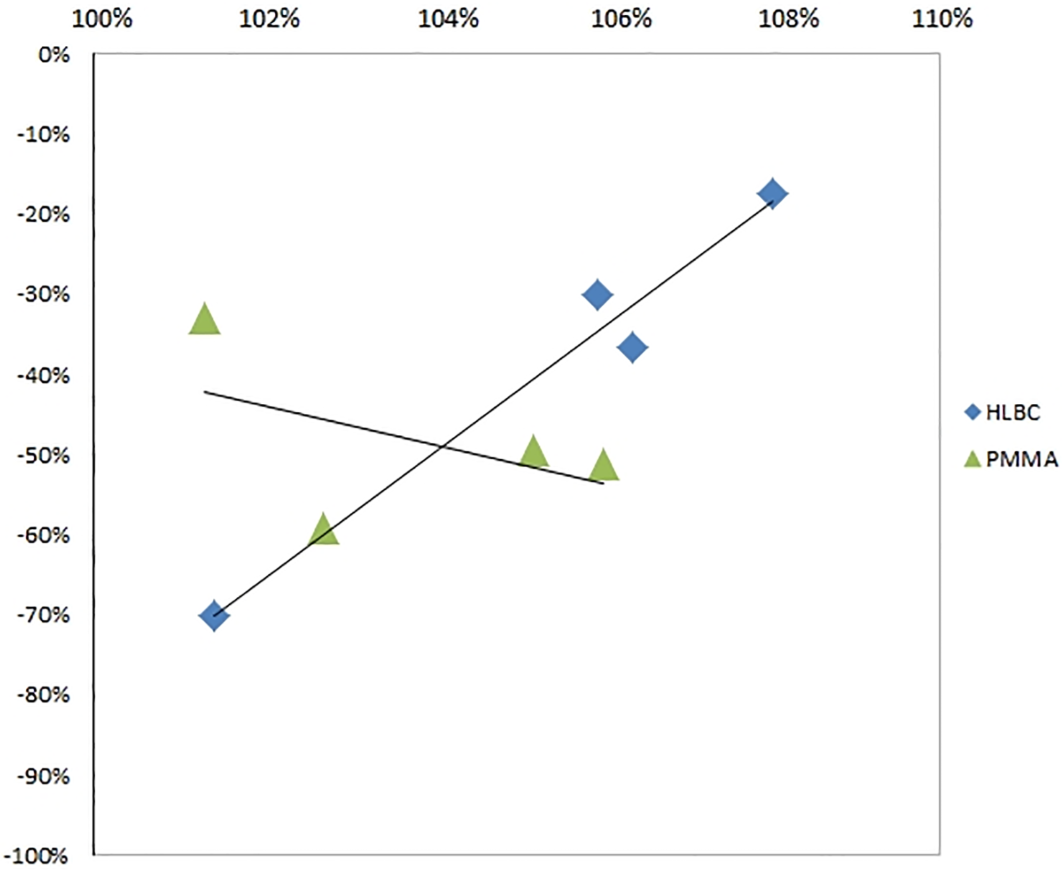

Fig 5. Linear regression. The ratio of opacity increasing % and the ratio of Tc-99m-MDP activity decreasing % from 3rd week after surgery to 8th week after surgery values for each individual animal in PMMA (triangle) and HLBC (diamond) groups were determined. A linear regression analysis was carried out.

https://doi.org/10.1371/journal.pone.0204423.g005

Conclusions

The examined bone grafts have enhanced the bone mineralization process, as revealed by X-ray CT. Despite of normalization of the attenuation values of the C5 vertebra to the intact C4 vertebra, and the filtration of the opacity below 1400 HU, the difference between PMMA and HLBC groups was not statistically significant. The common attributions of the examined bone graft materials underpin a bone formation enhancer effect.

Using NanoSPECT, the decreased Tc-99m MDP activity was shown to be significant in the HLBC group between the third and eighth weeks following a surgery. With a linear regression analysis, the decrease in osteoblast activity ratio related to the increase in opacity ratio was examined. In the PMMA group, negative correlation was obtained, contrary to the results in the HLBC group.

The applied experimental set-up is cost-effective, presents quick and quantitative results and reduced the use of animals, in coherence with the European Union (EU) directive 2010/63/EU on the protection of animals [23]. This novel multimodal Tc-99m-MDP NanoSPECT/CT radiomics approach may be useful to compare several experimental bone replacement materials in preclinical studies. In addition, tracking of clinical bone formation can be established based on the results of this study. The presented multimodal *in vivo* imaging may support the optimal therapeutic strategy not only in correlation to bone healing, bone grafting and bone replacement, but also to the advancement of prognosis of bone diseases.

Supporting information

S1 Table. Raw data of opacity and activity.
(XLSX)

Author Contributions

Conceptualization: Ferenc Budán, Krisztián Szigeti, Miklós Weszl, Zsombor Lacza, Domokos Máthé, Zoltán Gyöngyi.

Data curation: Krisztián Szigeti.

Formal analysis: Ferenc Budán, Krisztián Szigeti, Károly Berényi.

Funding acquisition: Zoltán Gyöngyi.

Investigation: Ferenc Budán, Ildikó Horváth.

Methodology: Ferenc Budán.

Project administration: Ferenc Budán, Zsombor Lacza, Domokos Máthé.

Resources: Krisztián Szigeti, Zsombor Lacza, Domokos Máthé.

Supervision: Krisztián Szigeti, Domokos Máthé, Zoltán Gyöngyi.

Writing – original draft: Ferenc Budán, Krisztián Szigeti, Miklós Weszl, Erika Balogh, Domokos Máthé.

Writing – review & editing: Reem Kanaan, Zoltán Gyöngyi.

References

1. Chen FM, Liu X. Advancing biomaterials of human origin for tissue engineering. Prog Polym Sci. 2016; 53: 86–168. https://doi.org/10.1016/j.progpolymsci.2015.02.004. PMID: 27022202
2. Sheikh Z, Hamdan N, Ikeda Y, Grynpas M, Ganss B, Glogauer M. Natural graft tissues and synthetic biomaterials for periodontal and alveolar bone reconstructive applications: a review. Biomater Res. 2017; 21: 9. https://doi.org/10.1186/s40824-017-0095-5 PMID: 28593053
3. Sullivan MP, McHale KJ, Parvizi J, Mehta S. Nanotechnology: current concepts in orthopaedic surgery and future directions. Bone Joint J. 2014; 96(5): 569–573. https://doi.org/10.1302/0301-620X.96B5.33606 PMID: 24788488
4. Huber FX, Hillmeier J, Herzog L, McArthur N, Kock HJ, Meeder PJ. Open reduction and palmar plate-osteosynthesis in combination with a nanocrystalline hydroxyapatite spacer in the treatment of comminuted fractures of the distal radius. J Hand Surg Br. 2006; 31(3): 298–303. https://doi.org/10.1016/j.jhsb.2005.12.006 PMID: 16487633
5. Kon E, Delcogliano M, Filardo G, Pressato D, Busacca M, Grigolo B, et al. A novel nano-composite multi-layered biomaterial for treatment of osteochondral lesions: technique note and an early stability pilot clinical trial. Injury. 2010; 41(7): 693–701. https://doi.org/10.1016/j.injury.2009.11.014 PMID: 20035935
6. Roach P, Eglin D, Rohde K, Perry CC. Modern biomaterials: a review-bulk properties and implications of surface modifications. J Mater Sci Mater Med. 2007; 18: 1263–1277. https://doi.org/10.1007/s10856-006-0064-3 PMID: 17443395
7. Gupta AK, Keshav K, Kumar P. Decalcified allograft in repair of lytic lesions of bone: A study to evolve bone bank in developing countries. Indian J Orthop. 2016; 50: 427–433. https://doi.org/10.4103/0019-5413.185609 PMID: 27512226
8. Fitzgerald TA. Comparison of research cost: man primate animal other animal models. J Med Primatol. 1983; 12: 138–145. PMID: 6438331

9. Ellender G, Feik SA, Carach BJ. Periosteal structure and development in a rat caudal vertebra. J Anat. 1988; 158: 173–187. PMID: 3225221
10. Renaud M, Farkasdi S, Pons C, Panayotov I, Collart-Dutilleul PY, Taillades H, et al. A new rat model for translational research in bone regeneration. Tissue Eng Part C Methods 2016; 22: 125–131. https://doi.org/10.1089/ten.TEC.2015.0187 PMID: 26472155
11. Nunamaker DM. Experimental models of fracture repair. Clin Orthop Relat R. 1998; 355: S56–S65.
12. Chambers TJ, Evans M, Gardner TN, Turner-Smith A, Chow JW. Induction of bone formation in rat tail vertebrae by mechanical loading. Bone Miner. 1993; 20(2): 167–178. PMID: 8453332
13. Albrektsson T, Johansson C. Osteoinduction, osteoconduction and osseointegration. Eur Spine J. 2001; 10: S96–S101. https://doi.org/10.1007/s005860100282 PMID: 11716023
14. Blazsek J, Dobó NC, Blazsek I, Varga R, Vecsei B, Fejérdy P, et al. Aminobisphosphonate stimulates bone regeneration and enforces consolidation of titanium implant into a new rat caudal vertebrae model. Pathol Oncol Res. 2009; 15: 567–577. https://doi.org/10.1007/s12253-009-9156-y PMID: 19267222
15. Feeman TG. The Mathematics of Medical Imaging: A Beginner's Guide. New York: Springer-Verlag; 2010. https://doi.org/10.1007/978-3-319-22665-1
16. Coles ME, Muegge EL, Auzerais F, Frulla P, Kantzas A. The use of attenuation standards for CT scanning. SCA Conference Paper1995: 9513.
17. Szigeti K, Szabó T, Korom C, Czibak I, Horváth I, Veres DS, et al. Radiomics-based differentiation of lung disease models generated by polluted air based on X-ray computed tomography data. BMC Med Imaging. 2016; 16: 14. https://doi.org/10.1186/s12880-016-0118-z PMID: 26864653
18. Chopra A. 99mTc-Methyl diphosphonate. In: Molecular Imaging and Contrast Agent Database (MICAD). Bethesda (MD): National Center for Biotechnology Information (US); 2004–2013. https://www.ncbi.nlm.nih.gov/books/NBK24575/.
19. Kanishi D. 99mTc-MDP accumulation mechanisms in bone. Or Surg Or Med Or P. 1993; 75(2): 239–246. https://doi.org/10.1016/0030-4220(93)90100-I PMID: 8381217
20. Fogelman I, Bessent RG, Turner JG, Citrin DL, Boyle IT, Greig WR. The use of whole-body retention of Tc-99m diphosphonate in the diagnosis of metabolic bone disease. J Nucl Med. 1978; 19(3): 270–275. PMID: 564941
21. Szigeti K, Hegedűs N, Rácz K, Horváth I, Veres DS, Szöllősi D, et al. Thallium labelled citrate coated Prussian blue nanoparticles as potential imaging agent. Contrast Media Mol I. 2018;2023604, 10 pages https://doi.org/10.1155/2018/2023604.
22. Aberg J, Pankotai E, Billström GH, Weszl M, Larsson S, Forster-Horváth C, et al. In vivo evaluation of an injectable premixed radiopaque calcium phosphate cement. Int J Biomater. 2011;232574. https://doi.org/10.1155/2011/232574 PMID: 21760794
23. Hartung T. Comparative analysis of the revised Directive 2010/63/EU for the protection of laboratory animals with its predecessor 86/609/EEC—a t4 report. ALTEX. 2010; 27(4): 285–303. https://doi.org/10.14573/altex.2010.4.285 PMID: 21240470
24. Weszl M, Skaliczki G, Cselenyák A, Kiss L, Major T, Schandl K, et al. Freeze-dried human serum albumin improves the adherence and proliferation of mesenchymal stem cells on mineralized human bone allografts. J Orthop Res. 2012; 30(3): 489–496. https://doi.org/10.1002/jor.21527 PMID: 22371968
25. Thoren K, Aspenberg P, Thorngren KG. Lipid extracted bank bone. Bone conductive and mechanical properties. Clin Orthop Relat R. 1995; 311: 232–246.
26. Lewis G, Wellborn B, Jones Ii L, Biggs P. A room-temperature autonomically-healing PMMA bone cement: influence of composition on fatigue crack propagation rate. J Appl Biomater Biom. 2009; 7(2): 90–96.
27. Chiu R, Smith KE, Ma GK, Ma T, Smith RL, Goodman SB. Polymethylmethacrylate particles impair osteoprogenitor viability and expression of osteogenic transcription factors Runx2, osterix, and Dlx5. J Orthop Res. 2010; 28(5): 571–577. https://doi.org/10.1002/jor.21035 PMID: 20014320
28. Sheikh ZA, Hamdan N, Ikeda Y, Grynpas M, Ganss B, Glogauer M. Natural graft tissues and synthetic biomaterials for periodontal and alveolar bone reconstructive applications: a review. Biomater Res. 2017; 21: 9. https://doi.org/10.1186/s40824-017-0095-5 PMID: 28593053
29. Sheikh ZA, Javaid A, Abdallah MA. Bone replacement graft materials in dentistry. In: Khurshid Z, Zafar SZ, editor. Dental biomaterials (Principle and its Application). 2nd ed: Paramount Publishing Enterprise: Karachi, Pakistan, 2013.
30. Peller PJ, Ho VB, Kransdorf MJ. Extraosseous Tc-99m MDP uptake: a pathophysiologic approach. Radiographics. 1993; 13(4): 715–734. https://doi.org/10.1148/radiographics.13.4.8356264 PMID: 8356264

31. Vaishya R, Chauhan M, Vaish A. Bone cement. J Clin Orthop Trauma. 2013; 4(4): 157–163. https://doi.org/10.1016/j.jcot.2013.11.005 PMID: 26403875

32. Aspenberg P, Thorén K. Lipid extraction enhances bank bone incorporation. An experiment in rabbits. Acta Orthop Scan. 1990; 61: 546–548. https://doi.org/10.3109/17453679008993579

Szigeti *et al. BMC Medical Imaging* (2016) 16:14
DOI 10.1186/s12880-016-0118-z

BMC Medical Imaging

TECHNICAL ADVANCE Open Access

Radiomics-based differentiation of lung disease models generated by polluted air based on X-ray computed tomography data

Krisztián Szigeti[1*], Tibor Szabó[2^], Csaba Korom[3], Ilona Czibak[2], Ildikó Horváth[1], Dániel S. Veres[1], Zoltán Gyöngyi[4], Kinga Karlinger[3], Ralf Bergmann[5], Márta Pócsik[2], Ferenc Budán[4,6] and Domokos Máthé[1,2]

Abstract

Background: Lung diseases (resulting from air pollution) require a widely accessible method for risk estimation and early diagnosis to ensure proper and responsive treatment. Radiomics-based fractal dimension analysis of X-ray computed tomography attenuation patterns in chest voxels of mice exposed to different air polluting agents was performed to model early stages of disease and establish differential diagnosis.

Methods: To model different types of air pollution, BALBc/ByJ mouse groups were exposed to cigarette smoke combined with ozone, sulphur dioxide gas and a control group was established. Two weeks after exposure, the frequency distributions of image voxel attenuation data were evaluated. Specific cut-off ranges were defined to group voxels by attenuation. Cut-off ranges were binarized and their spatial pattern was associated with calculated fractal dimension, then abstracted by the fractal dimension – cut-off range mathematical function. Nonparametric Kruskal-Wallis (KW) and Mann–Whitney post hoc (MWph) tests were used.

Results: Each cut-off range versus fractal dimension function plot was found to contain two distinctive Gaussian curves. The ratios of the Gaussian curve parameters are considerably significant and are statistically distinguishable within the three exposure groups.

Conclusions: A new radiomics evaluation method was established based on analysis of the fractal dimension of chest X-ray computed tomography data segments. The specific attenuation patterns calculated utilizing our method may diagnose and monitor certain lung diseases, such as chronic obstructive pulmonary disease (COPD), asthma, tuberculosis or lung carcinomas.

Keywords: Fractal dimension, Radiomics, In vivo micro-CT, Air pollution, Lung disease

Background

"Radiomics" is an approach currently recognized in biomedical image analysis as a tool to define a potentially diverse array of meta-data obtained from images using quantitative radiology image analytics. Some well-selected features of these meta-data can be informative of the health status of the imaged organ system and impact therapy decisions. Such therapy decisions are best taken early in the course of disease. Early therapy decisions have tremendous impact on quality of life in pulmonary diseases.

Fractals are often used to characterize non-Euclidean structures in biology [1]. Utilizing the scaling factor of statistically self-similar and non-overlapping subsets, fractal dimension can be computed [2] providing relevant information describing a structure's complexity and homogeneity [3]. Fractal dimension represents, with certain limitations, the "less or more branching nature" of structures [4, 5] including the respiratory organ [6].

---

* Correspondence: szigeti.krisztian@med.semmelweis-univ.hu
^Deceased
[1]Department of Biophysics and Radiation Biology, Semmelweis University, Tűzoltó utca 37-47, Budapest H-1094, Hungary
Full list of author information is available at the end of the article

We sought to implement a fractal-based radiomics approach to X-ray computed tomography attenuation data without respiratory gating thereby averting the risk of losing relevant information. Analysis of fractal dimensions in specially binned non-gated X-ray computed tomography image patterns has been the method of our choice.

The currently accepted method of analysing pulmonary fractal dimensions of X-ray computed tomography attenuation data usually consists of segmenting parts of the lung such as the alveolar respiratory units, or pulmonary arteries and veins [7–10]. Al-Kadi and Watson [2] distinguished tumours and blood vessels based on their X-ray attenuation differences (using contrast material) to perform fractal dimension analysis on the image segments. The usually applied methods therefore provide the reader with a fractal dimension value for each of the tissue component segments of lung images. A usual outcome measure e.g. is the fractal dimension of lung arterial vasculature.

Our approach to radiomics has been greatly different from simply calculating fractal dimensions of segmented pulmonary tissue components ("dissected" vessels, bronchi etc.). The examination of fractal dimensions of ideally selected attenuation ranges in relative Hounsfield units (HU) may provide the foundation towards discovering additional hidden tissue features in integrative patterns of lung images instead. These fractal dimension calculations may perhaps detect small scale tissue alterations such as those caused by harmful environmental conditions. Our objective was to unveil possible correlations between air pollutant categories and specific features or patterns of damaged lungs. These features of small magnitude might not be evident in either custom visual X-ray computed tomography image analysis or in the calculation of segmented pulmonary tissue fractal dimensions.

We aimed at distinguishing between different air pollutant effects on the lungs via a radiomic approach with a clinically translatable mathematical algorithm. We preferred using non-gated X-ray computed tomography data. Non-gated data acquisition still contains effects of e.g. hindered chest or lung motion. In our analysis we intended to examine data features reflecting disease-related changes also in lung organ movements rather than anatomical relationships. Thus in our analysis method presented here simple non-gated X-ray computed tomography mouse chest scans have been acquired and evaluated by the calculation of fractal dimension of binary images. We binned voxel sets from each mouse chest X-ray computed tomography volume into numerous attenuation ranges in our study [1, 11], instead of pulmonary tissue-based image segmentation. Additionally we also averted the use of any contrast agent.

Generally speaking, (both in the "classic" and in our novel method), the result of fractal dimension calculation is a number corresponding to how often examined structures (dissected arteries and veins in "classical" methods and voxel 3D patterns with specific attenuation values in our approach) branch and/or fill the space within the chest. However, in our novel approach, the fractal dimension calculation method examines and depicts integrative binary images of lung voxels which are selected according to their attenuation values. We then aimed at the application of our algorithm to discriminate among groups of mice treated with different air pollutants in an early phase of their respective disease models.

Methods

Ethics Statement

The animal experiment was reviewed and approved by the local authorities (Committee on the Ethics of Animal Experiments of Semmelweis University, permit number: PMK ÉBÁI-XIV-I-001/29-7/2012) according to Hungarian animal protection laws in accordance with EU guidelines.

Experimental animals

Three groups of BALBc/ByJ female mice (6–8 weeks old, 18–22 g) were used in the context of our current research. Their exposure was performed in a plexiglass inhalator chamber (30 cm × 30 cm × 50 cm). One group ($n = 5$) was treated with inhalation of sulphur dioxide (SO_2) gas 2 % v/v (SDO group). A second group ($n = 5$) was treated with air diluted, fresh mainstream cigarette smoke from '3R4F' Reference Cigarettes (Kentucky Tobacco Research & Development Center, USA) mixed with ozone-air gas mixture (50 mg/h, 3.7 l/min dilution with air; SAO group). Cigarettes with a shortened filter only (approx. 2 mm) were smoked according to our protocol (1 puff/9 s of 3 s duration and 40 mL volume). The SAO group first received one 20 min long exposure, followed by two 20 min long exposures, and lastly, three 20 min long exposures on the additional remaining days. A control group ($n = 6$) was also used, treated with the inhalation of filtered and humidified (30–40 %), air under identical conditions (CON group). Treatment duration was 14 days, and then imaging was carried out within all groups. An untreated BALB/CyJ female mouse (Janvier, France) was imaged too, in serving the purpose of representation of the attenuation profile of the chest (Fig. 1).

In vivo imaging

X-ray computed tomography information was collected using a NanoX-CT (Mediso Ltd, Hungary) cone-beam in vivo micro-CT imaging system (8 W power of X-ray source, 55 kV source voltage, 3.6x zoom) without using contrast material. It is important to emphasize the

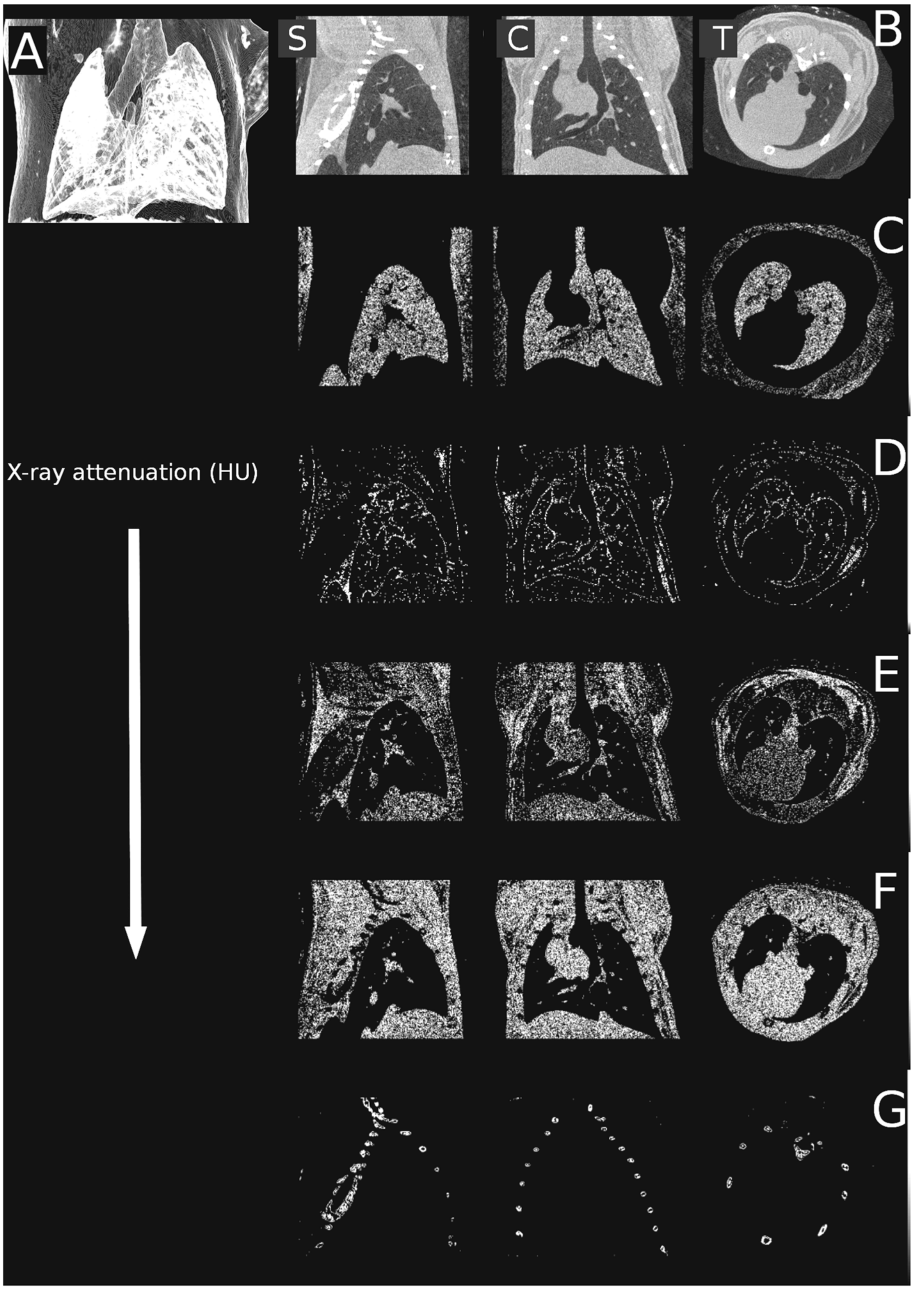

Fig. 1 The reconstruction of the lungs of an untreated mouse shown with the sole intent of representing the attenuation profile of the chest. Sagittal (left **b**), coronal (center **b**), transaxial (right **b**) planes and minimum intensity projection (**a**). Certain attenuation ranges were abstracted from these slices in sagittal, coronal and transaxial planes. **c** −700 – -400 relative HU (lung parenchyma), (**d**): −100 – +200 relative HU (pleura, endothoracic fascia, epipleural fat and interlobar fissures), (**e**): +200 – +500 relative HU (respiratory- and heart muscles, diaphragm), (**f**): +500 – +800 relative HU (blood inside the vessels, aorta and heart, lymphatic fluid and interlobar fissures), and (**g**): +1400 – +3800 relative HU (bones)

physics of cone-beam X-ray computed tomography acquisitions which represents specific technical considerations beyond the scope of our current paper and may distort the direct comparison of attenuation values of the same organs measured with other detection techniques, such as those applied in clinical slice-based X-ray computed tomography systems. Therefore, attenuation values are presented in relative Hounsfield units.

Reconstruction algorithm (Mediso Ltd.) utilizing the Feldkamp-filtered back projection was run on a 64 bit graphics processing unit (GPU). The reconstructed voxel sizes were 54 × 54 × 54 μm in one 370 × 370 × 370 voxel matrix, as region of interest (ROI) following our image acquisition. During data acquisition animals were constantly anaesthetized using a mixture of 2.5 % isoflurane and medical air, and their body temperature was maintained at 38 C. One image acquisition took 4.5 min. Non-respiration-gated data sets were acquired and further analysed.

Fan-beam technology, used earlier and extensively within clinical practice, has today largely been replaced by multislice detector technology. As a result, the difference between pre-clinical and clinical instruments is quickly disappearing and clinical systems are gradually becoming similar to cone-beam computer tomography instruments.

Sensitivity in small animal imaging may be worse when compared to the human counterpart. Voxel size is one tenth or twentieth of the human voxel size, and so the signal-to-noise ratio could be worse (as this ratio is inversely proportional to the third power of voxel volume), however, the measurement time is much longer. In summary, signal-to-noise ratio is better in human measurements, meaning our method will have an increased sensitivity when applied to human cases.

Evaluation of X-ray attenuation histograms

In the first step, our algorithm segmented the acquired 3D X-ray computed tomography volume reconstructions to contain only the whole lung volumes and to automatically distinguish between the lung tissue, chest bones and other tissues. The attenuation values of lung voxels were represented in a frequency distribution function, commonly referred to as a histogram [12] (data not shown). In the next step of evaluation, Gaussian curves were fitted by a minimum square algorithm (Gnuplot 4.4), featuring height, width and position. We calculated the means and standard deviations of positions and widths of the Gaussian curves of all examined groups (Fig. 2). The height is not presented on Fig. 2 as this parameter is dependent on width and area under histogram by definition.

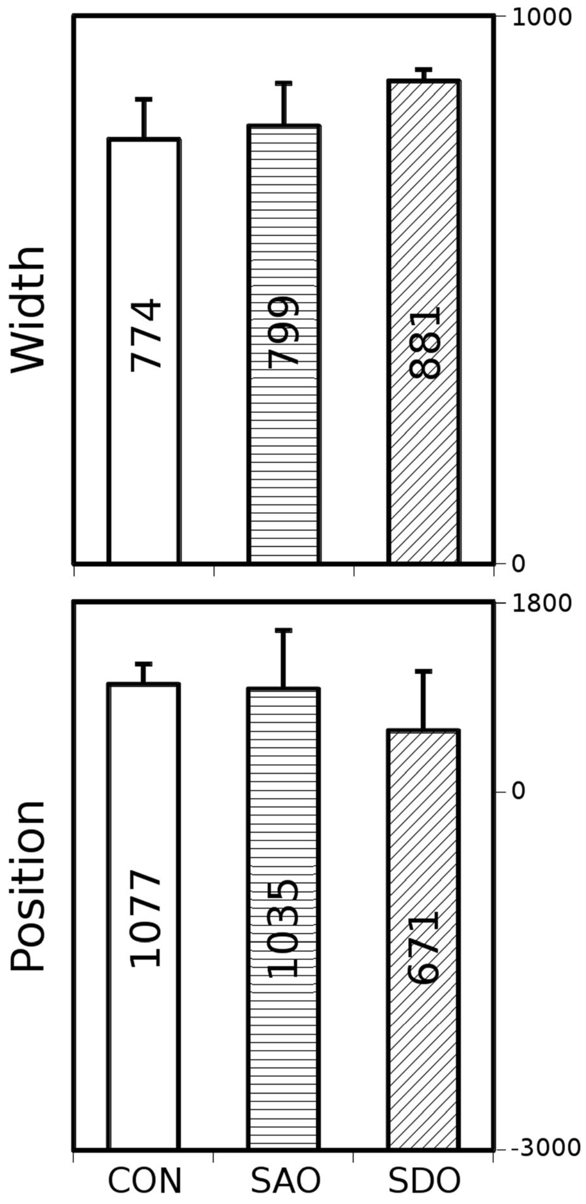

Fig. 2 Width and position parameters (mean, SD) of attenuation histograms. CON, SAO, SDO groups

Characterization by fractal dimension analysis of voxels of various attenuation ranges

Final data analysis was performed in five steps (Fig. 3). The entire attenuation range of the reconstructed chest area of animals was divided into 100 distinct cut-off ranges. Once the attenuation value of a given voxel was within a certain cut-off range, the voxel was represented by "1", or otherwise, "0". This generated a binary image. Each such derived binary pattern was then associated with a calculated fractal dimension via box-counting algorithm [13]. The lung morphology was quantified by plotting the fractal dimension of all cut-off ranges in each given X-ray computed tomography 3D attenuation map. This plot is defined as the fractal dimension - cut-off range function.

Here we present the exact details of the mentioned five steps of data analysis with the purpose of demonstrating how the cut-off range associated fractal dimension data were achieved (Fig. 3).

Step 1. The whole attenuation range in the experiments was between −3,000 and +10,000 relative HU. The 100 distinct ranges of attenuation values were chosen by the Freedman-Diaconis rule [14]. A chosen range is defined mathematically as the

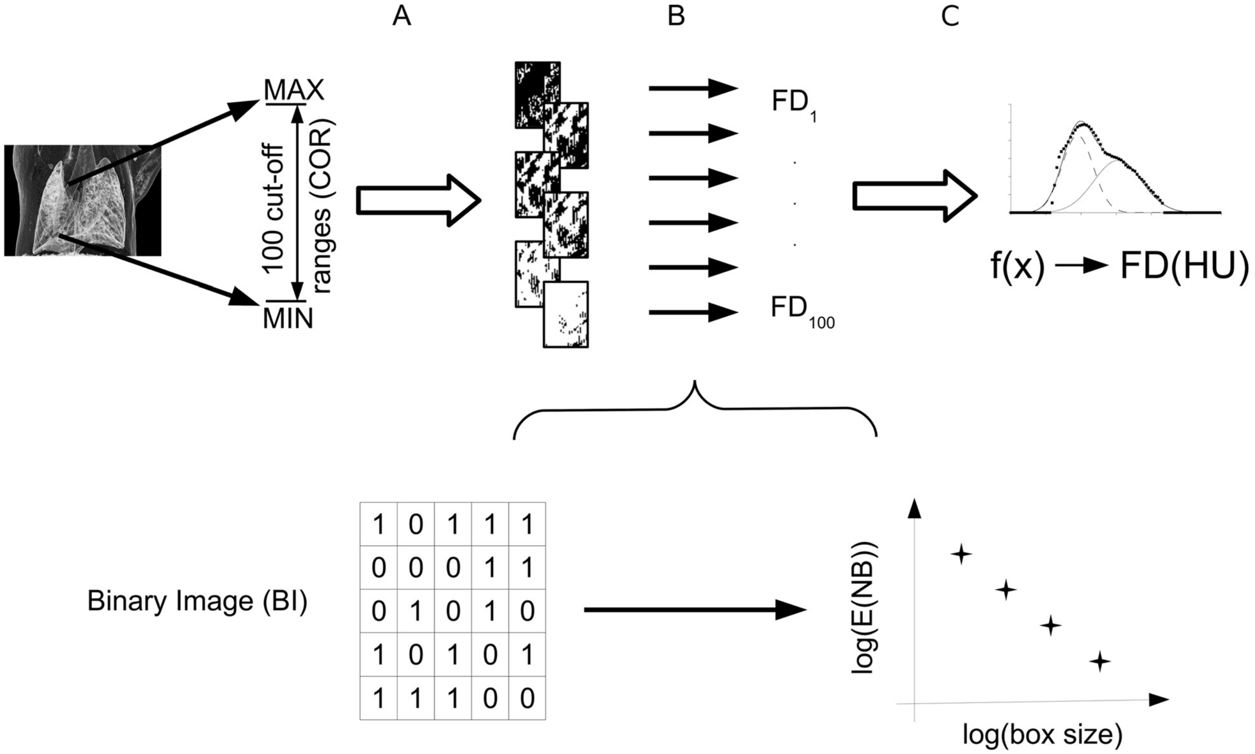

Fig. 3 Representation of the five steps of data analysis. **a**: The entire attenuation range of the reconstructed chest area of animals was divided into 100 distinct cut-off ranges (Step 1). **b**: Binary images are generated (Step 2 and 3) and each such derived binary pattern was next associated with a calculated fractal dimension via box-counting algorithms (Step 4). **c**: The fractal dimension – cut-off range function plot (Step 5)

standard cut-off range. Certain attenuation values ranging between the chosen higher and lower value were ranked into one cut-off range. The 100 cut-off ranges involved the whole scale of the voxel attenuations of all scans and one cut-off range contained 130 relative HU.

Step 2. The X-ray computed tomography images were partitioned into cubic voxels (size: 54 μm in a 370 × 370 × 370 voxel matrix). When the attenuation value of a given voxel was inside a certain cut-off range, then that voxel was associated with "1", or otherwise with "0" in the representation of the cut-off range.

Step 3. This association step was repeated which resulted in a pattern of voxels with "1" and "0" for every cut-off range. These patterns as binary images were used in the next steps. The 100 binary images were derived from 100 previously defined cut-off ranges.

Step 4. The box counting algorithm [13] was used to calculate the fractal dimension number associated with each binary image. See additional details below in the sub-steps labelled a through d.

Sub-step a) In this box-counting algorithm, the length of cubic boxes varied from 1 to 100 voxels. A given box was shifted from one position to another without overlapping in a certain binary image. The number of boxes containing at least one voxel with value "1" was summarized. Thereby, a number was calculated defined as the number of boxes of a given side length (NB).

Sub-step b) The previous sub-step a) was repeated including the difference that the boxes are overlapped. Thus, NB results were produced derived from the shifted overlapped positions. A certain box size in a certain binary image produced two different NB results (from overlapping and non-overlapping boxes). From these two NBs, an average (E(NB)) was calculated and that value was used in further evaluation.

Sub-step c) For each box size, both the a and b sub-steps were repeated. E(NB) was represented as the function of the box size in a certain binary image.

Sub-step d) To determine fractal dimension, the function from sub-step c) was fitted by a power function. The exponent of the power law is the fractal dimension. To each binary image, a fractal dimension number was ordered and calculated utilizing this method.

Step 5. In this step, the cut-off ranges were associated with the calculated fractal dimension. At both the very high and very low cut-off range values, the fractal dimension number is zero, while near the middle values of cut-off ranges the associated fractal dimension number becomes nearly maximal.

The resulting fractal dimension - cut-off range function was fitted by two Gaussian curves (Gaussian curve "A" and "B") using the so-called "least box square" algorithm. The outputs of our algorithm, the height, width and position parameters of these fitted "A" and "B" Gaussian curves, were calculated for all animals (Table 1). Lists these numerical features of the Gaussian curves for every group based on Additional file 1 (supporting data). The lungs of all three groups, SDO, SAO and CON, were characterized by these parameters (Fig. 4).

Lastly, to further attempt significant discrimination of the groups, ratios of all three mean parameters derived from both "A" and "B" Gaussian curves were calculated. The C insets represent the ratios of "A" parameters divided by "B" parameters (where a certain "C" parameter is calculated by dividing the "A" parameter of a given group by the "B" parameter of the same group) (Fig. 5).

These steps were repeated to evaluate the images of each animal.

Statistical analysis

Statistical analysis was performed using the nonparametric Kruskal-Wallis (KW) test for fitted parameters of groups (STATISTICA 7.0, Statsoft Inc., USA). Differences between all groups were evaluated by the Mann–Whitney post hoc (MWph) test (Figs. 2 and 5).

Table 1 Contains averages and standard deviations of all fitted parameters for all groups of animals

Average	SDO	SAO	CON
Height A	2,161	2,231	2,291
Height B	1,725	1,376	1,276
Position A	181	628	735
Position B	3951	3473	3776
Width A	1133	1036	1086
Width B	2496	1630	1562
STD			
Height A	0,049	0,104	0,042
Height B	0,080	0,063	0,090
Position A	386	540	217
Position B	110	647	277
Width A	61	165	169
Width B	161	169	135

A chi-square test was used to test the reliability ($p < 0.05$) of fit of the histogram and the fractal dimension, or the cut-off range function (either fitted with one single or two independent Gaussian curves).

Results

The mean values of width and position of the voxel density histograms demonstrate no significant differences between the three groups (Fig. 2).

The fractal dimension - cut-off range functions were evaluated by fitting them with Gaussian curves "A" and "B" (Fig. 4). These functions can be characterized by height, maximum position and width of the peak. The means of height, width and position of the "A" curve of the CON group do not differ significantly when compared to the SDO or the SAO group. The means of height, width and position are unchanged between the SDO and SAO groups, too (Fig. 5a).

The mean of height of "B" curve of the SDO group increased significantly when compared to the CON group (KW $p = 0.002$, MWph $p = 0.036$) and to the SAO group (KW $p = 0.002$, MWph $p = 0.024$), but not significantly when the CON group was compared to the SAO group (Fig. 5b top). The mean of widths of "B" curves of the SDO group increased significantly (KW $p = 0.016$, MWph $p = 0.036$) compared to the CON group, and also significantly when compared to the SAO group (KW $p = 0.016$, MWph $p = 0.024$), but not significantly when the CON group was compared to the SAO group (KW $p = 0.016$, MWph $p = 0.429$) (Fig. 5b middle). The means of maximum positions are not significantly altered between the SDO, SAO and CON groups (Fig. 5b bottom).

The difference between the ratios of height is significant if the SDO group is compared to the CON group (KW $p = 0.005$, MWph $p = 0.0357$), if the SDO group is compared to the SAO group (KW $p = 0.005$, MWph $p = 0.024$) and if the SAO group is compared to the CON group (KW $p = 0.005$, MWph $p = 0.042$) (Fig. 5c top).

The ratios of width of the SDO and CON groups (KW $p = 0.021$, MWph $p = 0.036$) and the SDO and SAO groups (KW $p = 0.021$, MWph $p = 0.024$) demonstrate a slight but significant difference (Fig. 5c middle), however, the difference between the SAO and CON groups is not significant.

Discussion

Differences between parameters based on the relative HU–frequency histograms of the animals in the three groups, i.e. the differences between mean maximum positions and widths (Fig. 2) could be neither the basis of detection of an altered lung structure nor the categorization

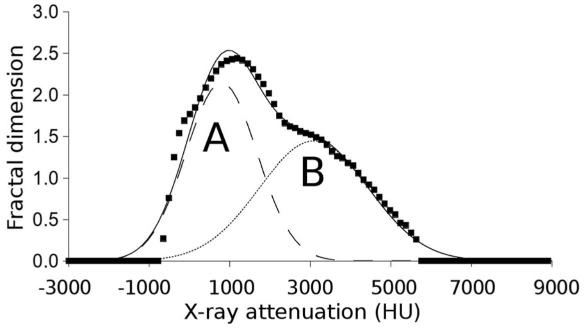

Fig. 4 The fractal dimension – cut-off range function fitted by Gaussian curves "**a**" and "**b**"

of air pollution exposure. Either the absence of gating or the reduced period of mouse model symptom production was likely the reason. Indeed, Sasaki et al. (2015) too could not distinguish the effect of cigarette smoke on lung tissue attenuation in comparison to the control using X-ray computed tomography with gating [15]. However, interestingly enough, a number of differences could be shown using our novel radiomics analysis method.

In our opinion, there are distinctly altered tissue features with respectively changed attenuation patterns in the different mouse models of air pollution related disease. However, the readout of these changes necessitates subtle differentiation and radiomics analysis methods in early phases of lung harm when symptoms are yet considerably subtle.

Severe lung diseases alter the inhalatory and exhalatory movements and these changes can be detected even in mild cases or after relatively short exposure to air pollutants (e.g., the slower exhalation in COPD is evident) [16, 17]. This may be paradoxically advantageous in our approach and likely will help in discerning exposure sources. The hindered motion in the smoke/air and sulphur dioxide groups presumably decreases or even negates spatial and temporal overlapping of different tissues in the same voxel caused by respiratory movement and finally contributes to the mentioned increase of width parameter in the exposed groups. This change in motion dynamics (probably due to inflammation, mucus build-up and entrapped air bubbles) may be an important part of the diagnosis and it is ignored when using respiratory gating. Notably, this finding suggests the fractal dimension- cut-off range function derived radiomic data might unveil some pathologic changes in lung diseases [3, 18]. Possibly the onset of disease as a result of exposure to air pollution could also be observed with our data analysis method.

The Gaussian curves of Fig. 5 display a different pattern of respiratory pulmonary motion in the exposed animals, possibly due to an increase in lung stiffness caused by pollutants.

The height of Gauss curve B is significantly increased in the SDO group compared to the other two groups (Fig. 5b top). We infer this change is attributable to the hindered motion of inflamed tissue.

Sulphurous gases are irritants and induce inflammation, bronchoconstriction and bronchitis resulting in an increase of mucus [3, 19]. Overproduction of mucus can form plugs which entrap air or temporally and partly obstruct the upper airways [20]. Airway clearance of mucus depends on the interactions between physical properties of the mucous gel, serous fluid content, and ciliary function, in addition to airflow [19]. Wagner et al. (2006) discovered in a Sprague–Dawley rat model that 80 ppm concentration of SO_2 (besides overproduction of mucus) caused epithelial cells to lose their ciliae [21]. Nanosized solid particles originating from fumes tend to accumulate in deeper airways and alveoli [22], as inflammatory agents increase water permeability and dilate cell volume thus thickening airway walls and resulting in the narrowing of the airways (in addition to minor mucus production which cannot be excluded). In our interpretation, this narrowing of the airways causes the different motion dynamics of this group.

The width parameter of the SDO group is significantly increased compared to the other two groups (Fig. 5b center). We believe this change is attributable to the hindered motion of inflamed tissue.

The number of voxels representing thickening airway walls is increased, caused by SO_2 exposure often penetrating into deeper airways and inducing inflammation in the alveoli, leading to the appearance of fluid, derived from necrotic cells [19, 23]. Mucus plugs trap air inside the alveoli and lead to the formation of micro-sized bubbles [24, 25] inside the lung parenchyma. Indeed mucus production is an early response to increased amounts of air pollution [19]. In our interpretation, the increased number of voxels representing thickening airway walls causes the different shape of the fractal dimension - cut-off range function of this group.

Only a slight difference was observed between the means of height of Gaussian curve "B" of SAO and CON groups (Fig. 5b top). In addition to mean values of maximum positions (Fig. 5b bottom), the width parameter of the SAO group was compared to the control group (Fig. 5 middle), however it did not significantly change.

Theoretically speaking, emphysema-diseased areas within the lungs could occur caused by destroyed walls of airways and alveoli [11, 12, 18], however, it appears only in long term experiments [26].

In using the corresponding ratios of parameters of Gaussian curves "A" and "B" (Fig. 5c) and the heights and widths of "B" Gaussian curves (Fig. 5b), all three groups could be distinguished. We believe the difference

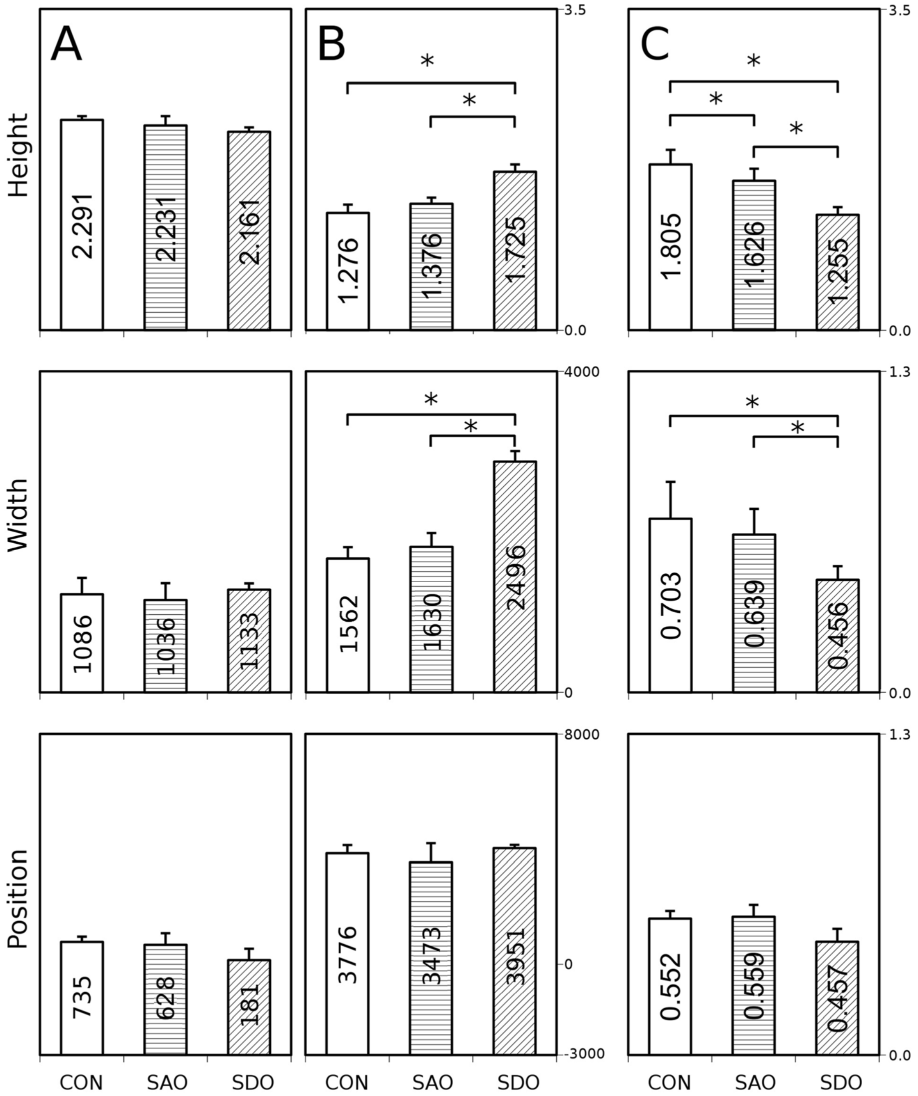

Fig. 5 Calculated height, width and position parameters of the fractal dimension - cut-off range functions. **a**: Height, width and position parameters of Gaussian curve „A" (CON, SDO, SAO groups). **b**: Height, width and position parameters of Gaussian curve „B" (CON, SDO, SAO groups). **c**: The ratios of the relevant parameters of Gaussian curves „A" and „B" (CON, SDO, SAO groups). * $p < 0.05$, Kruskal-Wallis (KW) test with Mann–Whitney post hoc (MWph) test

between the ratios of parameters refers to the different proportion of various kinds of tissue damage caused by different air pollution agents.

The proportion of tissue alterations has a specific pattern in lung diseases of different origin. Altered tissue (e.g., increased mucus production in one model or increased presence of tissue microbubbles in another) was explored.

The mechanism of these changes affecting the respiratory movement remains unclear and warrants further research.

Data acquired in our study (Fig. 5b, c) proved a worthy basis for differentiating specific air pollution caused lung changes in the early stage by direct fractal dimension - cut-off range function pattern analysis. It could be hypothesized that molecular features and presence of mucus in smaller airways [19] and inflammation profile of lung tissues [27] contribute to our fractal dimension analysis-based results. In reference to published literature [19, 28], we postulate that the fractal dimension - cut-off range function calculated with our method may be used as an imaging biomarker. It could be effectively converted to both preclinical applications and clinical use in humans, ideally providing patients the benefit of early warning towards avoiding environmental risks. Additional benefits are expected in the proper treatment at the onset of symptoms of disease, and lastly, to prevent aggravation of disease and exacerbation of COPD and/or asthma bronchiale symptoms. Here, we highlight the importance of length of smoke exposure and genetic susceptibility [28] to emphysema [26], which may later develop and will be reflected in the reported imaging biomarker parameters [3, 18].

The radiomic analysis of the fractal dimension - cut-off range function may be useful in early diagnosis of both exposure to air pollution and lung diseases (such as COPD or asthma), containing information about both the molecular features and patterns of mucus in smaller airways [19] and the inflammation profiles of lung tissues [27]. We propose an increase in the number of structurally quantitative imaging biomarker research studies, towards early detection and follow-up of therapy of other pulmonary diseases, for example, cystic fibrosis, lung carcinomas [3] or tuberculosis [29].

In translational research, our most important goal is to develop methods in animal models which later may be used in clinical practice. In the case of our paper, the translatability of the method is dependent upon three aspects of it. The first is the usability of the algorithm in clinical practice, the second is the relation between anatomy sizes and reconstruction voxels, and the third is the applicability of the algorithm in clinical protocols.

The algorithm does not use specific data, as it only requires a 3D reconstruction, that is attenuation distribution. These data are also available in the clinical setting, so our algorithm proposed here can also be applied for clinical lung computed tomography volumes.

The human body is about 15–20 times longer than the body of the mouse and there is nearly the same difference between spatial resolution (voxel size in preclinical CT is 50 μm and in clinical CT is 500–750 μm). Generally speaking, anatomy size and voxel size change proportionally. Because of the partial-volume effect, though, true resolution does not reach voxel size calculated from reconstruction. It is important to note that the size of alveoli is invariable between species and is around 200 μm. Consequently, neither the pre-clinical nor the clinical instrument can visualize individual alveoli with suitable resolution, but in the case of the pre-clinical instrument, we see one alveolus in the adjacent voxels, whereas in case of the clinical instrument, we see more than one alveoli in one voxel.

Practically speaking, the proposed algorithm can be applied in the clinics and it is not necessary to change protocols, since the usual examinations and unchanged data acquisition chain should be followed by this new "off-line" analysis.

In summary, the use of the algorithm will be self-evident in clinical practice. Naturally, its diagnostic effectiveness needs to be assessed meticulously throughout different diseases.

Conclusions

We discovered a novel diagnostic and disease characterization method providing results within a remarkably short disease model production time compared to the former 8–24 weeks needed to produce detectable lung tissue changes as described in published literature [30]. Additionally, as our method does not apply gating, it may contribute to the simplified and more cost-effective (through higher throughput) data analysis utilizing simple X-ray computed tomography scans in mouse experimental models. The implementation of our data analysis is straightforward and applicable in clinical image data sets and does not require additional hardware. As the early diagnostic potential of COPD-related lung and airway changes was shown here in data containing approximately clinical levels of noise, we remain convinced the translation and validation of our algorithm and data analysis in human clinical trials is warranted [3].

Additional file

Additional file 1: Lists of the numerical features of the Gaussian curves for every mouse. (DOC 36 kb)

Competing interests

The authors hereby declare they have no competing interests. Tibor Szabó, Ilona Czibak, Márta Pócsik, and Domokos Máthé are employees of CROmed Translational Research Centers. CROmed Translational Research Centers does not have any financial or non-financial interest in the subject matter or materials discussed in this manuscript. Ferenc Budán is an employee/stakeholder of MedProDevelop Kft that has no financial or non-financial interest in the subject matter or materials discussed in this manuscript.

Authors' contributions

DM and TS designed the study; TS, IC, DM and IH did the preclinical imaging work; CK, DSV and FB analyzed the data; KS takes responsibility for the integrity of the data and the accuracy of the data analysis; DM, KS, FB, ZG and MP wrote the paper; KK and RB contributed expert advice and valuable insight. All authors read and approved the final manuscript.

Acknowledgements

Miklós Kellermayer and Jon Marquette are gratefully acknowledged for providing support. The technical help from Mediso's Evaluation Software Team especially László Papp is gratefully acknowledged.

Author details

[1]Department of Biophysics and Radiation Biology, Semmelweis University, Tűzoltó utca 37-47, Budapest H-1094, Hungary. [2]CROmed Translational Research Centers Ltd., Baross utca 91-95, Budapest H-1047, Hungary. [3]Department of Radiology and Oncotherapy, Semmelweis University, Üllői út 78/A, Budapest H-1082, Hungary. [4]Department of Public Health Medicine, University of Pécs, Szigeti út 12, Pécs H-7624, Hungary. [5]Institute of Radiopharmaceutical Cancer Research, Helmholtz-Zentrum Dresden-Rossendorf, Dresden D-01314, Germany. [6]MedProDevelop Kft, Irgalmasok utcája 16, Pécs H-7621, Hungary.

Received: 1 October 2015 Accepted: 1 February 2016

References

1. Mandelbrot BB, Blumen A. Fractal Geometry: What is it, and What Does it do? Proc R Soc A. 1989;423:3–16.

2. Al-Kadi OS, Watson D. Texture analysis of aggressive and nonaggressive lung tumor CE CT images. IEEE Trans Biomed Eng. 2008;55(7):1822–30.
3. van Rikxoort EM, van Ginneken B. Automated segmentation of pulmonary structures in thoracic computed tomography scans: a review. Phys Med Biol. 2013;58:R187–220.
4. Smith TG, Lange GD, Marks WB. Fractal methods and results in cellular morphology - Dimensions, lacunarity and multifractals. J Neurosci Methods. 1996;69(2):123–36.
5. Helmberger M, Pienn M, Urschler M, Kullnig P, Stollberger R, Kovacs G, et al. Quantification of tortuosity and fractal dimension of the lung vessels in pulmonary hypertension patients. PLoS One. 2014;9(1):e87515.
6. Shlesinger MF, West BJ. Complex fractal dimension of the bronchial tree. Phys Rev Lett. 1991;67(15):2106–8.
7. Keller BM, Reeves AP, Henschke CI, Yankelevitz DF. Multivariate Compensation of Quantitative Pulmonary Emphysema Metric Variation from Low-Dose. Whole-Lung CT Scans Am J Roentgenol. 2011;197(3):495–502.
8. Huo Y, Choy JS, Wischgoll T, Luo T, Teague SD, Bhatt DL, et al. Computed tomography-based diagnosis of diffuse compensatory enlargement of coronary arteries using scaling power laws. J R Soc Interface. 2013;10(81):20121015.
9. Gould DJ, Vadakkan TJ, Poche RA, Dickinson ME. Multifractal and Lacunarity Analysis of Microvascular Morphology and Remodeling. Microcirculation. 2011;18(2):136–51.
10. Glenny RW. Emergence of matched airway and vascular trees from fractal rules. J Appl Physiol. 2011;110(4):1119–29.
11. Wright JL, Cosio M, Churg A. Animal models of chronic obstructive pulmonary disease. Am J Physiol Lung Cell Mol Physiol. 2008;295(1):1–15.
12. Smith Jr TG, Lange GD, Marks WB. Fractal methods and results in cellular morphology — dimensions, lacunarity and multifractals. J Neurosci Methods. 1996;69:123–36.
13. Freedman D, Diaconis P. On the histogram as a density estimator: L2 theory. Zeitschrift für Wahrscheinlichkeitstheorie und Verwandte Gebiete. 1981;57:453–76.
14. Sasaki M, Chubachi S, Kameyama N, Sato M, Haraguchi M, Miyazaki M, et al. Evaluation of cigarette smoke-induced emphysema in mice using quantitative micro-computed tomography. Am J Physiol Lung Cell Mol Physiol. 2015;308(10):1039–45.
15. Tantisuwat A, Thaveeratitham P. Effects of Smoking on Chest Expansion, Lung Function, and Respiratory Muscle Strength of Youths. J Phys Ther Sci. 2014;26:167–70.
16. Gagnon P, Guenette JA, Daniel L, Louis L, Vincent M, François M, et al. Pathogenesis of hyperinflation in chronic obstructive pulmonary disease. Int J of Crohn Obstruct Pulmon Dist. 2014;9:187–201.
17. Nagao M, Murase K. Measurement of heterogeneous distribution on Technegas SPECT images by three-dimensional fractal analysis. Ann Nucl Med. 2002;16(6):369–76.
18. Williams OW, Sharafkhaneh A, Kim V, Dickey BF, Evans CM. Airway mucus: From production to secretion. Am J Respir Cell Mol Biol. 2006;34(5):527–36.
19. Kim WD. Lung mucus: A clinician's view. Eur Respir J. 1997;10(8):1914–7.
20. Wagner U, Staats P, Fehmann H-C, Fischer A, Welte T, Groneberg DA. Analysis of airway secretions in a model of sulfur dioxide induced chronic obstructive pulmonary disease (COPD). J Occup Med Toxicol. 2006;1:12.
21. van Dijk WD, Gopal S, Scheepers PT. Nanoparticles in cigarette smoke; real-time undiluted measurements by a scanning mobility particle sizer. Anal Bioanal Chem. 2001;399:3573–8.
22. Castañer E, Gallardo X, Pallardó Y, Branera J, Cabezuelo MA, Mata JM. Diseases affecting the peribronchovascular interstitium: CT findings and pathologic correlation. Curr Probl Diagn Radiol. 2005;34(2):63–75.
23. Bossé Y, Riesenfeld EP, Paré PD, Irvin CG. It's not all smooth muscle: non-smooth-muscle elements in control of resistance to airflow. Annu Rev Physiol. 2010;72:437–62.
24. Moldoveanu B, Otmishi P, Jani P, Walker J, Sarmiento X, Guardiola J, et al. Inflammatory mechanisms in the lung. J Inflamm Res. 2009;2:1–11.
25. Maeno T, Houghton AM, Quintero PA, Grumelli S, Owen CA, Shapiro SD. CD8+ T Cells are required for inflammation and destruction in cigarette smoke-induced emphysema in mice. J Immunol. 2007;178(12):8090–6.
26. Jeffery PK. Structural and inflammatory changes in COPD: a comparison with asthma. Thorax. 1998;53(2):129–36.
27. Churg A, Cosio M, Wright JL. Mechanisms of cigarette smoke-induced COPD: insights from animal models. Am J Physiol Lung Cell Mol Physiol. 2008;294(4):612–31.
28. Chen RY, Dodd LE, Lee M, Paripati P, Hammoud DA, Mountz JM, et al. PET/CT imaging correlates with treatment outcome in patients with multidrug-resistant tuberculosis. Sci Transl Med. 2014;6(265):166.
29. Jobse BN, Rhem RG, Wang IQ, Counter WB, Stämpfli MR, Labiris NR. Detection of lung dysfunction using ventilation and perfusion SPECT in a mouse model of chronic cigarette smoke exposure. J Nucl Med. 2013;54(4):616–23.
30. Beckett EL, Stevens RL, Jarnicki AG, Kim RY, Hanish I, Hansbro NG, et al. A new short-term mouse model of chronic obstructive pulmonary disease identifies a role for mast cell tryptase in pathogenesis. J Allergy Clin Immunol. 2013;131(3):752–62.

RESEARCH ARTICLE

Longitudinal In Vivo MR Imaging of Live Earthworms

JOURNAL OF EXPERIMENTAL ZOOLOGY
PART A
ECOLOGICAL GENETICS AND PHYSIOLOGY
A Journal of Integrative Biology

FERENC BUDÁN[1], NOÉMI KOVÁCS[1], PÉTER ENGELMANN[2], ILDIKÓ HORVÁTH[3], DÁNIEL S. VERES[3], PÉTER NÉMETH[2], KRISZTIÁN SZIGETI[3]*, AND DOMOKOS MÁTHÉ[1]

[1]CROmed, Translational Research Centers, Budapest, Baross utca, Hungary
[2]Department of Immunology and Biotechnology, Clinical Center, University of Pécs, Pécs, Szigeti út, Hungary
[3]Department of Biophysics and Radiation Biology, Semmelweis University, Budapest, Tűzoltó utca, Hungary

ABSTRACT

Earthworm (*Oligochaeta*, *Lumbricidae*) species are used widely in eco-toxicological tests especially with contaminated soils. These long-term tests are reliable, but a high sample size is needed. Magnetic resonance imaging (MRI) can produce fast, robust, sensitive, and longitudinal morphological results using a small sample size. Performing longitudinal in vivo examinations of earthworms using MRI requires the need for anesthetics to completely avoid earthworm's moving. Our goal was to develop a simple and non-invasive method to anesthetize earthworms for in vivo longitudinal imaging studies. We investigated a number of different anesthesia methods and found that propan-2-ol and its vapor was optimal. We used a commercial sequential nanoScan® PET/MRI system (Mediso Ltd, Hungary, Budapest) to explore feasibility of MR imaging in immobilized earthworms. It was possible to visualize via micro MRI the brain, gastrointestinal tract, seminal vesicles, calciferous gland (Morren gland), and main blood vessels of the circulatory system. Our findings show the possibilities to examine changes in morphology using MRI of certain organs using a reversible, long-term immobilization method. *J. Exp. Zool. 9999A: XX–XX, 2014.* © 2014 Wiley Periodicals, Inc.

J. Exp. Zool.
9999A:1–11, 2014

How to cite this article: Budán F, Kovács N, Engelmann P, Horváth I, Veres DS, Németh P, Szigeti K, Máthé D. 2014. Longitudinal in vivo MR imaging of live earthworms. J. Exp. Zool. 9999:1–11.

Soils deliver valuable goods and services such as carbon storage and water filtering. In order to ensure a sustainable environment and society these goods and services need to be maintained (Lavelle et al., 2006; Morvan et al., 2006). Assessment of soil quality, defined as the ability of soils to deliver ecosystem services in a sustainable way (Doran and Parkin, ’94), has become a major research topic in the last two decades (Ruiz et al., 2011). Nevertheless, validated tools to obtain information on degradation and/or remediation of soil properties and functions to inform state agencies, as well as monitoring networks (European Commission, 2006) are needed. To date, soil characterization has generally been based on physical and chemical parameters (Kibblewhite et al., 2008; Morvan et al., 2008). However, soil organisms are known to respond to multiple impacts and to react quickly to natural and anthropic stresses, and could, therefore, be used as early warning indicators (Cortet et al., ’99; Sousa et al., 2006).

Grant sponsor: Medical Faculty Research Foundation; grant sponsor: University of Pécs; grant number: PTE ÁOK-KA 2013/09; grant sponsor: EC-FP7 Transnational Access Grant (QNANO); grant sponsor: János Bolyai Research Foundation of the Hungarian Academy of Sciences.

*Correspondence to: Krisztián Szigeti, H-1094, Budapest, Tűzoltó utca 37-47, Hungary.
E-mail: szigeti.krisztian@med.semmelweis-univ.hu

Received 14 March 2014; Revised 14 June 2014; Accepted 14 June 2014
DOI: 10.1002/jez.1880

Among terrestrial invertebrates, earthworms (*Oligochatea*, *Annelida)* are "keystone" species in soil ecosystems. Earthworms are distributed worldwide, have with a short life cycle and have a wide temperature and moisture tolerance range (Dominguez, 2004). Earthworms are sensitive to metallic pollution, for example, cadmium (can be detected in 0.6 mg/kg in soil, $LC_{50} = 1{,}000$ mg/kg) (Xiaohui et al., 2012) which delays their sexual maturation (Spurgeon and Hopkin, '96), slows down their growth (Spurgeon and Hopkin, '99), modifies enzymatic activities (Łaszczyca et al., 2004), and gene expressions (Ricketts et al., 2004; Brulle et al., 2006, 2007). Earthworms are, therefore, widely used as model organisms for detection of soil pollution. Their direct contact with natural soil pore constituents and soil water makes them ideal for environmental monitoring (Gerencsér et al., 2010). The studies of experimental carcinogen treated earthworms could monitor the effects of certain environmental carcinogens.

Although the current tests are reliable they need a large sample size (8–10 earthworms per sample interval per sample site) (Spurgeon and Hopkin, '98; Gerencsér et al., 2010; Heckmann et al., 2011) and are time consuming. Contrary to that, modern in vivo imaging techniques (e.g., MRI) can produce robust, sensitive and longitudinal results using a small sample size owing to the fact that each animal acts as a control for itself over time. These imaging studies are quick, high throughput (i.e., you can image multiple animals at once) and yield easily repeatable data. Results of MRI ideally could detect early morphological changes.

To the best of our knowledge, this is the first example of in vivo imaging of living earthworms using preclinical MRI. This modality requires the targets to be immobilized at least for 20 min and it is beneficial to avoid invasive immobilization techniques damaging the tissues. Thus, when using in vivo imaging techniques there is an imperative to perform non-invasive immobilization methods with minimal effects of the immobilization technique on the physiology of the animal. In addition, the repeatability of immobilization method is important in order to monitor biological processes and effect of environmental factors in the same living animal over time (Gerencsér et al., 2010). Therefore physical methods such as cooling down the earthworm are not suitable. The applicable immobilization method also needs to avoid disturbing the imaging measurements. Common liquid-state anesthetic agents such as tricaine (trade names: Finquel® or MS-222®) which are potentially capable to enhance immobilization could impair MRI especially if they are in direct contact with the target animal during the scan, because they themselves give contrast in MR. The aforementioned methods usually apply either physical factors like increased pCO_2 or decreased temperature, or they rely on a fluid directly contacting the individual annelid's skin for the period of time of immobilization. Therefore they are not suited for application in MR imaging. For the sake of completeness it is important to mention that fluids in direct contact, but not covering the earthworms body are supposed not to decrease the respiration rate of earthworms, because of body fluids of annelids are abundant with erythrocruorins (Salomon, '41). Erythrocruorins (hemoglobin) are highly cooperative giant extracellular respiratory complexes and they serve the same function as red blood cells. Earthworm hemoglobin is able to bind a great quantity of oxygen (Strand et al., 2004).

Some other reported methods are based on invasive techniques or apply metal ions (e.g., magnesium chlorine) (Lewbart, 2011). While there are some very recent reports on application of pharmaceutical substances, they present results of anesthesia-immobilization times that are too short for any appropriate in vivo imaging study design (Podolak-Machowska et al., 2013).

Our goal was to develop a practically useful method for optimal pre-treatment and immobilization of earthworm for in vivo imaging and then to test this method by MR imaging. The objective was to find a quick, feasible, cost-effective, and simple method to render our results easily reproducible by avoiding possibilities of motion artifacts in MR images. The proper immobilization method for our purpose must completely inhibit even small movements of earthworms and remain totally free of any external motion for a period of at least 20 min, without any motion-based reaction to environmental changes (e.g., light) or stress factors (like a touch). The second important aspect of proper immobilization is that it should be reversible and cause only minimal biologically important effects which could distort the results of imaging biomarker examinations (such an imaging biomarker is exemplified by the size of the gonads).

In our experiments *Eisenia hortensis* M., syn. *E. veneta*, syn., *Dendrobaena veneta* species were used for two reasons: (i) due to their larger size the details in MRI results are increased; and (ii) they are ecologically important in decomposing the soil (Leveque et al., 2013). For optimal MRI image quality, we pre-treated the animals to decrease intestinal soil contents.

MATERIALS AND METHODS

Housing of Earthworms

Earthworms (*Eisenia hortensis* M.) were kept at 20 ± 2°C in plastic boxes (diameter 8.8 cm), with small ventilation holes and ten animals per box. Soil in the boxes was kept moist and contained 30% of farmyard horse manure.

Test for Optimal Pre-Treatment to Decrease Intestinal Soil Contents

We examined the possibility of keeping earthworms alive without earth to empty their intestines. The essence of pre-treatment is that earthworms were kept on Ringer solution instead of earth. Drewes and Pax ('74) developed a pre-treatment Ringer salt solution for earthworms. This Ringer solution was modified and applied in our experiment (for details please see Table 1). The Ringer solution was changed daily. The buffer level in the boxes was sufficiently low to

Table 1. The quantities of compounds used to prepare the special earthworm Ringer solution, based on Drewes and Pax's Ringer, but sulfate ions are replaced with chloride ions in all if the used components.

Component	g/L	Concentration (mmol)
Sodium chloride	4.38	75.00
Potassium chloride	0.30	4.00
Calcium chloride	0.22	2.00
Magnesium chloride	0.10	1.00
Tris	1.21	1.00
Sucrose	7.87	23.00
pH adjusted to 7.4 with HCl		

allow the earthworms to keep contact with air. The sucrose in the Ringer nourished earthworms and the water content kept their body moist. Earthworms were kept in separated boxes and their body mass and the mass of their excrements were monitored daily.

To provide data about the potential effect of a 4-day pre-treatment on the earthworms two groups (n = 10) were examined. In both groups the earthworms were kept in Ringer solution (immersed in 1 mL × 4 mass (g) of the earthworm) in a box (diameter 8.8 cm). To Group A, we also provided a solid polystyrene plate as we wished to test its effect as cover and ground that prevented their bodies to be fully immersed if they moved onto the plate in the box. Group A (n = 10) earthworms were examined in the following way: a polystyrene plate was put into the box (Fig. 1A). Earthworms in the control group B (n = 10) were similarly treated as group A, but group B differed that polystyrene plates were missing (Fig. 1B). Results of group A and B were compared to each other. Other relevant observations were recorded at occurrence. For example, the potential earth content in their intestines were checked visually (earthworms were put before a light source and thus their intestines become transparent).

Tested Methods for Potential Immobilization

The earthworms were considered to be immobilized when they were completely paralyzed and they also not reacted on touching them. The time of immobilization was considered to be the time range from the beginning of the immobilization until the time point when immobilization ceased (e.g., they reacted with moving if their body was touched). We checked their state in each half-minute by smoothly touching them.

Administration of immobilizing pharmaceutical agents (all purchased from Sigma-Aldrich, Hungary, Budapest) was mostly applied in two ways: injection or immersing in aqueous solution of the test animals in 9 cm Petri dishes.

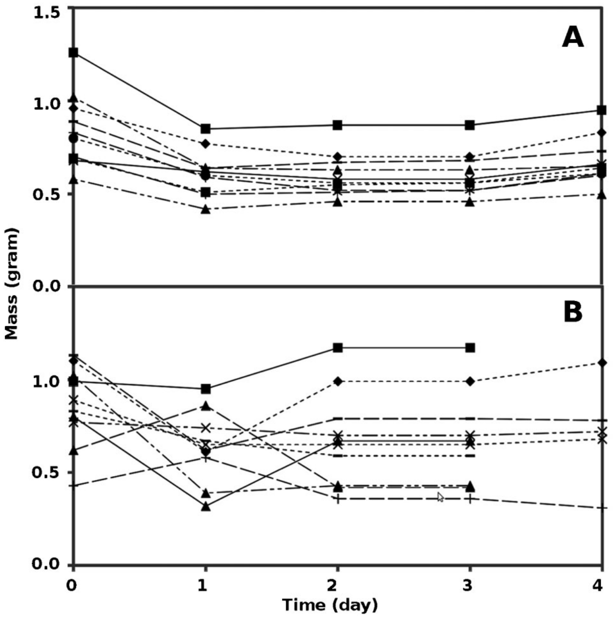

Figure 1. Individual earthworm's body mass (g) alteration caused by keeping them in Ringer solution. (A) Polystyrene plates present (n = 10). (B) Polystyrene plates absent (n = 10).

A method to administrate volatile pharmaceutical materials by inhalation was also investigated. Inhalation experiments with general anesthetics were performed in an in house-prepared airtight box (volume 100 cm^3). Eighty microliters of liquid anesthetics was placed into the box on a cotton bud. The following groups of pharmaceutical agents were tested (please see Tables 2 and 3 for the detailed chemical list and information about quantities): non-depolarizing neuromuscular blockers (NDNBs), parasympatho-mimetics, parasympatho-lythics, inhalational general anesthetics, neurotransmitters, $\alpha 2$ agonists, γ-aminobutyric acid (GABA) agonists, opiates, Na^+ channel blockers, different types of Ca^{2+} channel blockers and alcohols. The following ions were also tested: magnesium ions (Mg^{2+}) derived from magnesium chloride ($MgCl_2$) lithium ions (Li^+) derived from lithium-carbonate (Li_2CO_3), bromide ions (Br^-) derived from potassium-bromide (KBr). Furthermore anthelmintticals known to immobilize targets were tested as well. In another experimental series, the combinations of the above-mentioned agents were used, such as the "classical" combination of widely used agents for anesthetics in vertebrates, ketamine (0.12 mg) and xylazine (0.1 mg), in 50–50 μL Ringer solution (Green et al., '81; Greene and Thurmon, '88).

Ethanol (96.7%) was added into the bath of Ringer solution gradually. (The same modified (Drewes and Pax, '74) Ringer solution was used as by the pre-treatment for MR imaging with the

Table 2. Different agents (purchased from Sigma-Aldrich, Hungary, Budapest) solved in 50 μL Ringer solution and administered to test earthworms using injection and their results.

Compound	Doses	Effect on earthworm	Effect started after the treatment (min)	Duration of the effect
Rocuronium	0.50 mg	i	5 min	2 hr
Cisatracurium	0.10 mg	n	–	–
Physostigmin	0.01 mmol	n	–	–
Neostigmin	0.01 mmol	n	–	–
Glycine	75.0 mg	n	–	–
Fentanyl	0.005 mg	e	5 min	5 min
Atropine	0.005 mg	n	–	–
Magnesium ion	400 mmol/mL	n	–	–
Lithium ion	400 mmol/mL	n	–	–
Bromide ion	400 mmol/mL	n	–	–
Ketamine and xylazine	0.12 mg + 0.1 mg	#	–	–
Sodium-barbithalum	10.0 mg	n	–	–

Note: i, immobilized earthworms; n, not effective (does not cause any visible change in movement); e, excitatory; #, damaged or killed earthworms.

Table 3. Different agents (purchased from Sigma-Aldrich) solved in 10 mL Ringer solution, applied in bath for testing earthworms in Petri dish.

Compound	Doses	Effect on earthworm	Effect started after the treatment (min)	Duration of the effect
Rocuronium	0.40 mg/10 mL	n	–	–
Cisatracurium	0.04 mg/10 mL	n	–	–
Physostigmine	0.01 mmol	n	–	–
Neostigmine	0.01 mmol	n	–	–
Guaiphenesine	24 mg/10 mL	#	–	–
Fentanyl	0.50 mg/10 mL	e	5 min	5 min
Benzocaine	4,000 mg/10 mL suspension	#	–	–
Lidocaine	0.90 mg/10 mL	e	15 min	10 min
Lidocaine	2.50 mg/10 mL	i	5 min	2 + hr
Ketamine	0.45 mg/10 mL	n	–	–
Lamotrigine	50 mg/10 mL	#	–	–
Felodipine	5.00 mg/10 mL	n	–	–
Amiodaron	200 mg/10 mL	n	–	–
Verapamil	80 mg/10 mL	n	–	–
Diltiazem	90 mg/10 mL	#	–	–
Drotaverinum	80 mg/10 mL	#	–	–
Ethanol	8.00%	i	5 min	5 min
Propan-2-ol	4.00%	i	3 min	4 min
Ivermectine	0.60 mg/10 mL	#	–	–
Levamisole	3.50 mg/10 mL	#	–	–
Ketamine and xylazine	0.12 mg + 0.1 mg/10 mL	n	–	–
Propan-2-ol in airtight box	4.00%	i	3 min	3 + hr

Note: i, immobilized earthworms; n, not effective (does not cause any visible change in movement); e, excitatory; #, damaged or killed earthworms.

purpose to avoid soil in the intestines of earthworms.) Animals were kept away from direct contact with 96.7% alcohol. According to Petrics and Larsson ('86), 8% ethanol could be used to anesthetize earthworms. Similarly to ethanol application, we experimented with isopropanol added into the Ringer solution in 7–8 equal boli in each 5 min until 3.5–4.0 V/V % was reached. With careful administration minimal distress was caused to the animals and thereby the excretion of coelomic fluid was avoided. The airtight box tested for the general anesthetics was used to extend the immobilizing effect of alcohols by injecting 10 mL of 30% alcohol into the bottom of the box. An earthworm holder bed placed in a 50 mL Falcon tube was constructed with dual purpose: the first purpose of this holder bed was to keep the experimental animals from sliding inside the Falcon tube. The other goal was to separate animals from alcohol, but in such a manner that the vapor of alcohol was in the same airspace as the animals. Furthermore the box enabled us to move the animals from one desired imaging modality to the other one without the animal position changing related to the imaging bed.

Parameters of MR Imaging

For MRI a commercial small-animal sequential PET/MRI imaging system (nanoScan® PET/MRI, Mediso Ltd) was used applying 1 T permanent magnet, 60 mm diameter transmit/receive volume coil and 450 mT/m gradients. A T1 weighted spoiled gradient echo sequence was applied with three-dimensional acquisition scheme ($7 \times 7\,\text{cm}^2$ field of view in the coronal plane, 0.35 mm isovoxel size, 94 slices, repetition time of 20 msec, echo time of 2.3 msec, dwell time of 20 μsec, flip angle of 25° and 4 averages). To achieve the needed short TE asymmetric echoes were acquired by sampling only the last 75% of the full k-space line. This sequence was selected in order to satisfy two main criteria: Firstly to minimize MRI acquisition time and secondly to achieve a good signal-to noise ratio. Due to the elongated shape of the earthworms one can make the scan even shorter with a rectangular-shaped FOV, when the number of phase encoding steps is reduced without increasing the voxel size. Our scanner is not capable of this and we decided to image more earthworms simultaneously to reach high throughput, increased MR signal and make the most out of a single FOV. Our above mentioned imaging box—made from a Falcon tube—is suitable for the scanning of 3–6 earthworms at the same time. Two separated levels of beds could be fitted into the Falcon tube and on each level 3–3 earthworms can be placed. Three of them are right next to each other and the three others are just above them on the appropriate level of the bed. With this positioning coronal slices (frequency encoding is parallel to the axes of the earthworms) are the most appropriate choice and slice number is set to cover all of the earthworms.

Statistics

Mann–Whitney U-test was used to compare the data between group A and group B. All tests were performed using the Statistical Package for Social Sciences (IBM SPSS Statistics 20.0 software; IBM Corporation, Armonk, NY, USA).

RESULTS

Validation of Pre-Treatment

All earthworms' body masses decreased significantly from the beginning of the experiment until the first day. We also observed that in their body weight and the quantity of excrements decreased significantly in the first day and then only slightly thereafter (Fig. 1A and B). At the third day of the experiment their gastrointestinal tract was considered clean from excrements according to our visual observation. The body masses of *Eisenia hortensis* M. were 1.1 ± 0.3 g in the beginning of the experiment evaluating the pre-treatment.

In both of A and B groups the mass of earthworms decreased (Mann–Whitney, $P < 0.05$) from the beginning of the experiment to test the pre-treatment until the first day. In group A, none of the earthworms showed significant physiological and morphological alterations and their body mass remained near to the body mass measured on the first day until the third day (Mann–Whitney, $P > 0.05$). The body mass of earthworms in group B changed variously and generally strongly. At the fourth day, an increase in body mass was found because their body had begun to swell due to the Ringer solution (Mann–Whitney, $P < 0.01$). All of the earthworms in group A moved under the polystyrene plates each time when they were checked.

According to observations and data about body mass increasing as well (Fig. 1B) in group B some of the earthworms' body begun to swell even at the first day. At the fourth day all of the earthworms were swollen in such a manner that they were considered not to be useful for our planned MRI examination. At the fourth day five from the ten earthworms were swollen significantly and one of them was dead. The body mass of the earthworms corresponds to this observation.

In the group A, the change of the body mass as function of the time and the survival data were significantly better than in the control group B (Student's t-test, $P = 0.04$) (Fig. 1A and B). To keep the earthworms until the third day in Ringer solution with polystyrene plates in their boxes seemed to be optimal preparation for further experiments.

In summary, a 3 days long preparation time with the application of polystyrene plates was found optimal. Thus both the experiments to immobilize earthworms and to examine morphology of the organs with MRI were carried out in earthworms pre-treated in the way as described before.

Application of Chemical Compounds for Immobilization

The dose of pharmaceutical agents was based on the human toxic dose, using the extrapolation method of Reagan-Shaw et al. (2007).

Chemical agents, doses, method of application. and the outcome of the experiments are summarized in Tables 2 and 3.

Pharmaceutical agents could be delivered by injection into the coelomic cavity (Table 2). This method ensures the contact with the target organs (e.g., muscles, etc.). On the other hand in nearly all cases the earthworms were damaged after these administration procedures. According to our observations, 1 day after the injection the location of the puncture was remarkably swollen.

To apply on the earthworms the potential immobilizing pharmaceuticals in the bath made from Ringer solution is easier to carry out and the agents exposed to the earthworm body surface are homogeneous. Therefore, this application is more preferable if the applied immobilizing agent is suitable (Table 3).

Results: Inhaled Anesthetics. During inhalation of isoflurane and halothane anesthetics the earthworms released coelomic fluid and then died.

Results: Non-Depolarizing Neuromuscular Blockers. Administration of NDNBs gave various results. Injection of rocuronium caused a flaccid paralysis on earthworms for 2 hr, however, cisatracurium was not effective. Flaccid paralysis caused the total relaxation of the muscles. In addition, earthworms have lost their symmetrical round cross-section. Their body resistance was decreased compared to non-treated earthworms and did not react to touch. Injections of the solutions damaged the earthworm's bodies. Both agents were non-effective if they were applied according to our method.

Results: Parasympatho-Lythics (Physostigmine). Physostigmine caused flaccid paralysis in the segments posterior to the clitellum. The muscles were completely relaxed, but the segments functioned normally at the anterior region of earthworms.

Results: Parasympatho-Mimetics (Neostigmine, Atropine). Neostigmine and atropine, applied as an injection did not exert any effect corresponding to earthworm's locomotion.

Results: Sodium Channel Blockers (Benzocaine, Lidocaine). After applying benzocaine, a sodium channel blocker, we observed the extrusion of coelomic fluid and strong muscle contractions of the damaged earthworms. Lidocaine (0.25% 10 mL bath) caused convulse in the earthworms muscles. At lower doses we observe that lidocaine caused excitatory behavior and the earthworms became more active. The unexpected excitatory effect occurs at 15 min after treatment.

Results: GABA-Agonists (Glycine, Guaiphenesine, Sodium Barbithal, Meprobamate, Diazepam). GABA agonists such as glycine, guaiphenesine, sodium-barbithalum, meprobamate, and diazepamum were not effective.

Results: Opiates (Fentanyl). Fentanyl (0.005 mg injection, 0.5 mg/10 mL bath) also caused excitation, 1 min after treatment, independent of the application method. This effect lasted from 10 to 30 min.

Results: Alcohols (Ethanol and Propan-2-ol). After 30–60 min spent in isopropanol immersion, animals' muscles were completely relaxed. Thus they were immobilized for the duration of the experiments. The use of the airtight box was convenient for better handling of earthworms and avoiding gas exchange, it also kept the airspace in a steady state concentration the alcoholic vapor.

Ethanol and isopropyl alcohol treatment caused 5 min long immobilization in the aforementioned doses after the earthworm came into contact with fresh air.

However alcohols seemed to be useful, promising and effective method to immobilize earthworms for more than 3 hr if the body surface contact with the alcohol solution was maintained. On the other hand, fluids may disturb MR imaging modalities and greatly impair the result. This was avoided by the airtight box and bed, because of the bed kept the earthworms body over the alcoholic immobilization fluid's level, but the vapor of alcohol was in contact with the earthworms. The special bed avoided shifting of the anesthetized animals inside the box and enabled movement of the experimental specimens properly to the MRI modality as well. Indeed during the scan earthworms were not moving. Repeat exposure of the alcohol anesthesia induced a slight tolerance which was overcome by increasing the dose of alcohol.

Results: Ions. Mg^{2+}, Li^{+}, Br^{-}, 400 mg/10 mL were ineffective independent from all of the two types of application methods. Similarly the tested Ca^{2+} channel blockers were not applicable in our experiment set-up.

Results: Anthelmintics. Anthelmintics caused spasmic immobilization. Interestingly in some cases placid paralysis developed, but some motion of the head region were still observed.

Results: Combination of Anesthetics. Combination of ketamine and xylazine, in (0.12 mg + 0.1 mg/10 mL) doses was not effective (Green et al., '81; Greene and Thurmon, '88). The doses were increased until the body surface of animals were coated with the agents in such high concentration that it damaged the body surface. An excitatory effect was experienced, exactly 15 min after the treatment.

MRI Observations of Immobilized Earthworm Specimens

Using MRI certain organs of earthworms could be distinguished (Fig. 2). Septal walls, the muscles, and the coelomic cavity could be visualized.

We observed the brain at the third segment, while between the third and the eighth pharynx and between the ninth and the thirteenth segments the seminal vesicle was visible. The

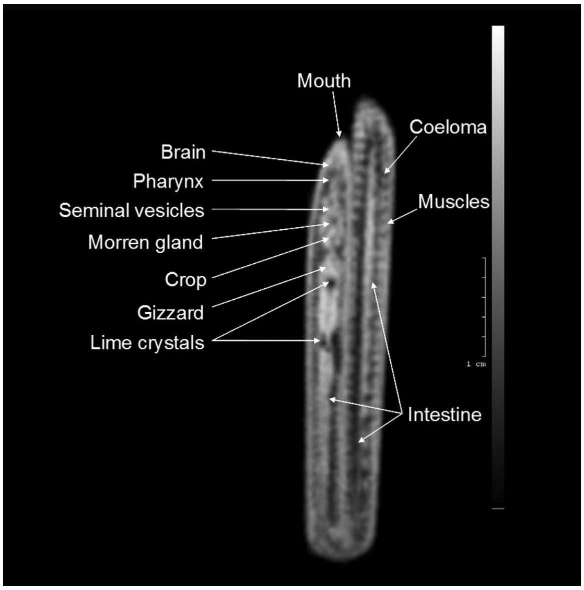

Figure 2. Organs of earthworm (*Eiseina hortensis* M.) are visualized by nanoScan PET/MRI (Mediso Ltd, Hungary). T1 weighted spoiled gradient echo sequence, 3 dimensional acquisition scheme.

circulatory system was relatively easily distinguishable between the ninth and the thirteenth segments. We detected the calciferous gland (Morren gland) between the tenth and eleventh segment. Lime crystals, produced by the Morren gland caused a strong negative contrast in MRI and could be detected in the intestines. By the sixth to the fourteenth segment the esophagus, from fifteenth to the seventeenth the gizzard and from eighteenth to the twentieth segment the stomach was detected.

DISCUSSION

Earthworms kept in Ringer solution for at least 3 days instead of soil were more suitable for MR imaging purposes than animals used directly without removing soil from the intestinal lumen. Using Ringer solution the gastrointestinal soil content was totally eliminated. This step is essential to avoid the soil absorbance of the pharmaceutical agents. Moreover, it reduced the signal level caused by magnetic susceptibility artifacts of MR imaging compared to those results where earthworms were kept in soil (data not shown).

In group A, the earthworms body mass remained near to the body mass measured on the first day until the third day unlike in earthworms body mass in group B caused by swelling due to Ringer solution (Fig. 1A and B). Thus we can state that polystyrene plates in earthworm's boxes are capable to protect earthworms from swelling (and consequently death) because indeed they can climb on polystyrene plates ad libitum and thus prevent being totally immersed in fluid. However some examined biomarkers (especially some sensitive gene's expression pattern) could have been distorted by the mentioned pretreatment to ensure that the bowels of earthworms are empty. That could limit the utility of our experimental method and requires to validate the usefulness of our test according to each specific aspect as desired. But numerous environmental pollutions exert long lasting and well-known in vivo effects on certain biomarkers and presumably independent affects from environmental moisture content and also absence of earth for at least the time of optimal pre-treatment (3 days). For example, the following exposures in annelids influence the listed spectacular biomarkers such as: immuno-stimulants decrease numbers and change composition of the coelomocytes (Homa et al., 2013); endocrine disruptors (Keay and Thornton, 2012); heavy metal (e.g., cadmium) pollution increases the expression of stress-related genes (heat shock proteins, metallothioneins, glutathione-*S*-transferase, superoxide dismutase, etc.); (Roh et al., 2006) or organic lead compound cause morphological change (inflexible metameric segmentation (Rao et al., 2003)); certain organophosphorus insecticide inhibit acetylcholinesterase enzyme activity (Rao and Kavitha, 2004) and per se genotoxic heavy metal (trivalent and hexavalent chromium) damage DNA (evaluated on the earthworm's coelomocytes using the comet assay (Bigorgne et al., 2010)).

MRI is performed with higher efficiency if the target organism avoids internal muscle contractions and movements (Fig. 2).

Generally, with the dose ranges used we observed effects on invertebrates similar to those reported by Reagan-Shaw et al. (2007) where the article reports the calculation of pharmaceutical doses from humans to other vertebrates.

The distinct effects of the applied NDMBs could correspond to their different chemical structure and mechanisms of action. NDMBs bind to acetyl-choline receptors or and antagonize the effects of acetyl-choline in a competitive manner at the postsynaptic nicotinic acetyl-choline receptors. However, cis-atracurium is a benzyl isoquinoline compound and lacks any vagolytic effect (in vertebrates). On the other hand, rocuronium is a monoquaternary amine and could be vagolytic in vertebrates (Appiah-Ankam and Hunter, 2004). Thus, we suppose that rocuronium could block muscarinic receptors in invertebrate species contrary to cisatracurium. Thus rocuronium could block movement. Also other effects of rocuronium on other receptors cannot be excluded.

Lipophilic physostigmine was effective only in the posterior segments of the clitellum. The lipophilic nature of these compounds is essential. Contrary to that neostigmine did not exert any effect on earthworms. Presumably due to the neostigmine's hydrophillic character, the absorption of this agent was hindered by coelomic fluid. According to Barna et al. (2001) atropine strongly inhibits the action of acetylcholine but is ineffective against certain neurotransmitters, such as serotonin, dopamine, and octopamine in earthworms. These neurotransmitters are involved in earthworm locomotion (Mill, '78).

Podolak-Machowska et al. (2013) tested local anesthetics in 0.0–2.0% concentrations to achieve anesthesia in *Eisenia hortensis* M. species. Lidocaine in 0.25% (2.5 mg/10 mL) concentration anesthetized earthworms ($n = 6$) for 2.5 and 24 hr later the earthworms were in good condition (Podolak-Machowska et al., 2013). This experimental setup seemed promising for our cause. However, in our hands we observed that the muscles of the earthworms were convulsing and the effects were too short for MR procedures. To perform optimal MRI we required completely relaxed muscles for the duration of the scan. Therefore we tried out lidocaine in lower doses on earthworms, but we experienced an unexpected excitatory effect. Lidocaine in low doses (0.01, 0.1, and 1 mM) causes general neuronal excitation in both presynaptic and postsynaptic neurons in some invertebrates (Shin et al., 2005). Presumably that underpins our observation about the increased movement of the lidocaine treated experimental group.

Despite that benzocaine (in 400 mg/mL) was useful to immobilize leeches for 3 hr (Lewbart, 2011), but for immobilization of earthworm it was not successful.

Neurotransmitters and xenobiotics, such as glycine, guaiphenesine, $GABA_A$ agonists, and opiates were not effective because sodium, potassium, and chloride ions are not exclusively responsible for resting membrane potential in earthworm longitudinal muscle (Mill, '78).

Barbiturates act by prolonging and potentiating the action of on $GABA_A$ receptors and at higher concentrations directly activate the receptors. The $GABA_A$-receptor β3 sub-unit seems to be essential in sedative and immobilizing effects of small rodents (Löscher and Rogawski, 2012). According to Rho et al. ('97) meprobamate enhanced a GABA-evoked concentration-dependent response in cultured rat hippocampal neurons using whole-cell voltage-clamps recordings. In addition, high concentrations (>1 mM) of this compound exhibited a separate channel-blocking effect. Meprobamate in the absence of GABA directly activated Cl^- currents that could be attenuated by $GABA_A$ receptor antagonists such as bicuculline and picrotoxin (Rho et al., '97). However, the chloride ion channel opening does not take part in forming of resting membrane potential in earthworm longitudinal muscle in such a manner that blocking it could lead to paralysation (Mill, '78).

Fentanyl caused excitation (Petrics and Larsson, '86) because opiates are involved in sensory neurons as transmitters, rather than in motor functions in earthworms.

Mg^{2+}, Li^+, Br^- (400 mmol/mL) were supposed to substitute the physiological analogues (such as Ca^{2+}, Na^+, and Cl^-, respectively) and influence their effects involved in signal transduction. The concentrations of Mg^{2+} was 100-fold higher in this experiment than the physiological concentrations (2.0–4.0 mmol) (Ochiai and Weber, 2002.). Extracellular magnesium ions inhibit the *Na-Ca antiport* in a competitive manner with calcium ions (Bara et al., '93). Inhibition of the Na-Ca antiport consequently inhibits the Na-H antiport (Bara et al., '93). Interestingly magnesium ions were not effective, in 50 μL injection, despite that Ca^{2+} is known as an important second messenger of various cell types also in invertebrates (Mill, '78; Opper et al., 2010).

For the same cause it could be supposed that the tested Ca^{2+} channel blockers, such as lamotrigin, felodipine, diltiazem, verapamil, and drotaverinum were neither useful to cause immobilization. This can be caused because the inward currents during the action potential are less than $0.3\ \mathrm{mAcm^{-2}}$ in the neuromuscular system of earthworms (Mill, '78). It refers to a less well-developed spike generating system. In comparison, in the frog skeletal muscle that potential is $2\ \mathrm{mAcm^{-2}}$. This threshold and the rates of action potentials are very sensitive to condition changes in the membrane potential (Mill, '78).

Diluted ethanol has anesthetic effects (Petrics and Larsson, '86), and using alcohols to immobilize earthworms have such benefits as a simple, reliable, non-invasive, and reversible approach. Further merit is that the animals do not extrude coelomic fluids, which is abundant in immune cells so called coelomocytes (Cooper et al., 2002). Therefore, immune-toxicological assessment of metal pollution on phagocytic activity (Brulle et al., 2006, 2007) could remain intact.

The effect is caused by direct influence of alcohol on the cell membrane. It is exerted by secondary intracellular transmitters, such as activation of the polyphospho-inositide-specific phospholipase C that triggers intracellular signalling responses. Through this pathway, more signal transmissions will be activated, including the formation of inositol-1,4,5-trisphosphate, the release of Ca^{2+} from intracellular storage sites (Opper et al., 2010) with the consequent activation of cytosolic Ca^{2+}-dependent enzymes and the formation of diacylglycerol leading to the stimulation of protein kinase C (Hoek and Rubin, '90). Another benefit is in using alcohols and leaving animals for 2–3 hr in the anesthetic fluid, the hearts of the animals could be stopped. Skin respiration still functions and this state is also reversible. With the mentioned "overdosing" the tested agents pharmacokinetic and dynamic (e.g., affinity to tissues and receptors) features could be tested "switching off" the circulation. Alcohols are appropriate anesthetic agents because in invertebrate among alcohol dehydrogenase (ADH) family only ADH3 isoenzyme exists (Albalat, 2009) and ADH3 oxidize low chained alcohols poorly (e.g., ethanol) or not at all (e.g., isopropanol) (Wagner et al., '84). The optimal immobilizing effect of isopropanol, compared to ethanol is because ethanol is metabolized by ADH3 enzyme into acetaldehyde that increases anion gap, unlike isopropanol. The increased anion gap causes acidosis and thereby can affect several physiological functions. Thus using alcohols as anesthetics the opportunity to repeat experiments with the same animal is possible. In contrast to ivermectin a further advantage is the distinct effects in various species (Wolstenholme and

Rogers, 2005). This anesthesia method of applying alcohols could be extended to every annelid species.

The contradictory effects of anthelmintics could be explained as ivermectin exerts through binding to glutamate-gated chloride (GluCl) channels, *inter alia* (Wolstenholme and Rogers, 2005). GluCls are expressed on neurons and pharyngeal muscle cells of nematode worms. Ivermectin activated channels act very slowly but irreversibly leading to a very long-lasting hyperpolarization or depolarization of the neuron/muscle cell. Therefore it can block further functions. Molecular and genetic studies have shown that multiple GluCl isoforms are expressed in both free-living and parasitic nematodes, but the exact function of the GluCl may vary from species to species (Pemberton et al., 2001; Wolstenholme and Rogers, 2005). In *Caenorhabditis elegans* pharynx model an intracellular recording technique elucidated that ivermectin caused a rapidly desensitizing glutamate response along with reversible, chloride-dependent depolarization ($EC_{50} = 166\,\mu M$). This later was weakly antagonized by picrotoxin. Thus, GluCl channels are the site of action of the ivermectin and GluCl-alpha2 subunit is essential to their function (Wright, '86). Indeed, our experimental setup with ivermectin caused mostly clonic spasmic immobilization. However, interestingly in some cases placid paralysis developed. Thus the mentioned anthelmintics were declared not to be useful for our purpose. The application of ivermectin to GluCl channels exerted an irreversible hyperpolarization on certain inhibitory motor neurons and their consequent inability to produce action potentials. This would prevent inhibitory transmission at the neuromuscular junction and hence the abolition of the waves of muscular relaxation required for movement (Wolstenholme and Rogers, 2005).

The multiple and contradictory effects of ketamine could be explained by the study of (Quibell et al., 2011). With other calcium and sodium channels, dopamine receptors, cholinergic transmission, and noradrenergic and serotoninergic re-uptake together with opioid-like and anti-inflammatory effects could be caused also by ketamine.

Experiments with ketamine, xylazine, and lidocaine tried to exploit the fact that with both of applications methods such as coating the body surface or immersion in aqueous solutions, the skin respiration of the animals ensured the uptake of the chosen materials in the case of hydrophilic agents. Furthermore, according to pharmacokinetics because the time of absorption was the same for these agents, an active enzymatic transporter mechanism is supposed by our group. Low sized lipophylic molecules usually cross biological membranes this is underpinned by the quick excitatory effect experienced by the fentanyl treatment.

CONCLUSION

The optimal preparation is to keep the earthworms until the third day in Ringer solution (Table 1) using polystyrene plates in their boxes for both of pharmaceutical and for in vivo imaging experiments to avoid earthworm's swelling caused by Ringer solution otherwise.

In general, certain hydrophilic pharmaceutical agents could be taken up by skin respiration. However, in most cases the influence of agents is exerted through the movement pattern of animals rather than according to the supposed immobilizing effects.

Diluted ethanol caused the best results to anesthetize earthworms (Petrics and Larsson, '86). According to the literature isopropanol exerts less influence on physiological functions than ethanol (Wagner et al., '84; Albalat, 2009). Thus it is more useful practically for immobilization if we consider the in vivo imaging applications.

Benefits of alcohol immobilization of earthworms are simple, reliable, non-invasive, and reversible. Thereby the opportunity to repeat experiments with the same animal is possible. Thus, with this method biological processes could be traced easier and with less experimental specimens.

According to the results of MRI approach, the reproductive organ could be detected. It is therefore possible to demonstrate reproductive capacity alterations in vivo in a longitudinal way where the animal is its own control and starting in an early stage contrary to generally used autopsy.

We, therefore, deduct that according to available literature data in context to some important biomarkers, for example, anatomical and morphological alterations (Rao and Kavitha, 2004) or reproduction and development factors (Keay and Thornton, 2012) in vivo imaging could have a complementary role for studying the effects of harmful environmental conditions on earthworms. Other distortions could be mapped in the future with further experiments specific for certain relevant ex vivo and histological biomarkers used in earthworm models to elucidate how our in vivo imaging based experimental method could complement the actually available tests.

ACKNOWLEDGMENTS

We thank the helpful discussions to Lóránd Barthó (Department of Pharmacology, Faculty of Medicine, University of Pécs) and László Molnár (Department of Comparative Anatomy and Developmental Biology, Faculty of Sciences, University of Pécs) and Miklós Kellermayer (Department of Biophysics and Radiation Biology, Semmelweis University) The support of István Bagaméry, Sándor Hóbor and Gábor Németh from Mediso Ltd. (Budapest, Hungary) is kindly acknowledged too. We gratefully acknowledge the financial support of the Medical Faculty Research Foundation, University of Pécs (PTE ÁOK-KA 2013/09), the support of EC-FP7 Transnational Access grant QNANO and TÁMOP-4.2.1./B-09/1/KMR-2010-0001. This paper was supported by the János Bolyai Research Foundation of the Hungarian Academy of Sciences.

LITERATURE CITED

Albalat R. 2009. The retinoic acid machinery in invertebrates: ancestral elements and vertebrate innovations. Mol Cell Endocrinol 1-2:23–35.

Appiah-Ankam J, Hunter JM. 2004. Pharmacology of neuromuscular blocking drugs. Contin Educ Anaesth Crit Care Pain 4:2–7.

Bara M, Guiet-Bara A, Durlach J. 1993. Regulation of sodium and potassium pathways by magnesium in cell membranes. Magnes Res 2:167–177.

Barna J, Csoknya M, Lázár ZS, et al. 2001. Distribution and action of some putative neurotransmitters in the stomatogastric nervous system of the earthworm, *Eisenia fetida* (Oligochaeta, Annelida). J Neurocytol 30:313–325.

Bigorgne E, Cossu-Leguille C, Bonnard M, et al. 2010. Genotoxic effects of nickel, trivalent and hexavalent chromium on the *Eisenia fetida* earthworm. Chemosphere 80:1109–1112.

Brulle F, Mitta G, Cocquerelle C, et al. 2006. Cloning and real-time PCR testing of 14 potential biomarkers in *Eisenia fetida* following cadmium exposure. Environ Sci Technol 8:2844–2850.

Brulle F, Mitta G, Leroux R, et al. 2007. The strong induction of metallothionein gene following cadmium exposure transiently affects the expression of many genes in *Eisenia fetida*: a trade-off mechanism? Comp Biochem Phys C 4:334–341.

Cooper EL, Kauschke E, Cossarizza A. 2002. Digging for innate immunity since Darwin and Metchnikoff. BioEssays 4:319–333.

Cortet J, Vauflery G-D, Poinsot-Balaguer A, et al. 1999. The use of invertebrate soil fauna in monitoring pollutant effects. Eur J Soil Biol 35:115–134.

Dominguez J. 2004. Earthworm ecology. Boca Raton: CRC Press. p 401–424.

Drewes CD, Pax RA. 1974. Neuromuscular physiology of the longitudinal muscle of the earthworm, *Lumbricus terrestris*. I. Effects of different physiological salines. J Exp Biol 60:445–452.

Doran JW, Parkin TB 1994. Defining and assessing soil quality. In J. W. Doran, D. C. Coleman, D. F. Bezdicek B. A. Stewart, editors. Defining soil quality for a sustainable environment. Madison, Wisconsin, USA: SSSA, Inc.

European Commission. 2006. Communication from the Commission to the Council, the European Parliament, the European Economic and Social Committee and the Committee of the regions: thematic strategy for soil protection. COM 231. Last accessed 04/04/2007: http://ec.europa.eu/environment/soil/.

Gerencsér G, Murányi E, Szendi K, et al. 2010. Ecotoxicological studies on *Hungarian peloids* (medicinal muds). Appl Clay Sci 50:47–50.

Green CJ, Knight J, Precious S, et al. 1981. Ketamine alone and combined with diazepam or xylazine in laboratory animals: a 10 year experience. Lab Anim 15:163–170.

Greene SA, Thurmon JC. 1988. Xylazine—a review of its pharmacology and use in veterinary medicine. J Vet Pharmacol Ther 11:295–313.

Heckmann LH, Hovgaard MB, Sutherland DS, et al. 2011. Limit-test toxicity screening of selected inorganic nanoparticles to the earthworm *Eisenia fetida*. Ecotoxicology 20:226–233.

Hoek JB, Rubin E. 1990. Alcohol and membrane-associated signal transduction. Alcohol Alcohol 2-3:143–156.

Homa J, Zorska A, Wesolowski D, et al. 2013. Dermal exposure to immunostimulants induces changes in activity and proliferation of coelomocytes of *Eisenia andrei*. J Comp Physiol B 183:313–322.

Keay J, Thornton JW. 2012. Hormone-activated estrogen receptors in annelid invertebrates: implications for evolution and endocrine disruption. Endocrinology 150:1731–1738.

Kibblewhite MG, Ritz K, Swift MJ, 2008. Soil health in agricultural systems. Phil Trans R Soc B 363:685–701.

Łaszczyca P, Augustyniak M, Babczyńska A, et al. 2004. Profiles of enzymatic activity in earthworms from zinc, lead and cadmium polluted areas near Olkusz (Poland). Environ Int 7:901–910.

Lavelle P, Decaëns T, Aubert M, et al. 2006. Soil invertebrates and ecosystem services. European J Soil Biology 42:S3–S15.

Leveque T, Capowiez Y, Schreck E, et al. 2013. Assessing ecotoxicity and uptake of metals and metalloids in relation to two different earthworm species (*Eiseina hortensis* and *Lumbricus terrestris*). Environ Pollut 179:232–241.

Lewbart GA. 2011. Invertebrate medicine. Chichester: Wiley-Blackwell. p 159–168.

Löscher W, Rogawski MA. 2012. How theories evolved concerning the mechanism of action of barbiturates. Epilepsia (Suppl 8):12–25.

Mill PJ. 1978. Physiology of annelids. London: Academic Press.

Morvan X, Mouvet C, Baran N, et al. 2006. Pesticides in the groundwater of a spring draining a sandy aquifer: temporal variability of concentrations and fluxes. J Contam Hydrol 87:176–190.

Morvan X, Saby N, Arrouays D, et al. 2008. Soil monitoring in Europe: a review of existing systems and requirements for harmonisation. Sci Total Environ 391:1–12.

Ochiai T, Weber RE. 2002. Effects of magnesium and calcium on the oxygenation reaction of erythrocruorin from the marine polychaete Arenicola marina and the terrestrial oligochaete *Lumbricus terrestris*. Zool Sci 9:995–1000.

Opper B, Németh P, Engelmann P. 2010. Calcium is required for coelomocyte activation in earthworms. Mol Immunol 11–12:2047–2056.

Pemberton DJ, Franks CJ, Walker RJ, et al. 2001. Characterization of glutamate-gated chloride channels in the pharynx of wild-type and mutant *Caenorhabditis elegans* delineates the role of the subunit GluCl-alpha2 in the function of the native receptor. Mol Pharmacol 5:1037–1043.

Petrics GB, Larsson LI. 1986. Enkephalins may act as sensory transmitters in earthworms. Cell Tissue Res 1:33–37.

Podolak-Machowska A, Kostecka J, Librowski T, et al. 2013. The use of selected Anaesthetic drugs in search of a method for improving earthworms' welfare. J Ecol Eng 14:83–88.

Quibell, R, Prommer, EE, Mihalyo, M, et al. 2011. Ketamine J Pain Symptom Manage 41:640–649.

Rao JV, Kavitha P. 2004. Toxicity of azodrin on the morphology and acetylcholinesterase activity of the earthworm Eisenia foetida. Environ Res 96:323–327.

Rao JV, Kavitha P, Rao AP. 2003. Comparative toxicity of tetra ethyl lead and lead oxide to earthworms, *Eisenia fetida* (Savigny). Environ Res 92:271–276.

Reagan-Shaw S, Nihal M, Ahmad N. 2007. Dose translation from animal to human studies revisited. FASEB J 3:659–661.

Rho JM, Donevan SD, Rogawski MA. 1997. Barbiturate-like actions of the propanediol dicarbamates felbamate and meprobamate. J Pharmacol Exp Ther 3:1383–1391.

Ruiz N, Mathieu J, Célini L, et al. 2011. IBQS: a synthetic index of soil quality based on soil macro-invertebrate communities. Soil Biol Biochem 43:2032–2045.

Ricketts HJ, Morgan AJ, Spurgeon DJ. 2004. Measurement of annetocin gene expression: a new reproductive biomarker in earthworm ecotoxicology. Ecotoxicol Environ Saf 1:4–10.

Roh JY, Lee J, Choi J. 2006. Assessment of stress-related gene expression in the heavy metal-exposed nematode *Caenorhabditis elegans*: a potential biomarker for metal-induced toxicity monitoring and environmental risk assessment. Environ Toxicol Chem 25:2946–2956.

Salomon K. 1941. Studies on invertebrate hemoglobins (erythrocrourins). J Gen Physiol 3:367–375.

Shin O, Toshiharu K, Toshiro H, et al. 2005. Lidocaine excites both pre- and postsynaptic neurons of reconstructed respiratory pattern generator in *Lymnaea stagnalis*. Anesth Analg 100:175–182.

Sousa JP, Bolger T, da Gama MM, et al. 2006. Changes in Collembola richness and diversity along a gradient of land-use intensity: a pan European study. Pedobiologia 50:147–156.

Spurgeon DJ, Hopkin SP. 1996. Effects of metal-contaminated soils on the growth, sexual development, and early cocoon production of the earthworm *Eisenia fetida*, with particular reference to zinc. Ecotoxicol Environ Saf 1:86–95.

Spurgeon DJ, Hopkin SP. 1998. Comparisons of metal accumulation and excretion kinetics in earthworms (*Eisenia fetida*) exposed to contaminated field and laboratory soils. Appl Soil Ecol 11:227–243.

Spurgeon DJ, Hopkin SP. 1999. Tolerance to zinc in populations of the earthworms *Lumbricus rubellus* from uncontaminated and metal-contaminated ecosystems. Arch Environ Contam Toxicol 3:332–337.

Strand K, Knapp JE, Bhyravbhatla B, et al. 2004. Crystal structure of the hemoglobin dodecamer from *Lumbricus erythrocruorin*: allosteric core of giant annelid respiratory complexes. J Mol Biol 1:119–134.

Wagner FW, Parés X, Holmquist B, et al. 1984. Physical and enzymatic properties of a class III isozyme of human liver alcohol dehydrogenase: chi-ADH. Biochemistry 23:2193–2199.

Wolstenholme AJ, Rogers AT. 2005. Biological activity and mode of action of avermectins. Parasitology 131:S85–S95.

Wright DJ. 1986. Biological activity and mode of action of avermectins. In: M. G. Ford, G. G. Lunt, R. C. Reay, P. N. R. Usherwood, editors. Neuropharmacology and pesticide action. Chichester: Ellis Horwood.

Xiaohui M, Yuhui Q, Zhenjun S, et al. 2012. Molecular toxicity of earthworms induced by cadmium contaminated soil and biomarkers screening. J Environ Sci 24:1504–1510.